

POWER MANAGEMENT AND DAMAGE ASSESSMENT TECHNIQUES
FOR SELF-POWERED SENSING BASED ON PIEZOELECTRIC
TRANSDUCTION

By

Mohamed Rhimi

A DISSERTATION

Submitted to
Michigan State University
in partial fulfilment of the requirements
for the degree of

Civil Engineering- Doctor of Philosophy

2013

ABSTRACT

POWER MANAGEMENT AND DAMAGE ASSESSMENT TECHNIQUES FOR SELF-POWERED SENSING BASED ON PIEZOELECTRIC TRANSDUCTION

By

Mohamed Rhimi

A major obstacle toward efficient health monitoring systems is the ability to accurately predict the remaining life of the monitored components. Several commonly used remaining life prediction models rely on empirical data which limits their applicability. Furthermore, the large scatter in material data, i.e., fatigue, combined with limited instrumentation capabilities has hindered the development and validation of improved prediction models. Thus, there is a need for adequate long-term continuous monitoring techniques capable of rendering a more precise and reliable stream of data. This would enhance the modeling proficiencies and would ultimately help reduce maintenance cost, improve the longevity, and enhance the safety of civil infrastructures.

Wireless sensors and sensor networks are emerging as substitutes for traditional tethered monitoring systems. A major consideration in using a dense sensor array for long term monitoring is the power availability and management. Piezoelectric energy powering has the advantage to act both as the sensor and as the powering means, thereby reducing the sensors' power requirement.

Improving the efficiency of piezoelectric power harvesting from civil structures ambient vibrations, while obeying environmental constrains (temperature variation) is the first objective of this thesis. The application of a variable preloading condition is used as a solution to modify the cantilever piezoelectric harvester's properties. A generalized system model is derived. Measured acceleration recordings from a concrete bridge decks under ambient loading and recordings from extreme events are used to show the gain in harvested energy when the harvester is in a preloaded

configuration. The effects of temperature variations on the piezoelectric (PZT) harvested energy from civil structures are also studied. A proposed mechanical tuning, based on the application of an axial load using Shape Memory Alloy to compensate the temperature effect, is presented.

The work required for the deployment of a long-term piezoelectric based monitoring system, with all necessary attributes, is also described. The calibration and installation of the sensor is addressed. Damage prediction abilities of the long term self-powered continuous monitoring system are evaluated considering full field data generation and interpolation issues. Sensor specific data interpretation techniques are developed and evaluated under laboratory conditions. The developed methods are based on tracking the variation with respect to time of the damage index, which strongly correlates to damage evolution if the sensor is in the influence zone of the monitored damage mechanism.

**Copyright by
MOHAMED RHIMI
2013**

TO MY FAMILY

ACKNOWLEDGEMENTS

I would like to express my gratitude to Dr. Nizar Lajnef for his guidance throughout my study at Michigan State University and I would like to extend my appreciation to Dr. Karim Chatti for his valuable advice and support. I also would like to thank also Dr. Tom Pence and Dr. David Grummon for reading my thesis and for their valuable comments.

I would like to acknowledge Dr. Nicholas Brake for his assistance with damage prediction models literature, and his concrete beam testing results.

Finally I would also like to thank all the graduate and undergraduate students at the Civil and Environmental Engineering Department (CEE) at Michigan State University.

Research in this dissertation has been supported in part by the FHWA grant DTFH61-08-C-00015.

TABLE OF CONTENTS

| | |
|---|-----------|
| LIST OF TABLES | ix |
| LIST OF FIGURES | x |
| CHAPTER 1: INTRODUCTION..... | 1 |
| Motivation..... | 1 |
| Piezoelectric Energy Harvesting from Civil Structures for Self Powered Sensing | 4 |
| Self Powered Long Term Monitoring System and Damage Prediction..... | 9 |
| Objective and Overview | 11 |
| CHAPTER 2: TUNABLE PIEZOELECTRIC ENERGY HARVESTING FROM CIVIL STRUCTURE..... | 13 |
| Introduction..... | 13 |
| General Model of Axially Preloaded Bimorph Piezoelectric Energy Harvester..... | 14 |
| System Configuration | 14 |
| Effect of Preloading on the Harvester Governing Equations | 16 |
| Experimental Setup and Model Verification..... | 20 |
| Experimental Setup | 20 |
| Model Verification and Experimental Results | 22 |
| Tunable Energy Harvesting from Ambient Vibrations in Civil Structures..... | 26 |
| Maximum Harvestable Power Using Preloaded Harvester | 26 |
| Tunable Energy Harvesting from Civil Structures | 28 |
| Conclusion | 34 |
| CHAPTER 3: PASSIVE COMPENSATION OF TEMPERATURE EFFECT ON PIEZOELECTRIC ENERGY HARVESTING FROM VIBRATION..... | 36 |
| Introduction..... | 36 |
| Temperature effects on the response of a bimorph piezoelectric energy harvester | 37 |
| Effect of Temperature on the Material Properties | 37 |
| Effect of Temperature on Piezoelectric Energy Harvesting from Vibration | 40 |
| Temperature effects correction using axial preloading..... | 43 |
| Experimental Setup | 43 |
| Preliminary Result: Temperature Compensation Using Preload | 45 |
| Passive self-tuned harvester using shape memory alloy effect | 47 |
| Passive Self-Tuned Harvester Design..... | 47 |
| Self-Tuned Vibration Energy Harvester | 50 |
| Numerical Analysis | 52 |
| Experimental Results and Validation | 56 |
| Conclusion | 57 |
| CHAPTER 4: PIEZOELECTRIC BASED SELF POWERED SENSOR FOR STRAIN MONITORING..... | 59 |

| | |
|--|-----------|
| Introduction..... | 59 |
| Piezoelectric floating gate Self Powered Sensor..... | 59 |
| Sensor description..... | 59 |
| Sensor Output under Service Load..... | 64 |
| Sensor Calibration and Initial Testing..... | 65 |
| Sensor Calibration..... | 65 |
| Experimental Setup and Initial Testing..... | 66 |
| Initial Fatigue Testing..... | 69 |
| Sensor Network..... | 70 |
| Probability Density Function of the Loading Distribution Parameters..... | 71 |
| Results and discussion..... | 75 |
| Conclusion..... | 77 |
| | |
| Chapter 5: DAMAGE PREDICTION USING PIEZOELECTRIC SELF POWERED SENSOR..... | 78 |
| Introduction..... | 78 |
| Damage Index Derivation..... | 78 |
| Experimental Setup and Damage Index Distribution..... | 80 |
| Experimental setup..... | 80 |
| Damage index distribution..... | 82 |
| Remaining Life Prediction..... | 84 |
| Linear Damage Accumulation..... | 84 |
| Survivability analysis..... | 86 |
| Probability density function of the damage index at failure..... | 86 |
| Survivability function..... | 87 |
| Results..... | 88 |
| Conclusion..... | 91 |
| | |
| CHAPTER 6: CONCLUSION AND RECOMMENDATIONS..... | 92 |
| | |
| BIBLIOGRAPHY..... | 94 |

LIST OF TABLES

| | |
|---|-----------|
| Table 1. Piezoelectric properties used in simulations..... | 15 |
| Table 2. Optimized maximum collected energy for axially loaded and unloaded beam harvester configurations..... | 31 |
| Table 3.. Material properties of the SMA wires used in the simulations..... | 52 |
| Table 4. Predicted remaining life using calibrated coefficient and the sensor output. | 85 |
| Table 5. Estimated remaining life using the different fitting shape function..... | 89 |

LIST OF FIGURES

| | |
|--|-----------|
| Figure 1. Frequency Response of PZT Beam Loaded in the Strain and Vibration Modalities | 6 |
| Figure 2. Experimental results of the output voltage amplitude, versus the excitation frequency and the temperature under 1 g base acceleration. (Mtip=3.75g, load resistance=1MΩ, P=-2N) | 8 |
| Figure 3. Schematic depiction of a cantilever bimorph piezoelectric vibration scavenger of length (L), width (b), and height (h+2a), subjected to axial loading. | 16 |
| Figure 4. (a) Test setup, loaded piezoelectric bimorph beam with attached tip mass; (b) experimental apparatus mounted on a shaker for testing (For interpretation of the references to color in this and all other figures, the reader is referred to the electronic version of this dissertation). | 21 |
| Figure 5. Predicted and measured output voltage across a 10MΩ resistance (a) Frequency=40Hz, axial preload=-2N, tip mass=3.75g, (b) Frequency=37Hz, axial preload=-6N, tip mass=3.75g | 23 |
| Figure 6. Variation of the first mode damping ratio with respect to applied axial loading. | 24 |
| Figure 7. Output voltage transfer function of the transducer under different preload conditions. Mtip=3.75g, Load resistance=10MΩ. (solid: theoretical, dots: experimental). .. | 25 |
| Figure 8. Resonant frequency variation with respect to applied axial loading for different tip mass (resistance R=10MΩ) | 27 |
| Figure 9. Maximum generated power with respect to applied axial loading for different tip mass (resistance R=1MΩ). | 28 |
| Figure 10. (a) Frequency spectrum for the acceleration measurements from the deck of a concrete bridge under traffic loading, (b) Variation of the output energy as a function of the applied preload subject to the recorded bridge accelerations (resistance R=1MΩ) | 30 |
| Figure 11. (a) Acceleration time-history from the 1985 Valparaiso earthquake, (c) Output energy with respect to tip mass for a loaded and unloaded system subject to the 1985 Valparaiso earthquake acceleration signal | 33 |
| Figure 12. Average power output generated by a piezoelectric harvester (Table 1) subject to a set of example earthquake accelerations events for both the unloaded and with applied optimal axial loading configurations (Table 2) – 1: Llole, 2: Elcentro, 3: El Salvador, 4: Northridge, 5: Uttarkashi, 6: Rapel, 7: Arthur Pass, 8: Dharmasala, and 9: Xiang | 34 |
| Figure 13. Temperature dependence of the elastic modulus of PZT-5H | 38 |

Figure 14. Temperature dependence of (a) the dielectric constant of PZT-5H and PZT-5A (Hooker, 1998), (b) the piezoelectric coefficient d_{31} of PZT-5H and PZT-5A (Hooker, 1998).
..... 39

Figure 15. Test Setup: (a) loaded piezoelectric bimorph beam mounted on a shaker, with the SMA springs, (b) experimental apparatus enclosed in an environmental chamber..... 41

Figure 16. Numerical results and experimental measurements of the output voltage amplitude versus the excitation frequency at different temperatures, under a 1g base acceleration. ($M_{tip}=3.75g$, load resistance= $1M\Omega$) 42

Figure 17. Variation of the first vibration mode damping ratio with respect to temperature 43

Figure 18. Temperature compensation for a variation from the 20° C reference to (a) 0° C, (b) 40° C. ($M_{tip}=3.75g$, load resistance= $1M\Omega$)..... 46

Figure 19. Schematic depiction of a piezoelectric beam with attached SMA axial loading mechanism, (a) compression mechanism, (b) tension mechanism. 49

Figure 20. SMA induced load versus temperature 52

Figure 21. Voltage transfer function versus temperature, (a) without SMA axial load, (b) with an axial load compensator for a temperature increase..... 53

Figure 22. Variation of the resonant frequency with and without SMA induced load (arrows indicate the direction of temperature variations) 55

Figure 23. Output voltage transfer function of the transducer at 60 °C with and without SMA induced axial loading. $M_{tip}=3.75g$, Load resistance= $1M\Omega$ 56

Figure 24. (a) Full sensor embedded in an epoxy package, (b) CMOS floating gate sensor.61

Figure 25. Illustration of the level crossing cumulative time counting implemented by the sensor..... 63

Figure 26. Schematic of a piezoelectric strain scavenger of length L, width b, and height h 65

Figure 27. Voltage transfer function of a PZT piezo under 50 micro-strain loading across 50 mega-ohm load resistance 66

Figure 28. (a) Piezoelectric transducer embedded in epoxy then bounded to concrete, (b) Bending test setup to check the activation strain loss from a configuration to another. 67

Figure 29. Cumulative distribution of strain duration expressed in term of voltage. 68

| | |
|--|-----------|
| Figure 30. Strain distribution at different life stages: (a) at 25000 cycles, (b) at 40500 cycles. | 69 |
| Figure 31. Fitting of the sensor’s output at different life stages of the specimen: (a) at 25000 cycles, (c) at 40500 cycles. | 70 |
| Figure 32. Pavement cross-section with sensors installed at the bottom of the HMA layer | 72 |
| Figure 33. Schematics of the likelihood maximization algorithm | 74 |
| Figure 34. Theoretical and estimated density functions of the three parameters using the 10 sensors. (a) mean. (b) cumulative loading time | 76 |
| Figure 35. Least square estimation error of each of the parameters' distributions versus number of deployed sensors | 77 |
| Figure 36. Test setup: the sensor is installed in the bottom of the concrete specimen to measure the induced tensile strain. | 81 |
| Figure 37. Probability distribution of the damage coefficient versus the number of cycles of loading | 83 |
| Figure 38. (a) Variation over time of the mean of the damage index versus the exact damage index evaluated with the COD gage, (b) Variation of the variance of the damage index distribution. | 83 |
| Figure 39. Probability density function of the damage index at failure | 86 |
| Figure 40. Normalized estimated remaining life vs. normalized specimen’s lifetime using three different methods, (a) first specimen (b) second specimen | 89 |

CHAPTER 1: INTRODUCTION

MOTIVATION

One major obstacle facing health monitoring systems is the ability to accurately predict remaining life after structural state diagnosis. Today, many remaining life prediction models rely on empirical data which limits their applicability. Moreover, the large scatter in material data, i.e., fatigue, combined with archaic instrumentation has hindered the development and validation of improved prediction models. There is a need for long term continuous monitoring techniques capable of rendering a more precise and reliable stream of data that would enhance the modeling proficiencies and would ultimately help reduce maintenance cost, improve the longevity, and enhance the safety of civil infrastructures.

In recent years, there has been an increasing interest in the adoption of emerging sensing technologies for instrumentation within a variety of structural systems. Wireless sensors and sensor networks are emerging as sensing paradigms that the structural engineering field has begun to consider as substitutes for traditional tethered monitoring systems. Lynch et al., 2006, Watters et al., 2003 and Cho et al., 2008 summarized the most newly developed and adopted wireless sensors; where the wireless sensors are not sensors, but rather are autonomous data acquisition nodes to which traditional structural sensors (e.g. strain gages, accelerometers, linear voltage displacement transducers, inclinometers, among others) can be attached. However the adopted technology does not appear to have kept pace with other technological improvement (Lajnef et al., 2011). The

existing monitoring approaches remain rather reactive than proactive in terms of detecting damage, since they merely record the distress that has already appeared. They either require significant personnel time or the use of costly equipment. Thus they can only be used cost-effectively on a periodic and/or localized basis. The current technology does not allow for continuous long-term monitoring and the deployment of existing systems on a network level remains infeasible due to cost, unease of installation, and data collection techniques.

A major consideration in using a dense sensor array for long term monitoring is the problem of providing power to the sensors. If the only way to provide power is by direct connections, then there is no need for wireless protocols. To date, batteries have been the primary means of powering wireless devices. Battery power can last anywhere from a few days to 10 years. For practical infrastructure monitoring, it is desirable that the sensors last the service lifetime of the structure; typically, a structure's lifespan is several decades, but it can be as long as 100 years. Even with the continued trend of decreasing the power consumption of electronics, it is likely that battery self-discharge would limit the useful lifetime of any sensor to 10 years. In the cases of remote structures and embedded sensors, it is impractical and costly to change batteries periodically through the lifetime of the structure. The problems associated with powering wireless sensors have led several research groups to investigate self-powering as a means of providing continuous power to remote sensors (Elvin et al., 2006).

A possible solution to the problem of localized power generation is technologies that enable harvesting ambient energy to power the instrumentation (Roundy et al., 2002; Rahimi et al., 2003; Sodano et al., 2004; Elvin et al., 2006; Lajnef et al., 2008), where a myriad of potential self-powering energy sources have been identified (e.g., solar power, thermal gradient, piezoelectric, vibration and acoustic).

It is estimated that the amount of harvestable energy from solar and thermal gradient is not enough to power a sensor. A piezoelectric powered sensor can, on the other hand, provide a reliable energy source that is a function of the input mechanical loading experienced by the monitored structure, making it a reliable embedded energy source.

As shown by Elvin et al. 2006, piezoelectric energy powering has the added advantage to act both as the sensor and as the powering means, thereby reducing the power requirement and cost of the sensor system. The piezoelectric transducer can generate large voltage signals (> 10 V), but exhibit limited current driving capability ($< 1\mu\text{A}$), limiting the level of extractable power. But, this ideally combines with the intrinsic properties of analog floating memories that can operate at very low current levels (pico-amperes).

A CMOS floating gate is a poly-silicon gate surrounded by an insulator, which in standard semiconductor fabrication process is silicon-dioxide. The charge on the gate can be modified using hot electron injection or through tunneling. Injection in a pMOS transistor occurs primarily due to hot-hole impact ionization caused by high electric fields at the edge of the drain-to-channel depletion region. As electrons are added to the floating gate its potential decreases, thus implementing a long term non-volatile memory.

Based on the described technology, the sensor was developed, tested and calibrated (Lajnef et al., 2007). Measured results from a fabricated prototype in a $0.5\ \mu\text{CMOS}$ process have demonstrated that the processor can sense and measure the piezoelectric output voltage subjected to strain loading. It measures the output voltage in a series of memory cells. Each cell records the cumulative duration when the piezoelectric output-voltage exceed a preset level. This direct use of the piezoelectric input signals allows the sensor to be self-powered and it can operate at very low power levels.

PIEZOELECTRIC ENERGY HARVESTING FROM CIVIL STRUCTURES FOR SELF POWERED SENSING

In order to use the existing concrete manufacturing methods to incorporate the sensor within the structure, we have constrained the maximum volume of the sensor to be 5 cm^3 , corresponding to the maximum size of a concrete aggregate that doesn't lead to a significant weakening of the structure (Issa et al., 2000). However, when limited to 5 cm^3 , the vibration based piezoelectric will typically have a resonant frequency in the range 100-300Hz, while most civil structures exhibit a fundamental vibration mode at frequencies less than 10 Hz. This mismatch significantly limits the levels of extractable power.

Figure 1(a) shows the voltage output of a bimorph PZT (1 cm x 4 cm) subjected to variable strain loading versus the loading frequency. The piezoelectric bimorph is mounted in patch configuration, and subjected to the strain induced in the structure. Starting from 50 micro-strain, which corresponds to the ultimate fatigue limit of concrete, the piezoelectric can provide enough energy to power the floating gate sensor, covering most of the needed frequency and strain range to sense. However when mounted in cantilever configuration used to harvest energy from vibration (Figure 1(b)), the minimum power needed is met either at very high vibration amplitudes, 2 g and more, or at higher frequencies. Thus improving the conversion capabilities of the piezoelectric-harvester subjected to dynamic excitation, while obeying all necessary constrains, is critical toward the successful implementation of a self-powered monitoring system.

Several external environmental effects, such as temperature variation, also alter the performance of vibration piezoelectric harvester, and limit its longevity and its efficiency. The

temperature variations in civil structures varies from -20° to 50° C significantly limiting the levels of extractable power. Several studies have been conducted to determine the effect of ambient temperature on piezoelectric properties and the levels of extractable energy. Birman et al. 2006 evaluated the effect of uniformly distributed temperature on the vibrations of a piezoelectric rod polarized in the axial direction. Omote et al., 1996 investigated the temperature dependence of elastic, dielectric, and piezoelectric properties of single crystalline films of vinylidene fluoride–trifluoroethylene copolymer. A change of more than 100% in the elastic modulus was shown in the range 20° to 50° C, affecting the stiffness of the harvester, and reducing dramatically the level of harvestable energy. Similar variations were observed for the dielectric constants, particularly the piezoelectric constant d_{31} . Mane et al., 2007 used a prestressed PZT-5A unimorph beam to characterize the dependence of the output voltage to temperature variations in the range of 20 to 100° C. Hooker, 1998 investigated the dependence of lead zirconate titanate (PZT)-4, PZT-5A, PZT-5H, and lead lanthanum zirconate titanate (PLZT)-9/65/35 properties with respect to temperature variations in the range -150 to 250° C. Figure 2 shows the experimental results of the voltage transfer function of a PZT bimorph mounted in a cantilever configuration subjected to base excitation at different temperature. The base acceleration was kept constant at 1g for varying input excitation frequency from 35 to 55 Hz (a selected range around the resonant response of the system) and a varying temperature from -20 to 40° C. A very pronounced effect is observed on both the resonant frequency and the amplitude.

A variety of options for improved piezoelectric harvesters have been previously examined. These include improvements through the optimization of the piezoelectric material, altering the electrode patterns and system configuration, the use of a matching network, and tuning the device's resonant frequency for maximum response and power transfer.

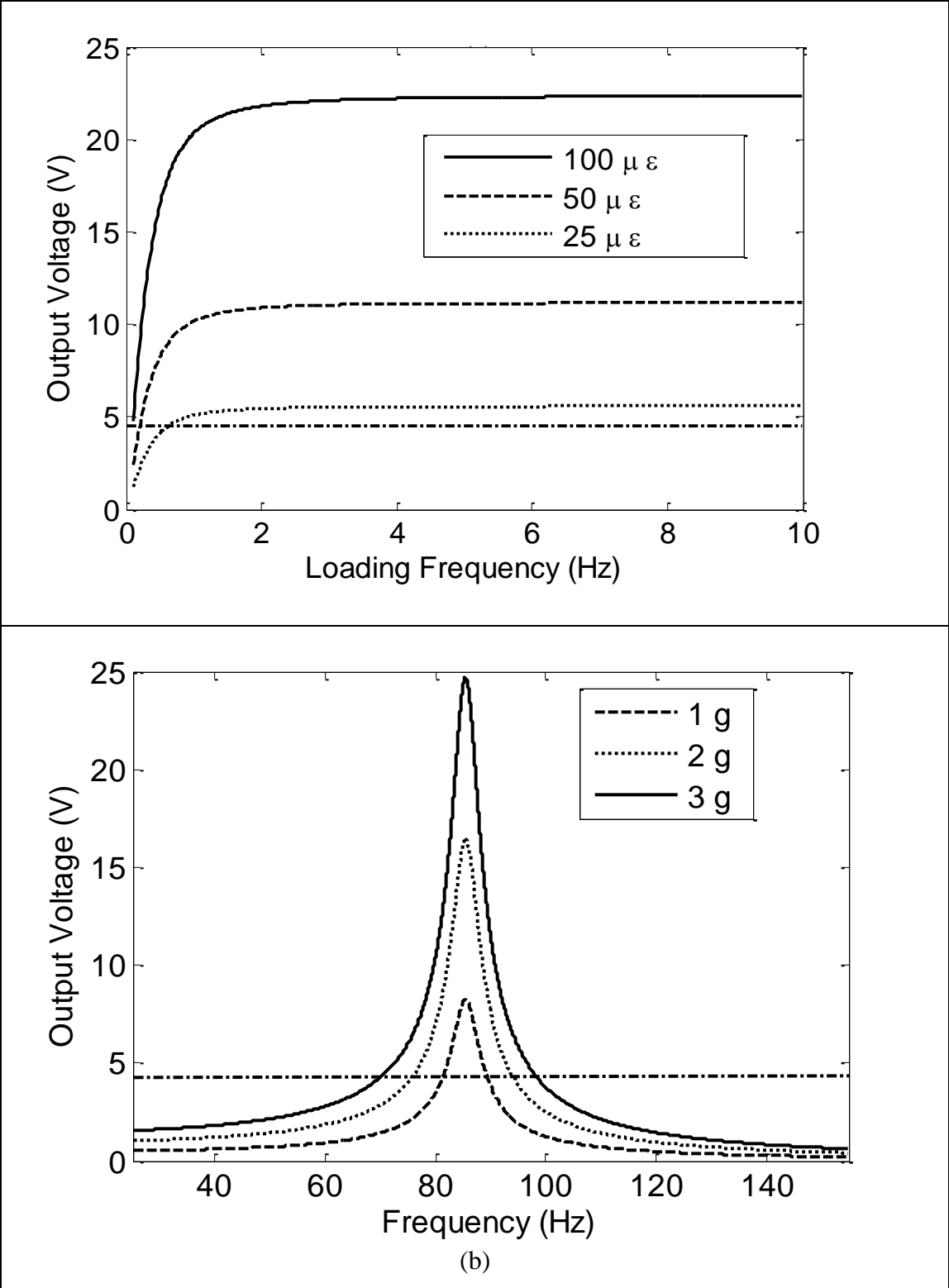


Figure 1. Frequency Response of PZT Beam Loaded in the Strain and Vibration Modalities

Results from all these studies showed that PZT ceramic remains one of the most practical options for energy harvesting from base excitation, primarily because of its low-cost and high-coupling characteristics.

Altering the stiffness of the vibrating device can maintain its natural frequency at the desired spectrum. Several different designs have been proposed to achieve this tuning capability. Leland et al., 2006 presented an analytical formulation of a tunable harvester using a simply supported piezoelectric beam with a proof mass at its mid-span. Only the first mode was addressed. An experimental apparatus was built, and measurements were compared with the theoretical predictions. Eichhorn et al. 2009 designed an experimental mechanism for pre-stress bidirectional frequency tuning on the basis of the theoretical formulation presented in Hu et al., 2007. An adjustable link was used by Morris et al., 2008 to build a tunable frequency mechanism. Frequency variations from 80 to 235 Hz were measured. Challa et al., 2008 and 2009 used magnetic forces to build a tuning mechanism. It was shown that resonance tuning of 20% is achievable. Piezoelectric actuation was also used by Peters et al., 2008 to build an electrically tunable resonator. An input voltage variation of 5 V was shown to achieve a shift of the resonant frequency by 15%. Although these designs were successful at adjusting the vibration response, they are impractical as energy-harvesting devices because they require high input power for control, making them obsolete as scavengers.

Eichhorn et al., 2011 proposed a design for a self-sufficient frequency-tunable harvester. The system's stiffness is altered to tune the resonance frequency using a piezoelectric actuator, controlled by a self-adjusting control unit that delivers the appropriate voltage for correction. The system converges to a stable operation mode within minutes, which is impractical for ambient

vibration events in civil structures. Around its optimal operational range, up to 90% of the harvested energy can be fed to the powered electrical load.

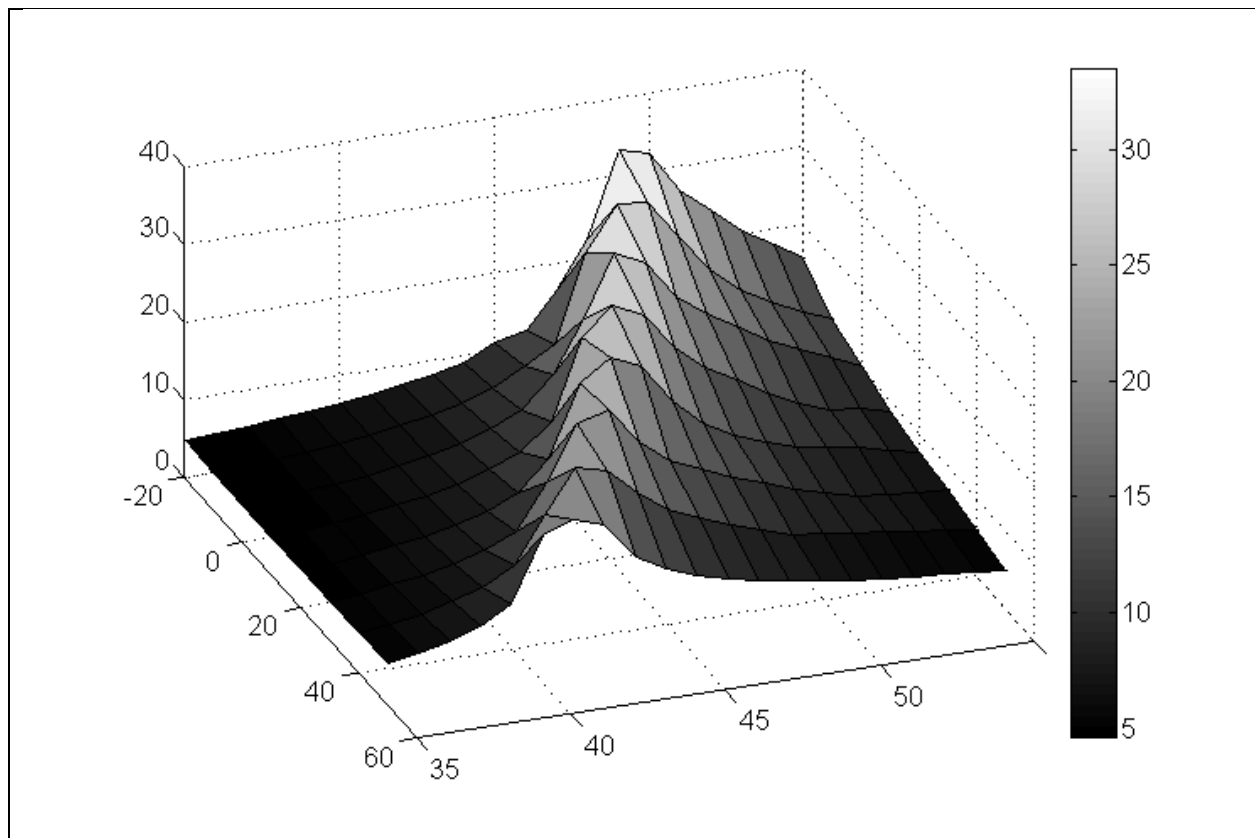


Figure 2. Experimental results of the output voltage amplitude, versus the excitation frequency and the temperature under 1 g base acceleration. ($M_{tip}=3.75g$, load resistance= $1M\Omega$, $P=-2N$)

Stanton et al., 2010 used nonlinear systems as an alternative way to enhance the vibrator response over a broader frequency range. A bi-stable inertial generator consisting of permanent magnets and a piezoelectric beam was investigated. An analytical model was developed, and it was shown experimentally that the system's frequency response can be enhanced. Erturk et al., 2011 introduced a non-resonant piezo-magneto-elastic energy harvester. They investigated experimentally and analytically the high-energy orbits in the bi-stable Duffing oscillator over a

wide range of frequencies. It was proved that the proposed device can generate power an order of magnitude higher than piezo-elastic devices under different excitation frequencies.

SELF POWERED LONG TERM MONITORING SYSTEM AND DAMAGE PREDICTION

The last 40 years have seen a rapid increase in the research related to damage prediction, which can be classified to either local or global. Global methods are mostly structural response vibration based. Doebling et al., 1996, Garden et al., 2006 and Fan et al., 2010 have provided a review of the most common vibration-based methods and algorithms to identify global damage of structures. They can be classified into three major categories: natural frequency-based methods, mode shape-based methods and curvature mode shape-based methods.

Natural frequency-based methods use the natural frequency's change as a way to identify and predict damage. The natural frequency change is attractive because it is usually less sensitive to experimental noise. However it has several other common limitations: low sensitivity to damage and difficulty of measurement.

However compared to natural frequencies, using mode shapes as a basic feature for damage detection is more advantageous: the mode shapes contain local information, which makes them more sensitive to local damages, and less sensitive to environmental effects, such as temperature. The disadvantages are also distinct; the measurement of the mode shapes requires more sensors; the measured mode shapes are more susceptible to noise contamination than natural frequencies. An alternative way of using mode shape to obtain spatial information about sources of vibration changes is by using the shape mode derivative, such as curvature. In fact, there is a direct relationship between curvature and bending strain for beams, plates, and shells.

Simultaneously, tremendous efforts have been spent on local damage investigation; different prediction models have been developed, either based on linear fatigue damage accumulation (LRD) accompanied with an experimentally generated log-log S-N curve (Basquin, 1910 and Coffin, 1954), or a reliability approach to predict fatigue damage accumulation (Park, 1990; Oh, 1991; Singh et al., 2001) by inserting an experimentally observed probability density function into the LDR to express the number of cycle to fail in terms of a probability.

Several researchers proposed modifications to the original LDR approach. The double linear damage rule (DLDR), introduced by Manson, 1966, separated the S-N curve into two regions to represent the differences in damage accumulation rates within the crack initiation and crack propagation stages. This method was then refined to include a damage curve function (Manson and Halford, 1981) that allowed damage to be expressed as a non-linear power function dependent on load-level. Oh, 1991, developed a non-linear damage rule for concrete that expresses the damage index (D) as a load-level dependent cubic polynomial, and was able to predict the LDR error for both L-H and H-L loading sequences. More recently, a one dimensional continuum damage mechanics model was used to predict the load sequence effect (Lemaitre, 1992; Xiao et al., 1998). These models associate damage directly to elastic modulus degradation and are founded on thermodynamic principles in which the damage induced strain energy release rate is the driving force for damage.

The piezoelectric self-powered sensor has showed significant promise toward a successful integration of a strain sensor. However the used data management and organization protocol results inevitably end in a considerable loss of information since it is not stored as function of real time, but rather compressed as a function of cumulative time at each strain level. As a consequence, the

interpretation and usefulness of the strain histogram as a mean to predict the remaining life using the conventionally developed methods is not possible.

OBJECTIVE AND OVERVIEW

This thesis is composite of two big chapters: (1) Improving piezoelectric power harvesting from vibration, in order to achieve the minimum power needed for a self-powered vibration monitoring system and (2) Successful deployment of the newly developed self-powered strain sensing system for damage monitoring and remaining life prediction in civil structures, particularly concrete.

The improvement of piezoelectric energy harvesting from civil structures using stiffness control will be the focus of the first chapter; the application of a variable preloading condition is used as a solution to modify the system's properties. A generalized model that takes into account all the vibration-mode shapes of the beam and the back-coupling effect is derived using the Hamiltonian principle. Measured acceleration from a concrete bridge deck under ambient loading and recordings from extreme events (earthquakes) are used to show the gain in harvested energy when the harvester is in preloaded configuration.

In the second chapter, the effects of temperature variations on the piezoelectric (PZT) harvested energy from civil structures are studied. A proposed mechanical tuning, based on the application of an axial load using Shape Memory Alloy to compensate the temperature effect, is presented. A fully passive temperature compensation mechanism is proposed, and numerical analysis showing the improvement of energy conversion from civil structures is presented.

In order to select the best model that would fit the sensor output, the sensor will be implemented, tested and its output will be defined. The work describing a fully deployed sensing system with all the needed attributes will be presented in chapter three. The calibration and

installation of the sensor is addressed. Defining the sensor output from real time loading distribution is shown. Finally the evaluation of a full field data from a limited number of randomly distributed sensor is studied.

In the fourth chapter, the damage prediction abilities of the long term self-powered continuous monitoring system are evaluated. The sensor is able to continuously monitor and cumulatively record strain events experienced by the structure over extended periods given its self-powered characteristic. A slightly modified linear damage accumulation approach is then proposed using the damage index founded on continuum mechanics definition. The derivation of the damage index using the sensor's output data is detailed with results from a set of laboratory tests, comparing the damage index prediction output from the sensor and values obtained using the complete time history data. Finally, a projection of the remaining life of the tested specimens using reliability analysis was computed and its accuracy was evaluated by completing the test until failure and counting the total real observed cycles, showing very promising results for full field deployment.

CHAPTER 2: TUNABLE PIEZOELECTRIC ENERGY HARVESTING FROM CIVIL STRUCTURE

INTRODUCTION

Vibration based PZT bimorph scavenger, mounted in a cantilever configuration and with an overall volume limited to less than 5cm^3 (Issa et al., 2000; Elvin et al., 2006), will typically have a resonant frequency in the range 100-300Hz, while most civil structures exhibit a fundamental vibration mode at frequencies less than 10 Hz.

When excited with a frequency equal to the first vibration mode of the harvester, the amount of harvested energy is maximum. However civil structures vibrate at lower frequency, making the level of output voltage amplitude a hundred times less important. This mismatch significantly limits the levels of extractable power. Therefore, improving the conversion capabilities of these systems, while obeying all necessary constraints, is critical toward a successful implementation for structural health monitoring.

A variety of options for improved PZT harvesters have been previously examined. These include the altering of the electrodes patterns and system configuration (Erturk et al., 2008 and 2009; Mateu and Moll, 2005; Goldschmidtboeing and Woias, 2008; Rupp et al., 2009), the use of matching network (Kim et al., 2007; Shu et al., 2007; Challa et al., 2011), and the tuning of the device's resonant frequency for maximum response and power transfer (Eichhorn et al., 2009 and 2011; Hu et al., 2007; Challa et al., 2008 and 2009).

The objective of the first chapter is to show that by using axial preloading as a way of tuning the frequency response of the piezoelectric harvester the minimum output power requirement to use the existing sensing technologies to monitor extreme events can be met. The effect of the preload on the conversion process is analyzed. A comprehensive analytical model based on the Hamiltonian principle is developed. The results show the effect of the preload on the dominant frequency of the resonator. Then the experimental verification of the design is presented. The apparatus' response is measured in both the time and frequency domains then compared to theoretical observations. Finally, case studies are presented. Vibration histories gathered from published data are used to estimate the harvestable power for different axial preload configurations in order to show the high improvement in piezoelectric energy harvesting from vibration in civil structures.

GENERAL MODEL OF AXIALLY PRELOADED BIMORPH PIEZOELECTRIC ENERGY HARVESTER

System Configuration

The configuration and the material properties of a bimorph piezoelectric vibration energy harvester mounted in cantilever configuration are shown in Figure 3 and Table 1. The piezoelectric cantilever bimorph beam is subjected to base excitation and to a permanent axial preload. The energy method is used to derive the constitutive equation.

The basic variational indicator equation is given by:

$$\int_{t_1}^{t_2} [\delta T - \delta U + \delta W] dt = 0 \quad (1)$$

where T is the kinetic energy and W is the work of external forces expressed as:

$$T = \frac{1}{2} \int_{V_s} \rho_s \dot{u}(x,t) \dot{u}(x,t) dV_s + \frac{1}{2} \int_{V_p} \rho_p \dot{u}(x,t) \dot{u}(x,t) dV_p + M_{tip} \dot{u}(L,t) \dot{u}(L,t) \quad (2)$$

$$W = \int_{V_s} \rho u(x,t) f(t) dV_s + \int_{V_p} \rho u(x,t) f(t) dV_p + M_{tip} u(L,t) \cdot f(t) \quad (3)$$

and

- u : deflection
- ρ : density
- f : base acceleration
- ' p ': subscript which represents the PZT material
- ' s ': subscript which represents the metallic substrate

Table 1. Piezoelectric properties used in simulations.

| Properties | Values |
|------------------------------------|-------------------------|
| Elastic modulus PZT C_s | 72 GPa |
| Elastic modulus substrate C^E | 11 GPa |
| Density piezoelectric ρ_p | 7900 g/m ³ |
| Density substrate ρ_s | 8900 g/m ³ |
| Piezoelectric constant d_{31} | 270e-12 m/V |
| Electrical permittivity ϵ | 3500 ϵ_0 (F/m) |
| Beam length, width (L, b) | (40, 10) mm |
| Thicknesses(a, h) | 0.1 mm, 0.2mm |

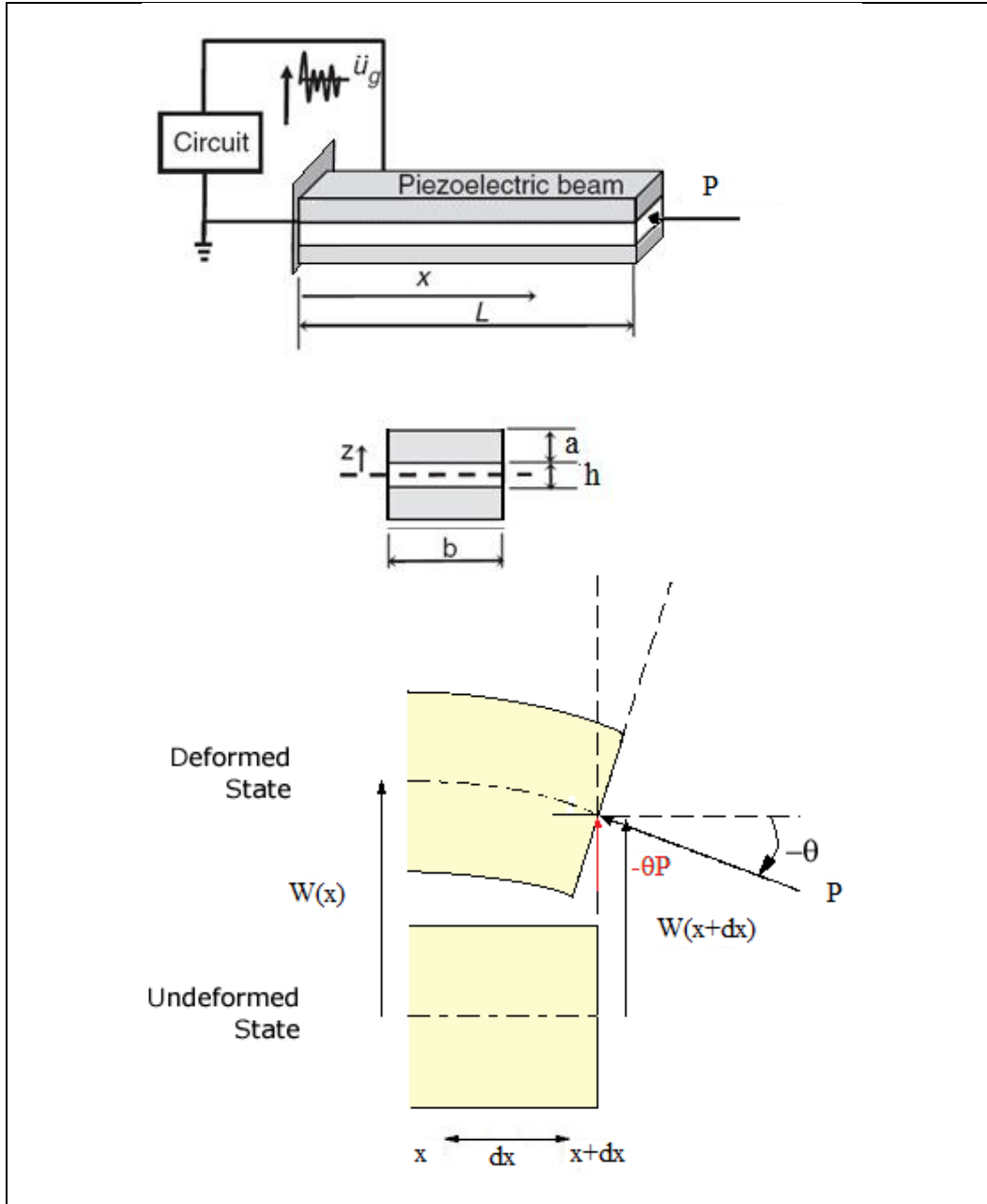


Figure 3. Schematic depiction of a cantilever bimorph piezoelectric vibration scavenger of length (L), width (b), and height ($h+2a$), subjected to axial loading.

Effect of Preloading on the Harvester Governing Equations

The added axial preload is incorporated in the constitutive equations of the cantilever beam as a change in the potential energy U of the system. Since the system is under a permanent axial

load P , this change is due to the additional internal non-dissipative energy. The total potential energy of the resonant system is then expressed as follow:

$$\begin{aligned}
 U = & \underbrace{\frac{1}{2} \int_{V_s} \underline{S}^T \underline{T} dV_s + \frac{1}{2} \int_{V_p} \underline{S}^T \underline{T} dV_p + \frac{1}{2} \int_{V_p} \underline{E}^T \underline{D} dV_p}_{I} \\
 & + \underbrace{\frac{1}{2} \int_L P \left(\frac{\partial u}{\partial x} \right)^2 dx}_{II}
 \end{aligned} \tag{4}$$

where \underline{S} , \underline{T} , \underline{E} , \underline{D} , and V are the strain, the stress, the electric field, the electric displacement, and the material's volume.

Incorporating the linear piezoelectricity equations into the potential energy function, yield the following general potential form:

$$U = \frac{1}{2} \left[\begin{aligned} & \int_{V_s} \underline{S}^T c_s \underline{S} dV_s + \int_{V_p} \underline{S}^T c^E \underline{S} dV_p - \int_{V_p} \underline{S}^T e^T \underline{E} dV_p \\ & - \int_{V_p} \underline{E}^T \varepsilon^S \underline{E} dV_p + \int_L P \left(\frac{\partial u}{\partial x} \right)^2 dx \end{aligned} \right] \tag{5}$$

where c , ε and e are the modulus of elasticity, the dielectric constant and the coupling factor, respectively. The superscripts, $()^S$ and $()^E$, indicate that the parameter is estimated either at constant strain or constant electric field.

Incorporating the variation of the external work, and the kinetic and potential energy into equation (1), the variational indicator becomes:

$$\int_{t_1}^{t_2} \left[\int_{V_s} \rho_s \delta \dot{u} \dot{u} dV_s + \int_{V_p} \rho_p \delta \dot{u} \dot{u} dV_p + M_{tip} \delta \dot{u}(L,t) \dot{u}(L,t) \right. \\ \left. - \int_{V_s} \delta \underline{S} c_s \underline{S} dV_s - \int_{V_p} \delta \underline{S} c^E \underline{S} dV_p + \int_{V_p} \delta \underline{S}^T e^T \underline{E} dV_p \right. \\ \left. + \int_{V_p} \delta \underline{E}^T e \underline{S} dV_p + \int_{V_p} \delta \underline{E}^T \varepsilon^s \underline{E} dV_p - \int_L P \delta u' u' dx \right. \\ \left. + \int_{V_s} \rho_s \delta u f(t) dV_s + \int_{V_p} \rho_p \delta u f(t) dV_p + \delta u(L,t) M_{tip} f(t) \right] dt = 0 \quad (6)$$

Assuming Euler-Bernoulli behavior for the considered cantilever beam subjected to the external force (induced by the base excitation) as shown in Figure 3, the longitudinal strains are deflection induced and are expressed as follows:

$$\underline{S} = -y \frac{\partial^2 u(x,t)}{\partial x^2} \quad (7)$$

The deflection and the electrical field are expressed in the modal and field coordinates as:

$$u(x,t) = \sum_{i=1}^N \phi_i(x) r_i(t) = \underline{\phi}(x) \underline{r}(t) \quad (8)$$

$$E(y,t) = \sum_{i=1}^M \psi_i(y) v_i(t) = \underline{\psi}(y) \underline{v}(t) \quad (9)$$

where ψ defines the field over the thickness of the PZT.

Substituting Equations 7, 8 and 9 into the variational indicator (Equation 6), leads to the two coupled equations expressed as follows:

$$\begin{cases} M_T \ddot{r}(t) + (K_T + \tilde{K})r(t) - \Theta v(t) = M^* f(t) \\ \Theta^T r(t) + C_p v(t) = q(t) \end{cases} \quad (10)$$

where the mass and the stiffness matrices of the system can be written as:

$$\begin{cases} M_T = \int_{V_s} \rho_s \underline{\phi}^T(x) \underline{\phi}(x) dV_s + \int_{V_p} \rho_p \underline{\phi}^T(x) \underline{\phi}(x) dV_p + M_{tip} \underline{\phi}^T(L) \underline{\phi}(L) \\ M^* = \int_{V_s} \rho_s \underline{\phi}(x) dV_s + \int_{V_p} \rho_p \underline{\phi}(x) dV_p + M_{tip} \underline{\phi}(L) \end{cases} \quad (11)$$

$$\begin{cases} K_T = \int_{V_s} y^2 \underline{\phi}^T(x) c_s \underline{\phi}(x) dV_s + \int_{V_p} y^2 \underline{\phi}^T(x) c^E \underline{\phi}(x) dV_p \\ \tilde{K} = P \int_L \underline{\phi}^T(x) \underline{\phi}(x) dx \end{cases} \quad (12)$$

where \tilde{K} is the additional stiffness induced by the applied preload condition.

The electromechanical coupling and the capacitance matrices are expressed as:

$$\begin{cases} \Theta = - \int_{V_p} y \underline{\phi}^T(x) e^T \underline{\psi}(y) dV_p \\ C_p = \int_{V_p} \underline{\psi}^T(y) \varepsilon^S \underline{\psi}(y) dV_p \end{cases} \quad (13)$$

The mechanical damping can be evaluated for a single mode analysis as:

$$C = 2\xi \sqrt{(K_T + \tilde{K})M} \quad (14)$$

where the damping ratio ξ is evaluated experimentally.

For more than one mode the damping ratio can be defined as follows:

$$C = \alpha(K_T + \tilde{K}) + \beta M \quad (15)$$

Incorporating the damping into Equation (10) yields the following generalized equations system for the studied setup:

$$\begin{cases} M_T \ddot{r}(t) + C \dot{r}(t) + (K_T + \tilde{K}) r(t) - \Theta v(t) = M^* f(t) \\ \Theta^T \dot{r}(t) + C_p \dot{v}(t) = \dot{q}(t) \end{cases} \quad (16)$$

Where $q(t)$ is the electric charge output of the piezoelectric PZT element that can be directly related to the power output through a load resistance R. The developed generalized model can accommodate all vibration modes.

EXPERIMENTAL SETUP AND MODEL VERIFICATION

Experimental Setup

To check the validity of the developed model, an experimental setup was built (Figure 4). The output voltage of the piezoelectric element was measured in frequency and time domains under constant acceleration input and varying pre-load conditions.

The experimental results were then compared to the predictions of the theoretical model. Variations of the voltage transfer function show the effect of the applied axial loading on the resonance frequency and amplitude. In all the experiments, a standard commercial bimorph piezoelectric sensor (SMBA4510T05M—from STEMINC Inc) was used. The materials' properties are summarized in Table 1. Figure 3 shows the sensor's geometry.

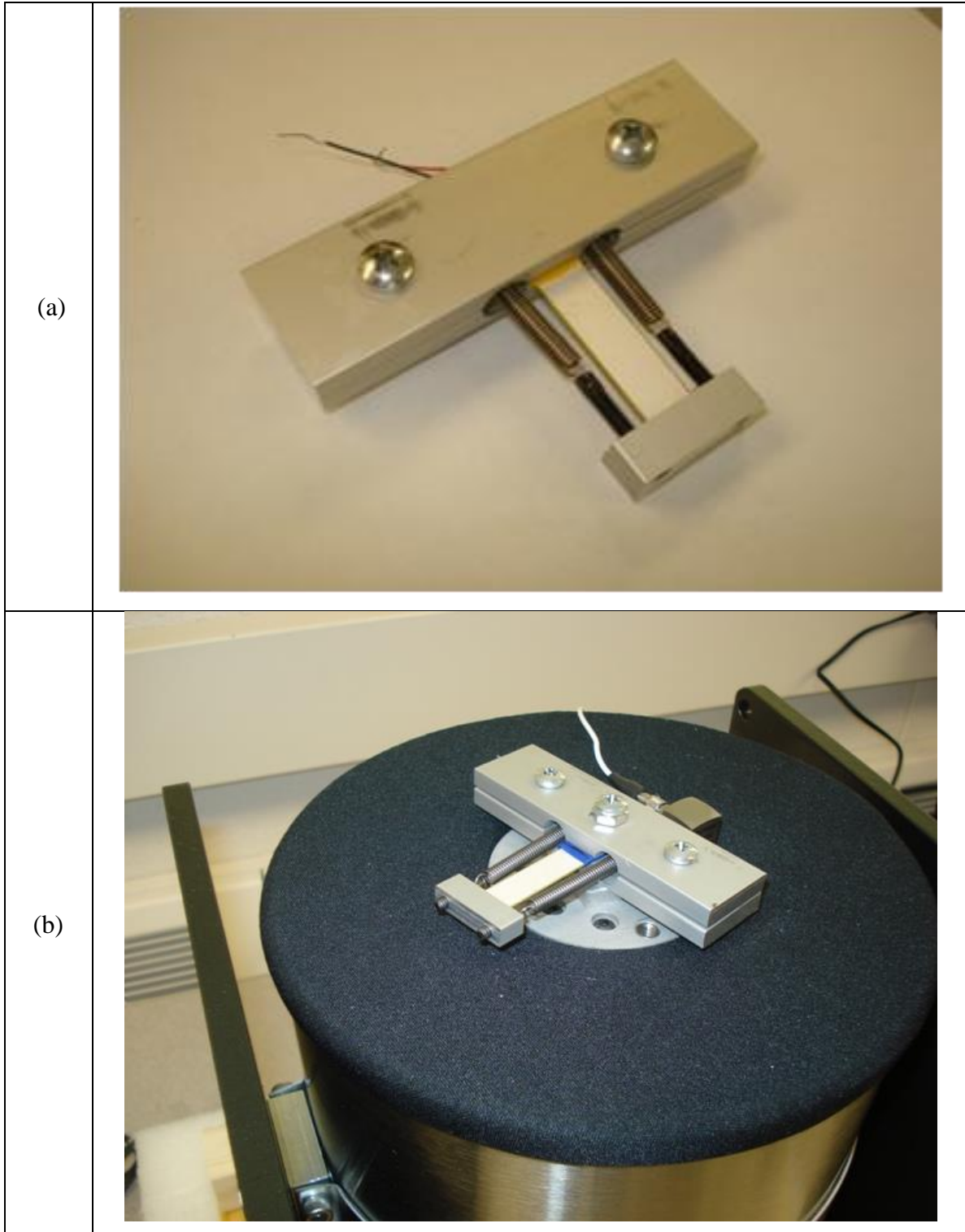


Figure 4. (a) Test setup, loaded piezoelectric bimorph beam with attached tip mass; (b) experimental apparatus mounted on a shaker for testing (For interpretation of the references to color in this and all other figures, the reader is referred to the electronic version of this dissertation).

In the developed system, shown in Figure 4(a), the preload is applied using two metallic springs connecting the tip of the beam to the base of the beam. Screws are used to adjust the preload. High precision linear springs were used. For each desired preload level, the springs' length (linear with respect to the preload level) is adjusted. The Euler's buckling load of a clamped-free beam is expressed as:

$$P_{cr} = \frac{\pi^2 EI}{4L^2} \quad (17)$$

If over loaded, the beam buckles and the piezoelectric ceramic cracks. The maximum tip deflection of the beam should not exceed 4mm peak-to-peak according to the manufacturer specifications. Ensuring these conditions is critical because if over-strained, the PZT will lose a significant fraction of its piezoelectric properties.

Model Verification and Experimental Results

The considered deflection shape mode in this work is assumed to have the following form (Elvin and Elvin, 2009):

$$\phi_i(x) = 1 - \cos\left(\frac{(2i-1)\pi x}{2L}\right) \quad (18)$$

The potential function is assumed to be constant over the PZT thickness and is expressed as follow:

$$\Psi(y) = \begin{cases} \frac{V}{a} \text{ if } \frac{h}{2} + a \geq y \geq \frac{h}{2} \text{ and } -\frac{V}{a} \text{ if } -a - \frac{h}{2} \geq y \geq -\frac{h}{2} \\ 0 & -\frac{h}{2} \geq y \geq \frac{h}{2} \end{cases} \quad (19)$$

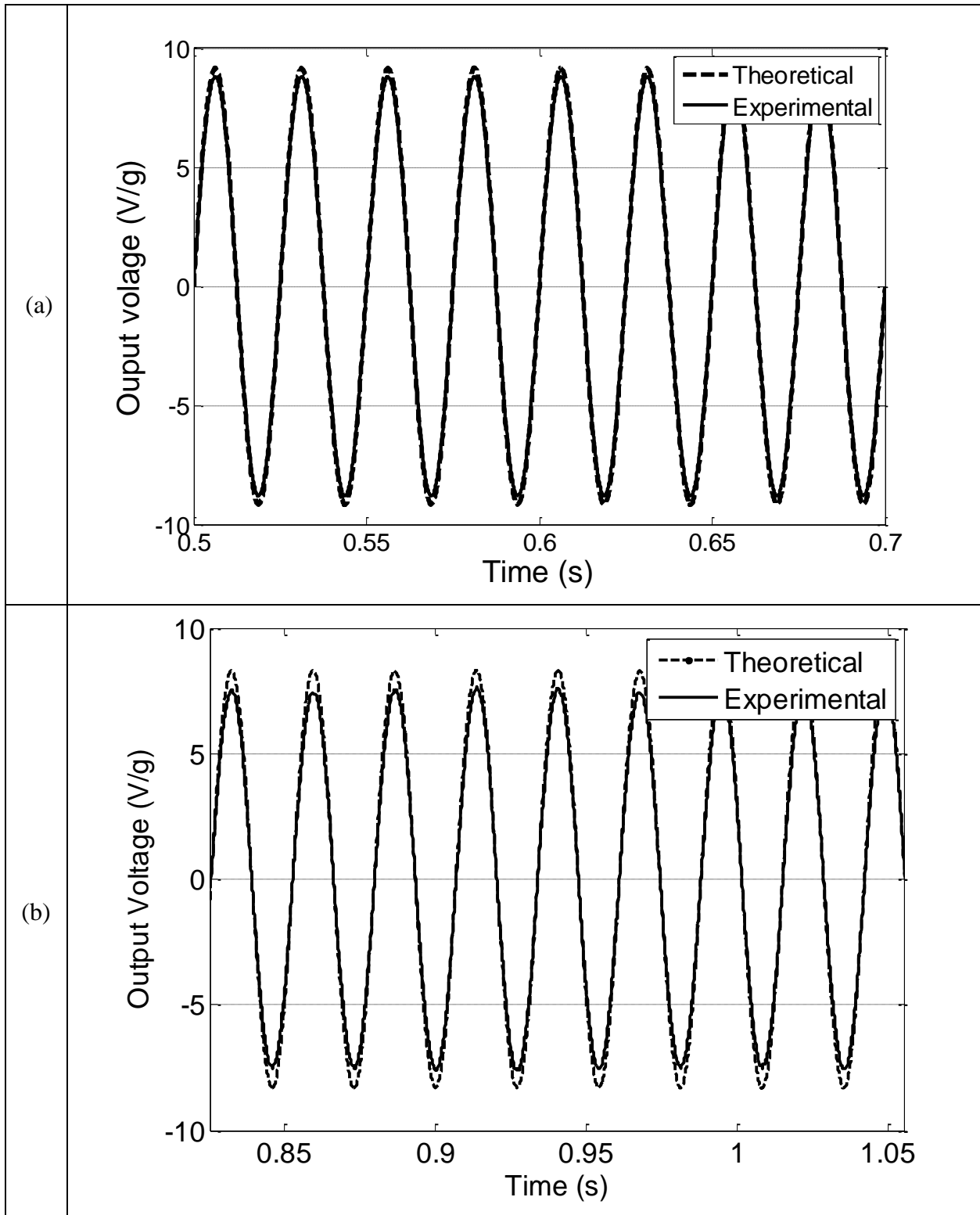


Figure 5. Predicted and measured output voltage across a $10M\Omega$ resistance (a) Frequency=40Hz, axial preload=-2N, tip mass=3.75g, (b) Frequency=37Hz, axial preload=-6N, tip mass=3.75g

A first set of experiments was conducted to compare the model predictions and the collected data for the time domain response under different configurations.

Figure 5(a) shows the measured and the predicted output voltage across a 10 MΩ load resistance for an excitation frequency of 40 Hz under a constant applied compressive axial loading of -2N. Less than 1 second of recording is shown for clarity. Different combinations of tip mass and axial loading conditions were tested at different excitation frequencies for accurate validation of the developed model. Figure 5(b) shows a second case of comparison at a loading frequency of 37 Hz and applied compressive constant loading of -6N. The results match, thus confirming the validity of the developed model.

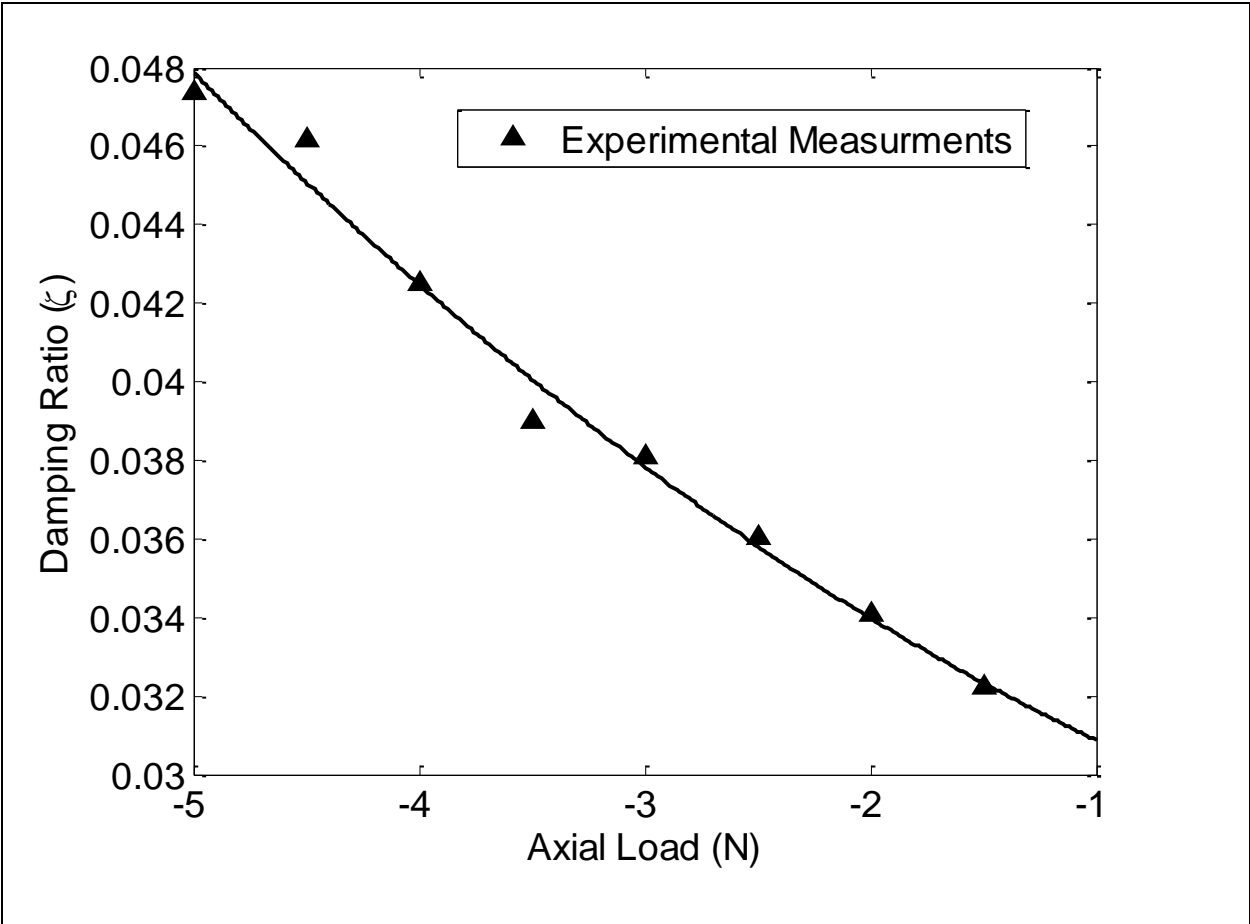


Figure 6. Variation of the first mode damping ratio with respect to applied axial loading

The variation of the damping ratio for the first vibration mode with respect to the applied preload was examined experimentally. The output voltage response of the system was measured under mechanical impulse excitation at different axial load levels ranging from -1 to -5 N. The damping ratio is then evaluated from the observed decay across a 10 M Ω load resistance. It is assumed that the damping ratio is constant over the frequency domain. Figure 6 shows the effects of preload on the damping ratio. It was observed that the damping ratio increases by more than 50% for a -5 N compressive loading. The measured damping ratio and the piezoelectric capacitance are injected into the analytical model in order to increase the accuracy of the numerical simulations.

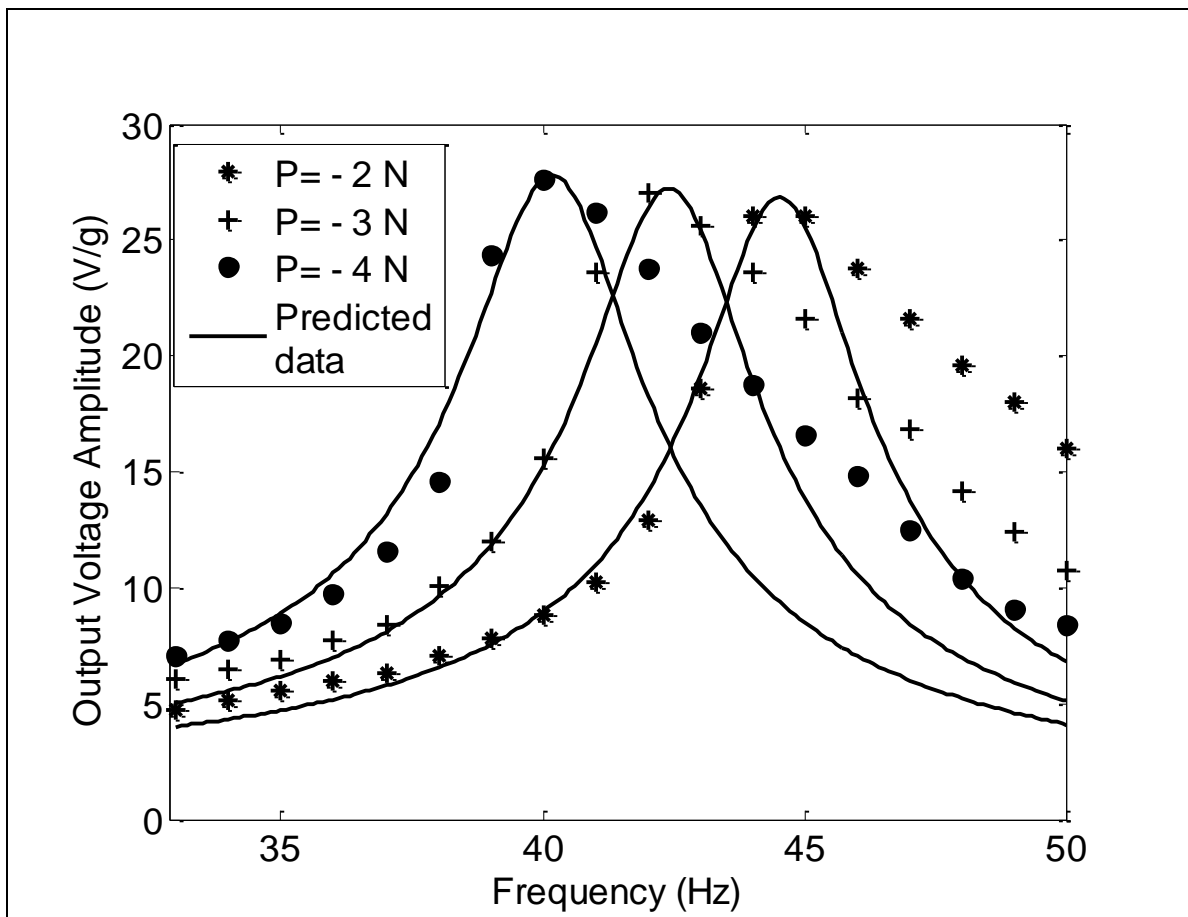


Figure 7. Output voltage transfer function of the transducer under different preload conditions. $M_{tip}=3.75g$, Load resistance=10M Ω . (solid: theoretical, dots: experimental).

The performance of the model was also evaluated in the frequency domain. The resonant frequency and the amplitude of the response were monitored for different applied axial loading. Figure 7 shows the measured and the computed voltage transfer functions of the resonator subjected to a compressive axial loading varying from -2 N to -4 N. The resonant frequency shifted from 44.5Hz to 40Hz. Only the first mode is shown in Figure 7.

As an example, it can be observed that when the energy harvester is designed for optimal response to base acceleration excitations centered at 45 Hz, a 3 Hz mismatch will induce a 50% reduction in the voltage response. This loss can be completely recovered through an adjustment of axial pre-loading of around 1.5N. The maximum response is constant despite the increase of the measured damping ratio. Experimental results shown in Figure 7 display a non-linear behavior with a prominent effect, especially for post-resonance frequencies. The high error after resonance can be explained by the softening nonlinearity in the piezoelectric resonator under high excitations (Erturk et al., 2010; Stanton et al., 2010).

TUNABLE ENERGY HARVESTING FROM AMBIENT VIBRATIONS IN CIVIL STRUCTURES

Maximum Harvestable Power Using Preloaded Harvester

Figure 8 presents a theoretical analysis of the variation in the resonant frequency response of the cantilever system as a function of the applied axial loading for different tip mass values. It can be observed that the effect of the axial loading on the resonant frequency (slope of the curves) is more prominent for lower mass values. Similarly, the higher the compressive loading, the lower is the effect of mass variations.

This is illustrated by the narrowing gap between the curves as the compressive loading is increased. These effects should be carefully considered while designing an energy harvesting resonator system.

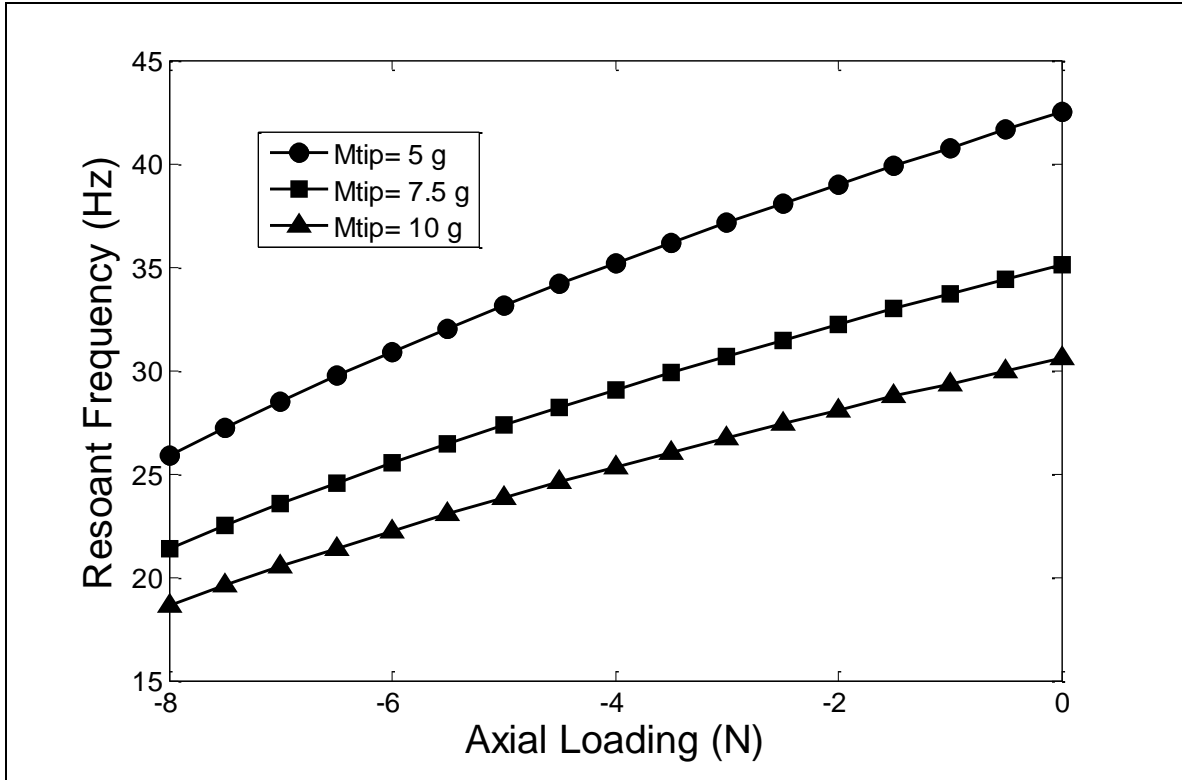


Figure 8. Resonant frequency variation with respect to applied axial loading for different tip mass (resistance $R=10M\Omega$)

Figure 9 shows the maximum generated power by a piezoelectric element as a function of the applied preload. The properties and dimensions of the piezoelectric are shown in Table 1. It is shown that by lowering the resonant frequency response of the piezoelectric device, slightly higher power is coupled through the system. This is also illustrated in Figure 7 (maximum voltage). It is observed that changes in the tip mass have a more prominent effect on the increase of the output power; this is due to the fact that a change in tip mass not only affects the resonant frequency but also the level of input work due base acceleration (Equation 11-b). Furthermore, it is shown that

frequency shifts due to mismatches (mechanical, environmental, etc), can be re-adjusted by varying the compressive loading to recover the loss in design power levels. It should be noted that all the shown numerical simulations' results are obtained using the material properties given in Table 1, under a constant amplitude acceleration input loading at 1 "g".

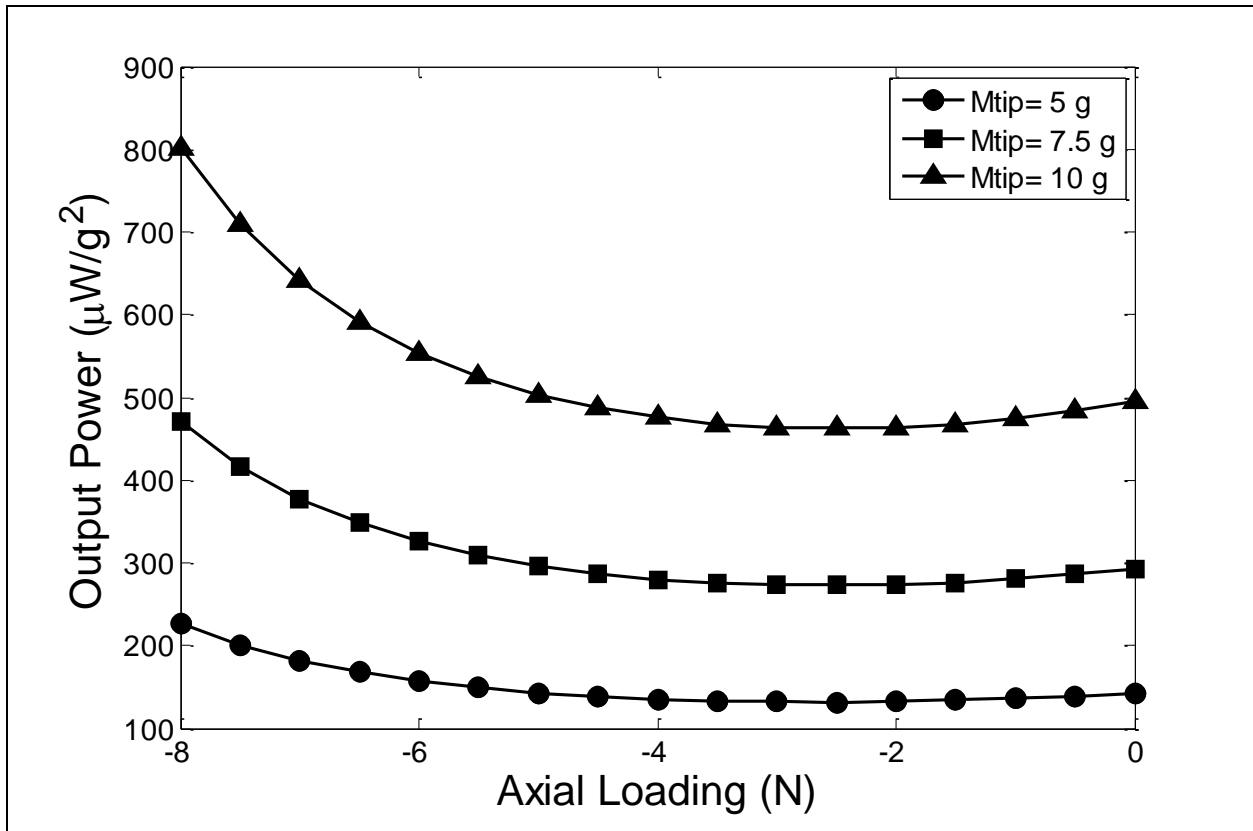


Figure 9. Maximum generated power with respect to applied axial loading for different tip mass (resistance $R=1\text{M}\Omega$).

Tunable Energy Harvesting from Civil Structures

Typical civil engineering structures exhibit fundamental vibration frequencies in a range below 10 Hz. The addition tip mass and axial loading shifts down the resonant frequency of a bimorph beam scavenger from its relatively high value at 157Hz. However, the maximum tip mass and deflections that the piezo-beam can accommodate are limited. The maximum volume of a

sensor node considered in this study, including the tip mass, is below 5 cm³. This relatively small volume is approximately the size of a large concrete aggregate (Issa et al. 2000), thus making the system suitable for embedment in, for example, concrete, without affecting the structural integrity of the host material.

In order to show the potential advantage of preload tuning, a set of study cases were conducted with the objective of evaluating the potential gains in harvested power under realistic excitation conditions on a civil structure. A set of extreme events – that is, earthquake recordings - were considered. Data were obtained from “the Earthquake Engineering Online Archive” of the University of California at Berkeley.

The energy output from the piezo-generator across a load resistance is evaluated using the following expression:

$$En = \int_0^{t_f} \frac{V^2(t)}{R} dt \quad (20)$$

Acceleration recordings from the deck of a 60 foot reinforced-concrete bridge under traffic loading (El-Borgi et al., 2005) were used as input excitation. The frequency spectrum of the measured accelerations is shown in Figure 10(a).

Obtained simulation results are illustrated in Figure 10(b). As the resonant frequency response of the harvester shifts closer to the dominant frequency of the bridge vibrations, more energy content is coupled to the resonator and harvestable power output increases considerably. For a system with a tip mass of 15 grams, the output power increases approximately a seven fold between the unloaded configuration and a system with an applied constant axial preload of -8 N.

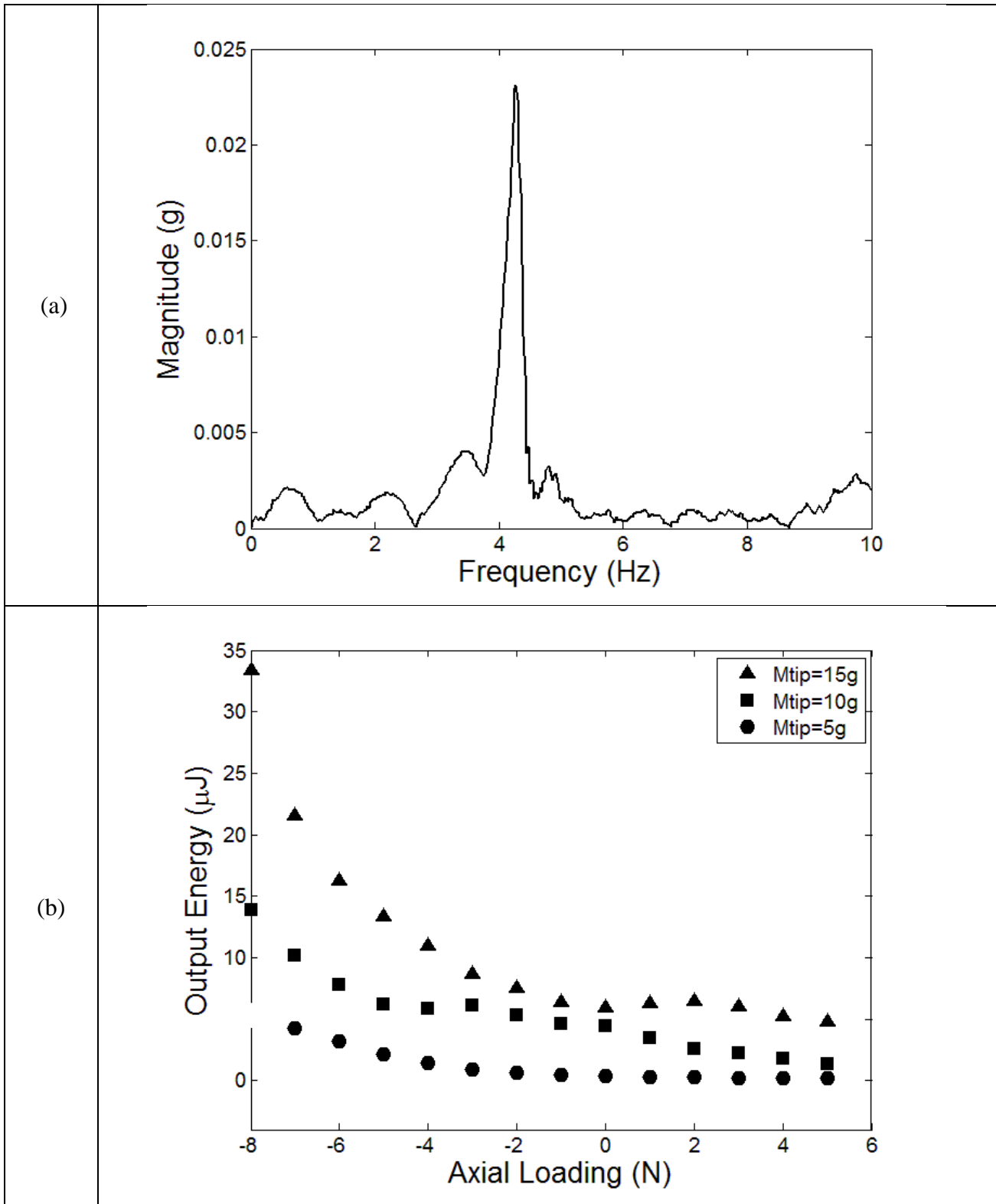


Figure 10. (a) Frequency spectrum for the acceleration measurements from the deck of a concrete bridge under traffic loading, (b) Variation of the output energy as a function of the applied preload subject to the recorded bridge accelerations (resistance $R=1M\Omega$)

Two different optimization analyses have been conducted: first, an optimization with respect to the tip mass and the resistive loading, and a second, analysis for the axially loaded confirmation with respect to the tip mass, the applied mechanical loading, and the resistive loading. The used optimization tolerances for the tip mass, the preload, and the electrical load are 0.5g, 0.1N, and 1k Ω , respectively.

Table 2. Optimized maximum collected energy for axially loaded and unloaded beam harvester configurations

| Earthquake event | Unloaded configuration | | Applied axial preloading | | |
|---------------------|--------------------------|--------------|--------------------------|--------------|-------------------|
| | Total output energy (uJ) | Tip mass (g) | Total output energy (uJ) | Tip mass (g) | Axial preload (N) |
| Llolleo (1985) | 485.18 | 25 | 5497.31 | 25 | -8.5 |
| El Salvador (2001) | 212.88 | 25 | 1422.13 | 22 | -7 |
| El Centro (1940) | 22.43 | 25 | 1150.38 | 25 | -10 |
| Northridge(1994) | 8.17 | 25 | 412.25 | 25 | -10 |
| Arthurs Pass (1995) | 8.21 | 25 | 343.46 | 25 | -9.5 |
| Nisqually (2001) | 7.55 | 25 | 329.72 | 25 | -10 |
| Valparaiso (1985) | 3065 | 17.5 | 8049 | 25 | -6.8 |

Results for the maximum harvestable energy from different earthquake events are presented in table 2. It is observed that the total transferred energy increases significantly with the added axial loading. A maximum mass of 25 grams was selected so that the overall constrain on the maximum volume can be verified. The buckling limit of the considered beam was also set as a constraining factor.

The buckling limit of the considered beam was also set as a constraining factor. It is also noted that for some cases, due to the frequency spectrum of the excitation, the response maximum can be caught on a secondary peak thus using only a portion of the maximum allowable mass. An example of such case can be illustrated in the response to the 1985 Valparaiso earthquake recording shown in Figure 11(a).

A secondary peak occurs within the range 0 to 25 grams mass, at a value of 17.5 grams as shown in Figure 11(c). The addition of an axial loading pushes the optimal response of the beam closer toward the main resonant component, thus resulting in a significant increase of collected energy while obeying the same volume and mass constraints. This is shown in Figure 11(c) in the loaded configuration response curve.

Figure 12 shows the average coupled power from different earthquake events with and without preloading condition. The shown averaged values of power are evaluated for optimized values of mass and axial loading. On average, the power output is 10 times more important with an added optimal preload.

In spite of that significant increase, and even though the total harvestable energy for such extreme events might seem to be high, the levels of continuous power remain critically low to allow for real time continuous recording of these events while relying only on harvested power. Only advanced, specific types of sensors, such as the data logger recently developed by the team, would allow for a self-powered processing of the generated vibration data.

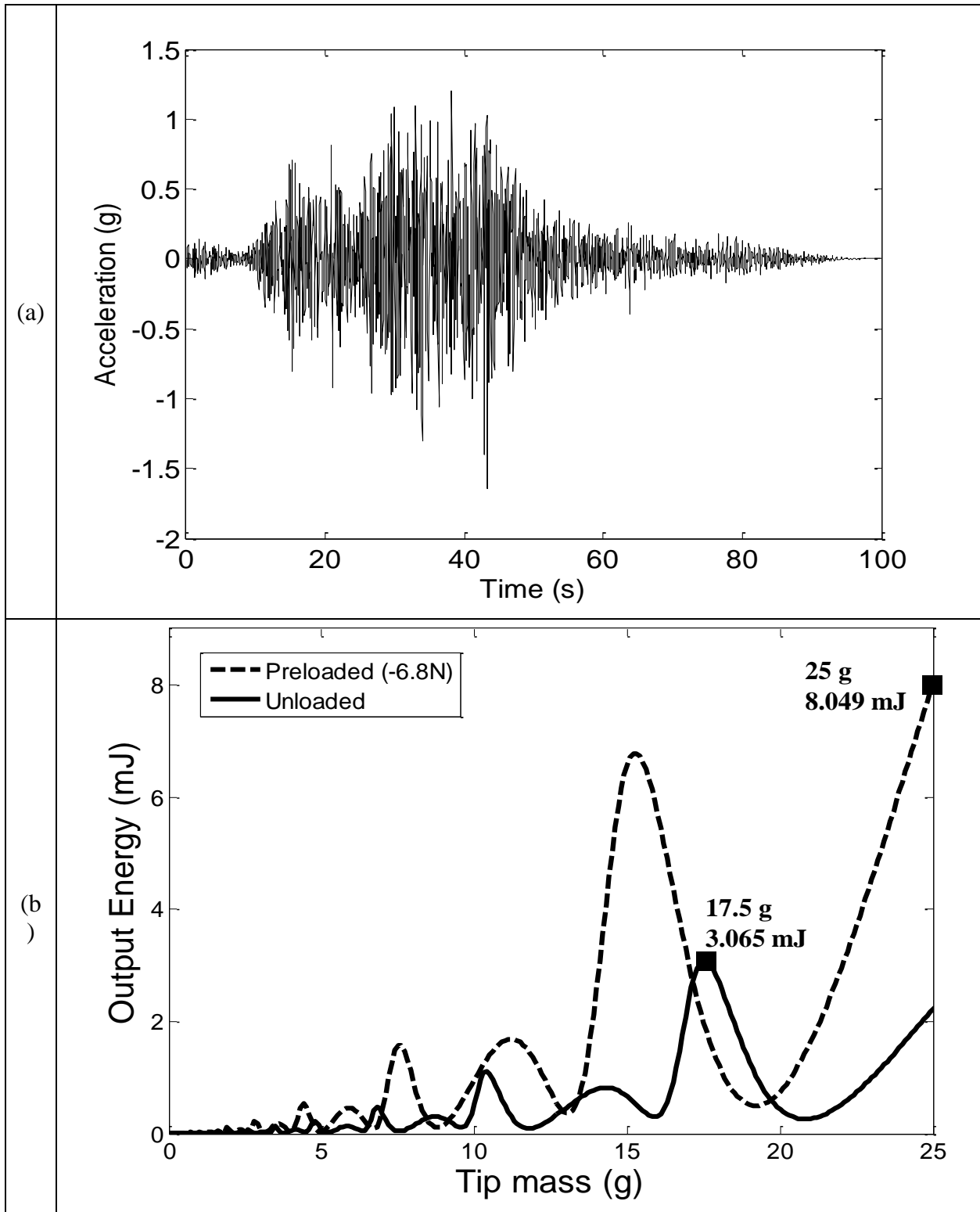


Figure 11. (a) Acceleration time-history from the 1985 Valparaiso earthquake, (c) Output energy with respect to tip mass for a loaded and unloaded system subject to the 1985 Valparaiso earthquake acceleration signal

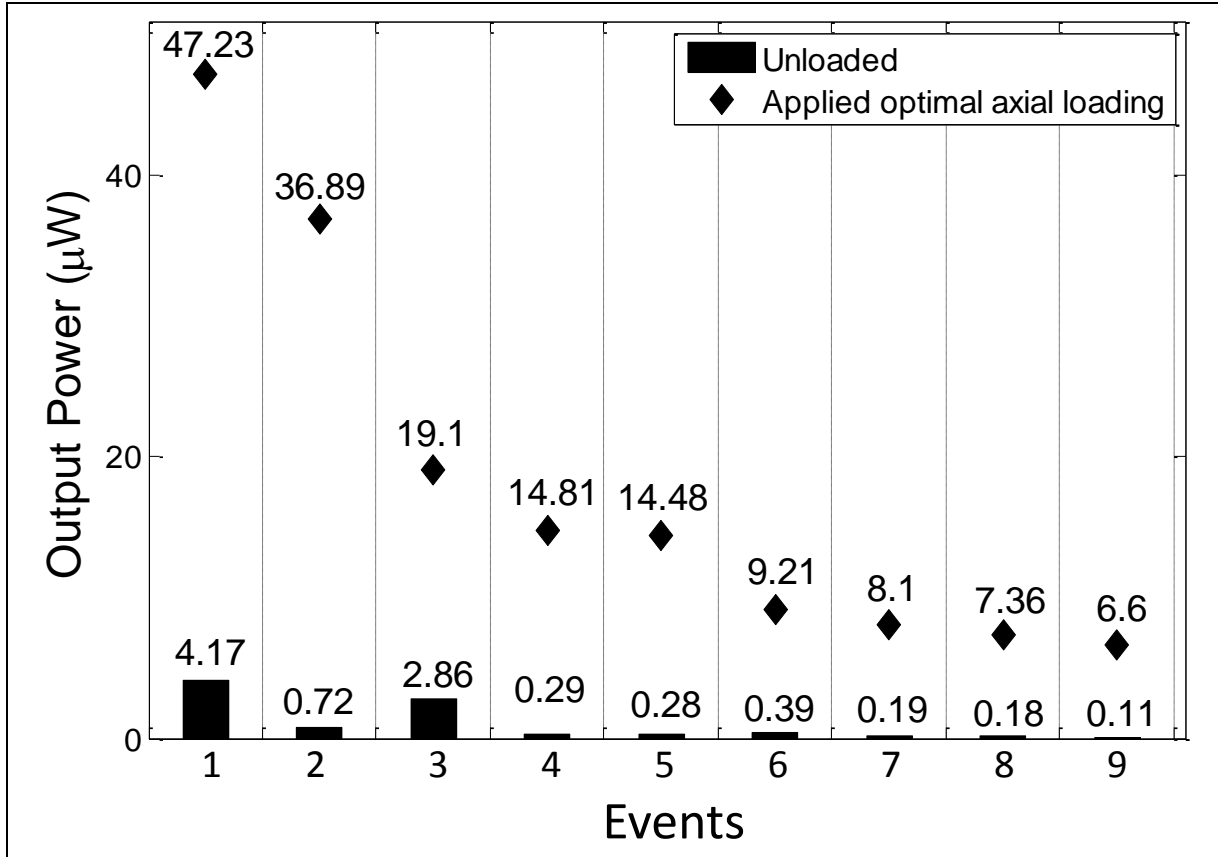


Figure 12. Average power output generated by a piezoelectric harvester (Table 1) subject to a set of example earthquake accelerations events for both the unloaded and with applied optimal axial loading configurations (Table 2) – 1: Lolleo, 2: Elcentro, 3: El Salvador, 4: Northridge, 5: Uttarkashi, 6: Rapel, 7: Arthur Pass, 8: Dharmasala, and 9: Xiang.

CONCLUSION

The above chapter focused on investigating the effect of preloading on the level of harvestable power from piezoelectric cantilever beam subjected to base excitation, in order to achieve a self-powered sensing system. A generalized model for a bimorph piezoelectric energy transducer mounted in a cantilever configuration and subject to permanent axial loading has been developed. The comprehensive model encompasses all the theoretical vibration modes of the beam and also takes into account the back coupling effect. A testing apparatus was built and tested for

different conditions. Obtained measurements showing the variations of the natural frequency and amplitude of the piezoelectric device response with varying preload validated the theoretical results. Realistic vibration recordings from earthquakes were used. Increases by 100 times in the output power levels were shown feasible through the application of -11 N of compressive axial loading.

It was also shown that tuning of vibration energy harvesters through axial preloading can be used to correct for mismatch induced effects. Such observed variations could be due to manufacturing mismatches or environmental effects (temperature, etc). The feasibility of a passive temperature effect compensator based on applied adjustments of an additional axial loading will be the focus of the next chapter.

CHAPTER 3: PASSIVE COMPENSATION OF TEMPERATURE EFFECT ON PIEZOELECTRIC ENERGY HARVESTING FROM VIBRATION

INTRODUCTION

Using preloading as a way of tuning the frequency response of the PZT harvester drastically increases the level of harvestable energy from vibration. However, several other obstacles still hinder their use in civil infrastructure. An important factor is mismatches induced due to temperature variations, as harvesters typically operate in a range varying from -20 to 50 degree Celsius.

In this chapter, the harvester's frequency response dependence to preloading is used to compensate for the observed temperature effects. Subsequently, we can partially recover the lost energy due to the induced mismatches. The main purpose is to develop a self-tuned piezoelectric energy harvester that can couple the maximum energy from vibration of civil structures in order to provide enough power for a successful implementation of self-powered vibration monitoring.

This chapter shows that passive compensation of temperature effects on piezoelectric vibrators is feasible using applied adjustments of axial preloading Shape Memory Alloy induced. Numerical and experimental analyses are performed to show the effect of varying temperatures on the voltage response of a bimorph cantilever piezoelectric energy harvester. A developed generalized modeling scheme, which employs a combination of temperatures and preloading, is presented. Based on this, the inclusion of shape memory alloys (SMAs) is proposed to achieve the

temperature correction, and thus a fully passive self-tuned vibration energy harvester. The proposed idea relies on the temperature dependence of SMAs to counteract the variations of the piezoelectric response induced by temperature change. SMAs are modeled using the one-dimensional constitutive behavior (Brinson (1993)). A proof of concept system that uses shape memory alloy wires is shown. Numerical analyses using optimal mechanism properties, which achieve the desired correction effects on a bimorph cantilever PZT-5H, are presented.

TEMPERATURE EFFECTS ON THE RESPONSE OF A BIMORPH PIEZOELECTRIC ENERGY HARVESTER

Effect of Temperature on the Material Properties

The stiffness matrix of the piezoelectric energy harvester shown in Equation (12) depends mainly on the elasticity modulus of the PZT material which varies with respect to temperature.

Figure 13 shows the dependence of the elastic modulus on temperature for PZT-5H. It can be seen that an increase in temperature will result in a decrease of the material's modulus. This relative softening of the material will induce a shift of the resonant frequency toward lower frequencies. Additionally, the overall response of the system also depends on the variations of the electrical properties and the mechanical-to-electrical coupling variables.

The dielectric constant varies with temperature (significant variations are observed for PZT-5H), which accounts for the strong dependence of the piezoelectric capacitance to temperature.

Figure 14(a) shows experimentally evaluated data of the dielectric constant variations for PZT-5H and PZT-5A piezoelectric ceramics. For PZT-5H, a variation of more than 50% is shown within the considered temperature range.

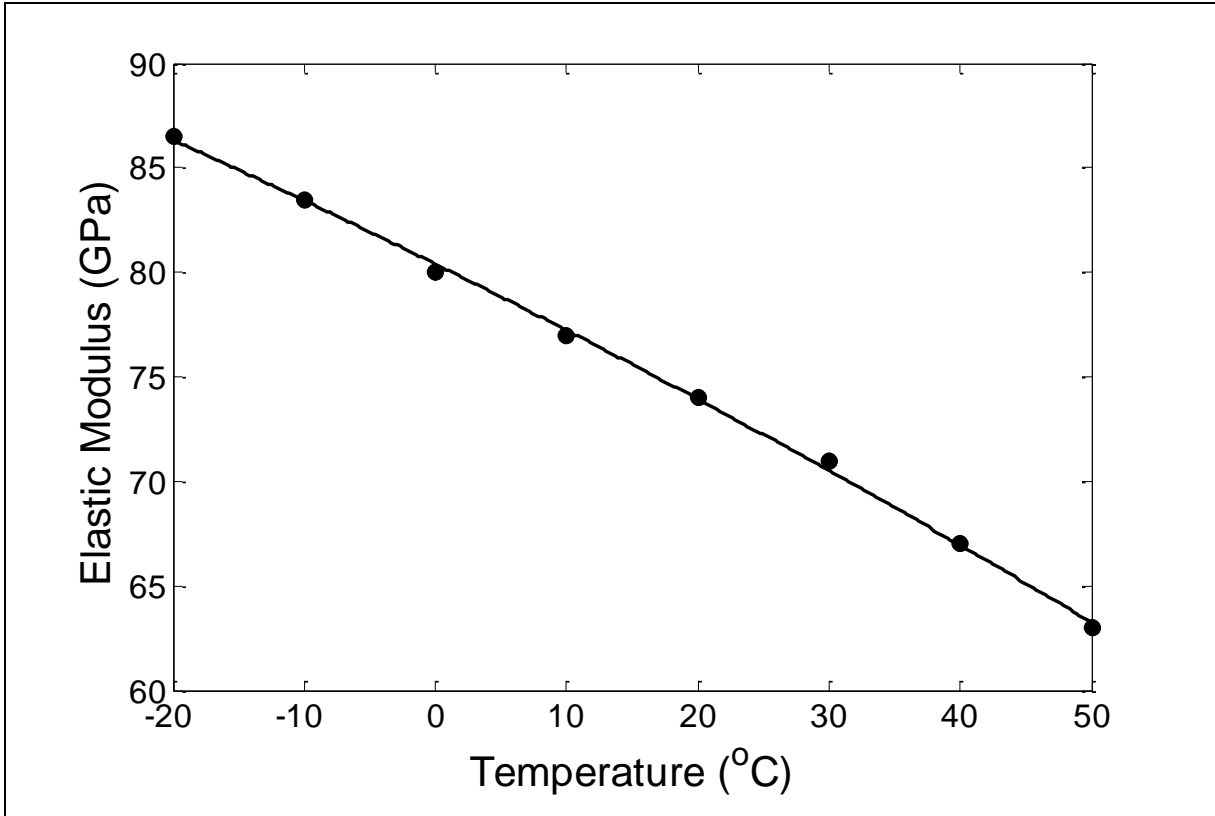


Figure 13. Temperature dependence of the elastic modulus of PZT-5H

Furthermore, in the considered cantilever configuration, the electromechanical coupling coefficient Θ is linearly dependent to the transverse strain constant d_{13} , which has a strong dependence to temperature as shown in Figure 14(b). A variation of more than 25 % of d_{13} is observed. The shown plots in Figure 14(a, b) were redrawn with parameters from experimental data obtained by Hooker, 1998.

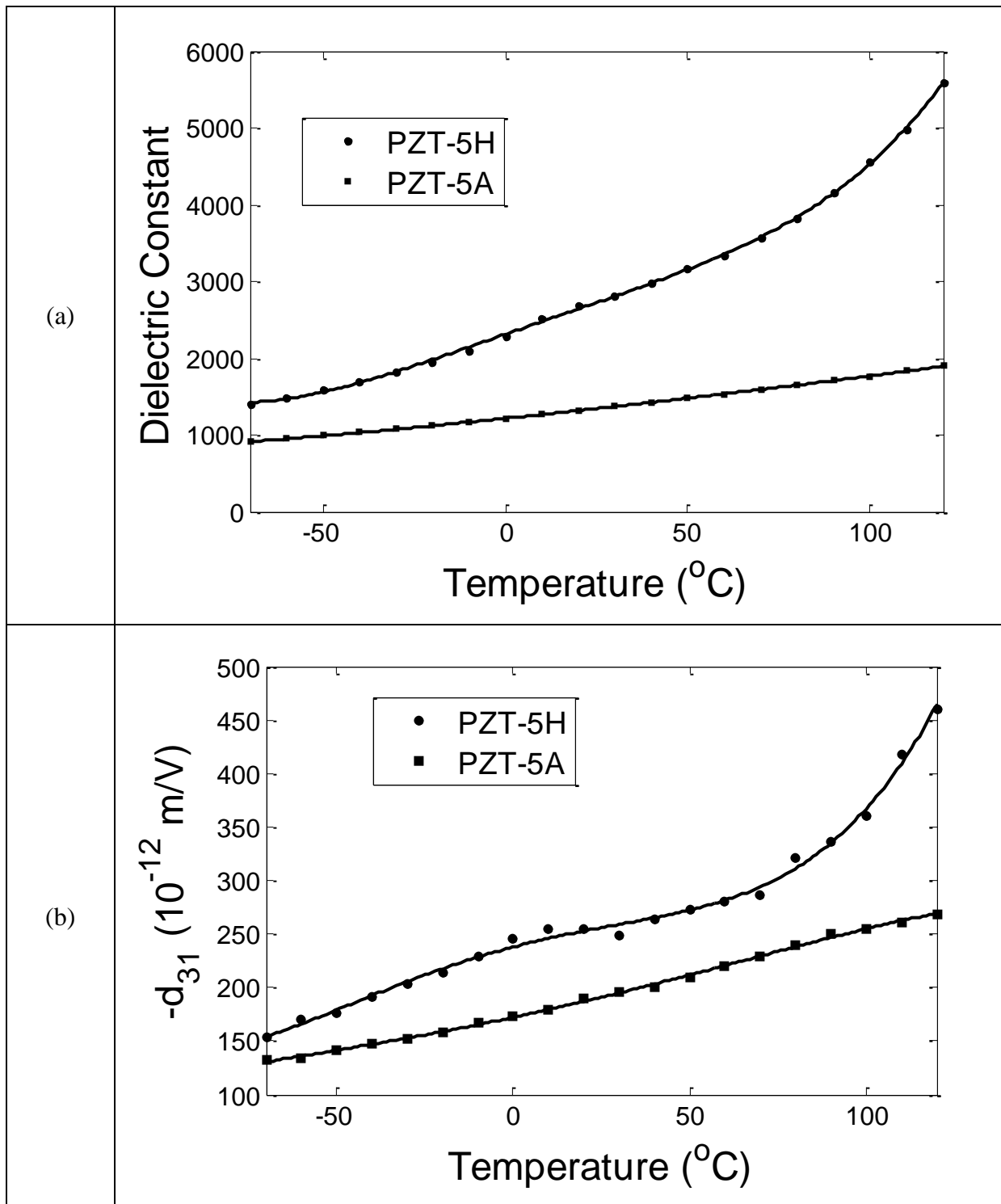


Figure 14. Temperature dependence of (a) the dielectric constant of PZT-5H and PZT-5A (Hooker, 1998), (b) the piezoelectric coefficient d_{31} of PZT-5H and PZT-5A (Hooker, 1998).

Effect of Temperature on Piezoelectric Energy Harvesting from Vibration

An experimental apparatus was built to check the validity of all the models used in this work. The setup is shown in Figure 15. The tested system geometry is shown in Figure 3. The first set of experiments was designed to determine the effect of temperature on the frequency response of the system. The output voltage transfer function of the piezoelectric element was measured under a constant applied acceleration at different temperatures.

Measurements were taken across a load resistance of $1\text{M}\Omega$. The base acceleration was kept constant at 1 g for an excitation frequency varying from 35 Hz to 55 Hz (a selected range around the resonant response of the system), and varying temperature from $-20\text{ }^{\circ}\text{C}$ to $40\text{ }^{\circ}\text{C}$.

A very pronounced effect is observed (Figure 16), on both the resonant frequency and the amplitude. An increase in temperature lowers the resonant frequency (material softening) and also lowers the maximum peak voltage amplitude at resonance, due to variations of the electrical and coupling properties. A resonance frequency shift between 41 and 49 Hz was observed for the considered temperature range. This shift, purely due to temperature, will induce practically a complete loss of the output amplitude for a resonating system tuned to respond around the peak at a selected temperature. This is due to the narrow-band response characteristic inherent to piezoelectric vibration harvesting devices.

Furthermore, it was observed that the damping ratio of the vibrator is affected by temperature. In fact, the temperature variation affects the elastic modulus of the material, leading to a change of the contact zone pressure between the piezoelectric beam and the base.

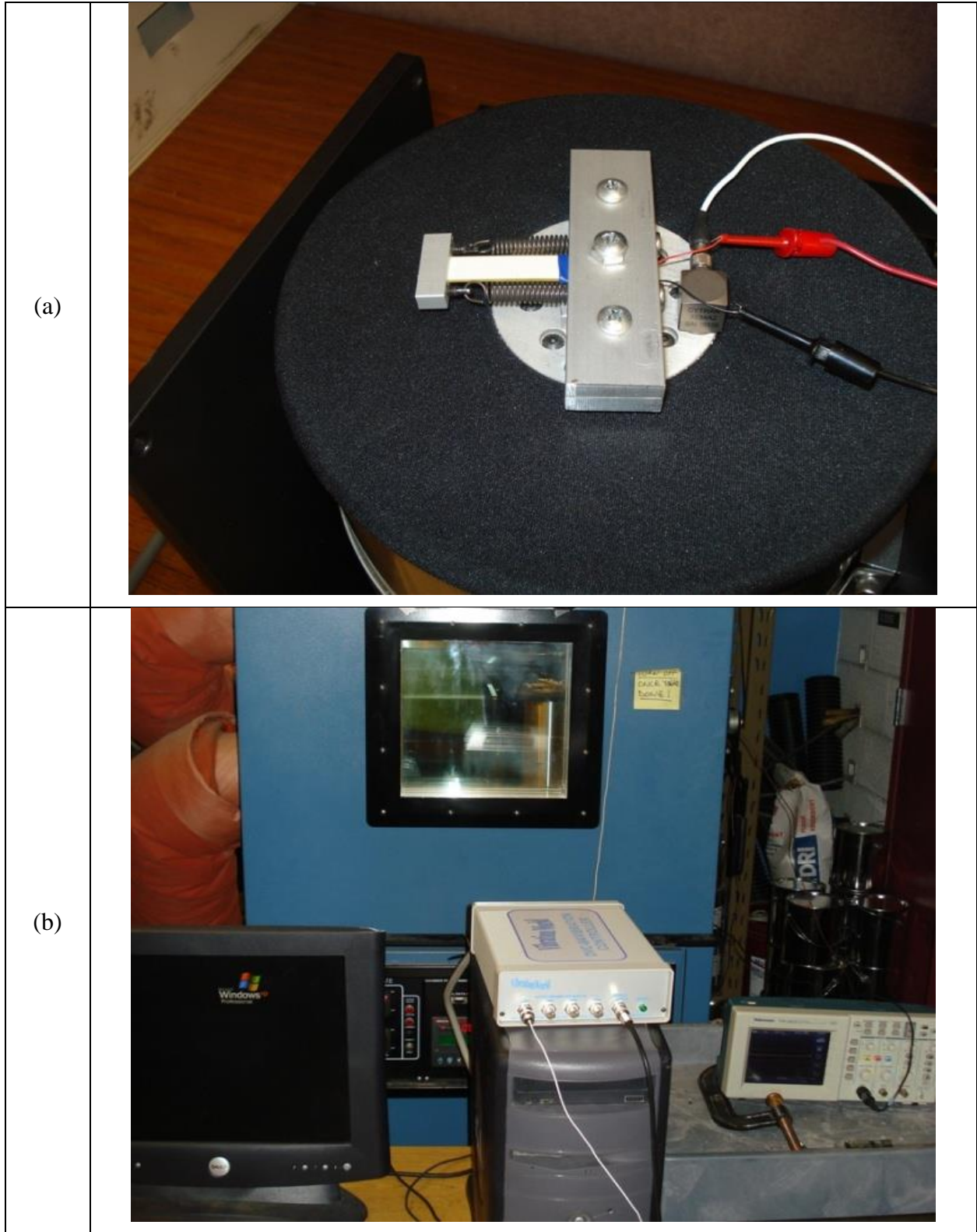


Figure 15. Test Setup: (a) loaded piezoelectric bimorph beam mounted on a shaker, with the SMA springs, (b) experimental apparatus enclosed in an environmental chamber

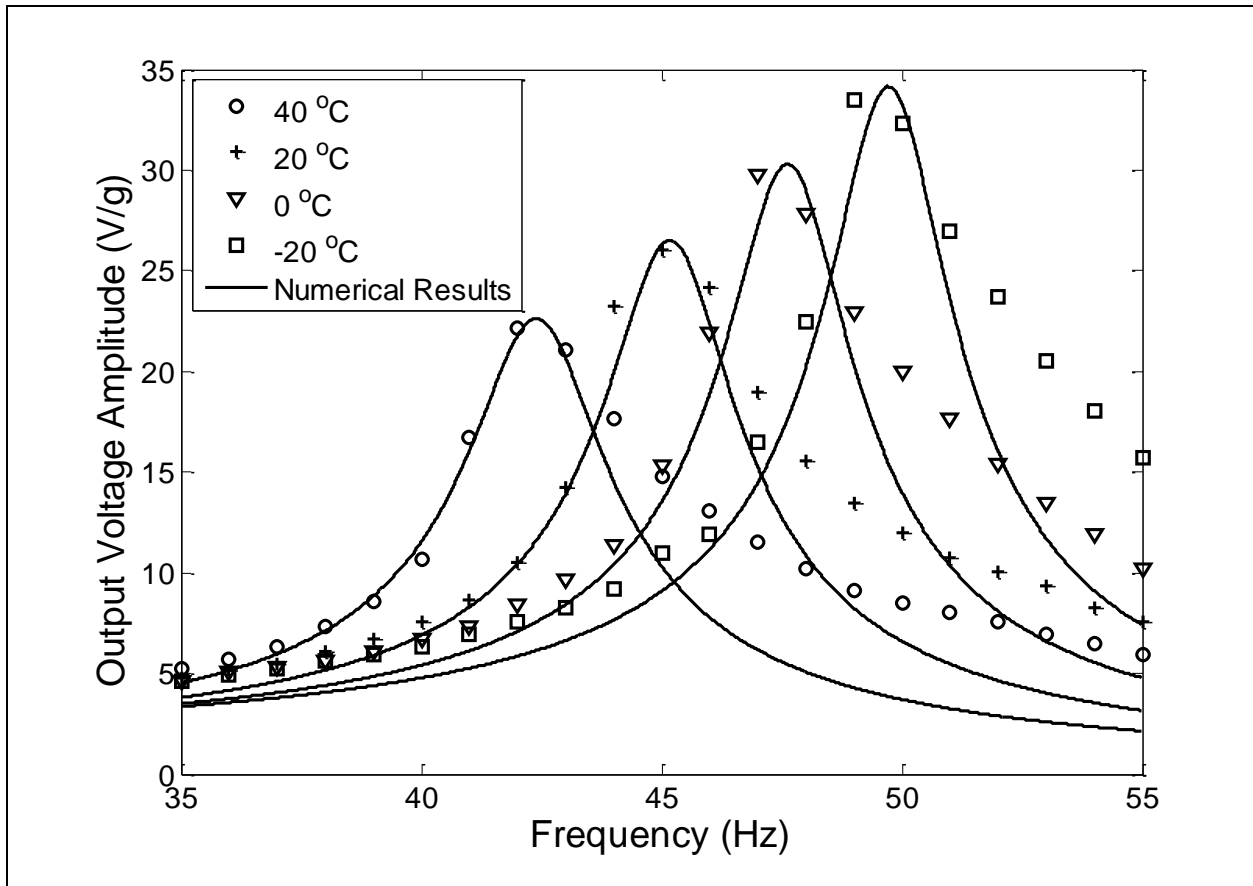


Figure 16. Numerical results and experimental measurements of the output voltage amplitude versus the excitation frequency at different temperatures, under a 1g base acceleration. (Mtip=3.75g, load resistance=1MΩ)

Figure 17 shows this effect measured experimentally for the first vibration mode of the cantilevered beam. It was shown that the damping ratio increases by about 40% for a temperature change from -20 °C to 40 °C. This increase and the observed peak amplitude decrease, induced by the material's properties changes, combine to further reduce the obtained output response. The experimental measurements of the damping were injected into the analytical model in order to enhance the accuracy of the implemented numerical simulations.

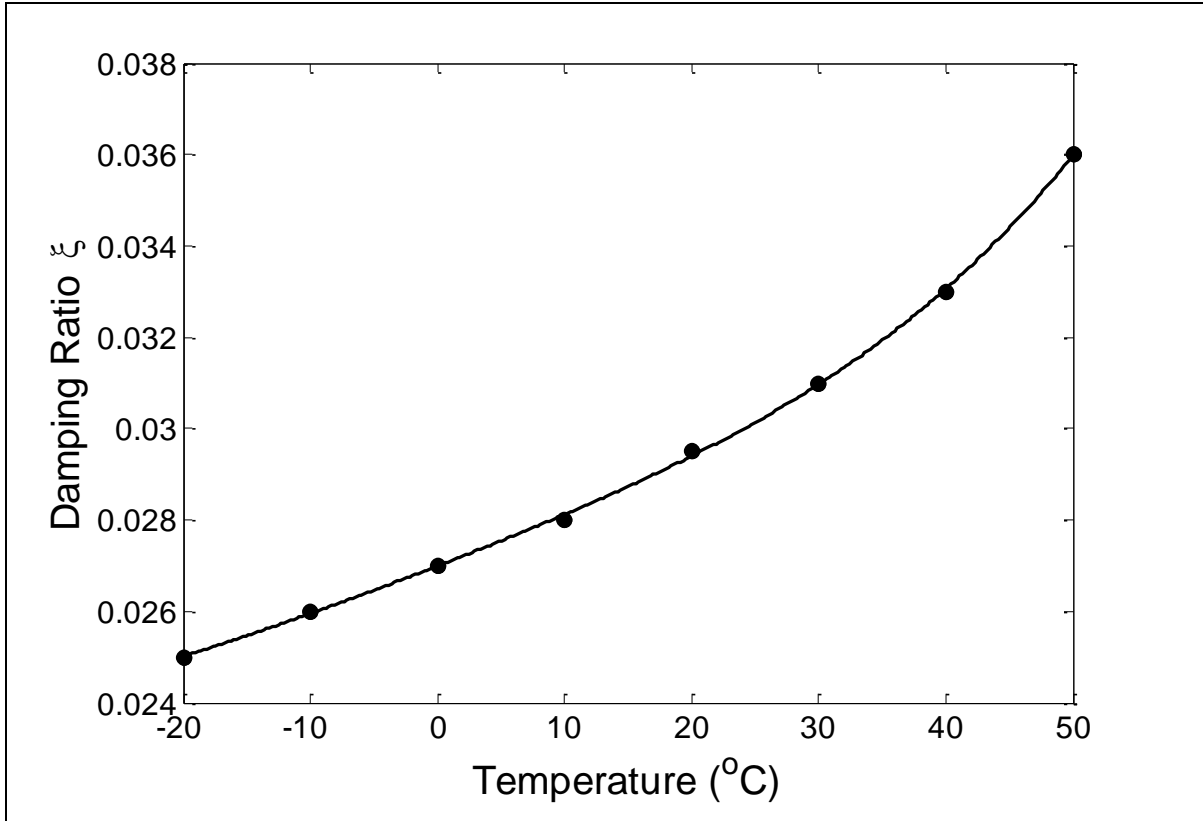


Figure 17. Variation of the first vibration mode damping ratio with respect to temperature

TEMPERATURE EFFECTS CORRECTION USING AXIAL PRELOADING

Experimental Setup

In this section, the alteration of stiffness of the vibrating device is studied in order to counteract the observed effects due to temperature variations. The objective is to maintain the natural frequency of the system around a desired spectrum for varying temperatures in the considered range. A mechanical tuning mechanism is considered. The principle is based on the application of a variable axial loading, which will change the beam stiffness and subsequently affect the resonant frequency of the piezoelectric transducer. The technique employs the effect of

these mechanical adjustments in order to compensate for the observed deviations due to temperature.

The obtained results from the previous chapter clearly show that by applying either compressive or tension axial loading, it is possible to regulate the frequency response of the vibrator and tune its resonant response to a desired range. Capitalizing on this effect, it is deduced that the observed deviations due to variations of the ambient temperature can be compensated. The natural resonance characteristic can be re-shifted to match the input excitation spectrum as the temperature tries to push it away.

In the shown results, 20 degrees Celsius is selected as a reference temperature. A decrease in temperature will stiffen the PZT and shift the cantilever resonant frequency toward higher frequencies, a compressive axial loading is then needed to shift it back to lower values. On the other direction, an increase in temperature shifts the cantilever resonant frequency toward lower frequencies, and a tensile axial load will regulate it back toward higher values.

A second set of experiments were conducted to validate the updated model (including the mechanical loading) and to verify the correction effect. The setup is shown in Figure 3. A set of springs connect the tip mass to the base of the vibrator. Adjustable screws are used to vary the tension in the spring and induce a tunable axial loading in the system. The resonant frequency at the selected reference temperature of 20 °C, corresponding to the used system (Table 1), was measured to be 45 Hz for a system subjected to an initial compressive axial preloading of 2 N.

Preliminary Result: Temperature Compensation Using Preload

In the first run, the temperature was decreased to 0 °C. The resonant frequency shifted to 47.6 Hz inducing more than a 40% reduction in the output voltage response evaluated across a 1 M Ω load resistance. Measured transfer functions (Figure 18(a)) show that the temperature induced shift of the resonant frequency can be corrected, meaning an adjustment of the axial loading through the application of an additional 1.2 N compressive axial loading, thus increasing the total load to 3.2 N and counteracting the temperature effect. Furthermore, the voltage loss can be completely recovered. The additional compressive loading reduces the overall stiffness of the system, hence allowing for increased maximum deflections and peak response voltages.

For the second considered case, the temperature was increased to 40 °C starting from the same reference point at 20 °C. The heating induced a decrease of the resonant frequency response to 42 Hz. Figure 18(b) also shows that a reduction of the applied axial force by 1.2 N to a new tuning point at 0.8 N compressive force (the initial reference point was at 2 N applied compressive loading) induced a total resetting of the resonant frequency response. But in this case, only a portion of the loss in the amplitude voltage is recovered since the tuning increased the stiffness and in turn affected the allowable maximum deflection range under the same input excitation force.

Figures 18(a) and (b) present both experimental measurements and theoretical results obtained using the model developed above. These experiments prove the validity of the tuning concept and verify the accuracy of the considered models

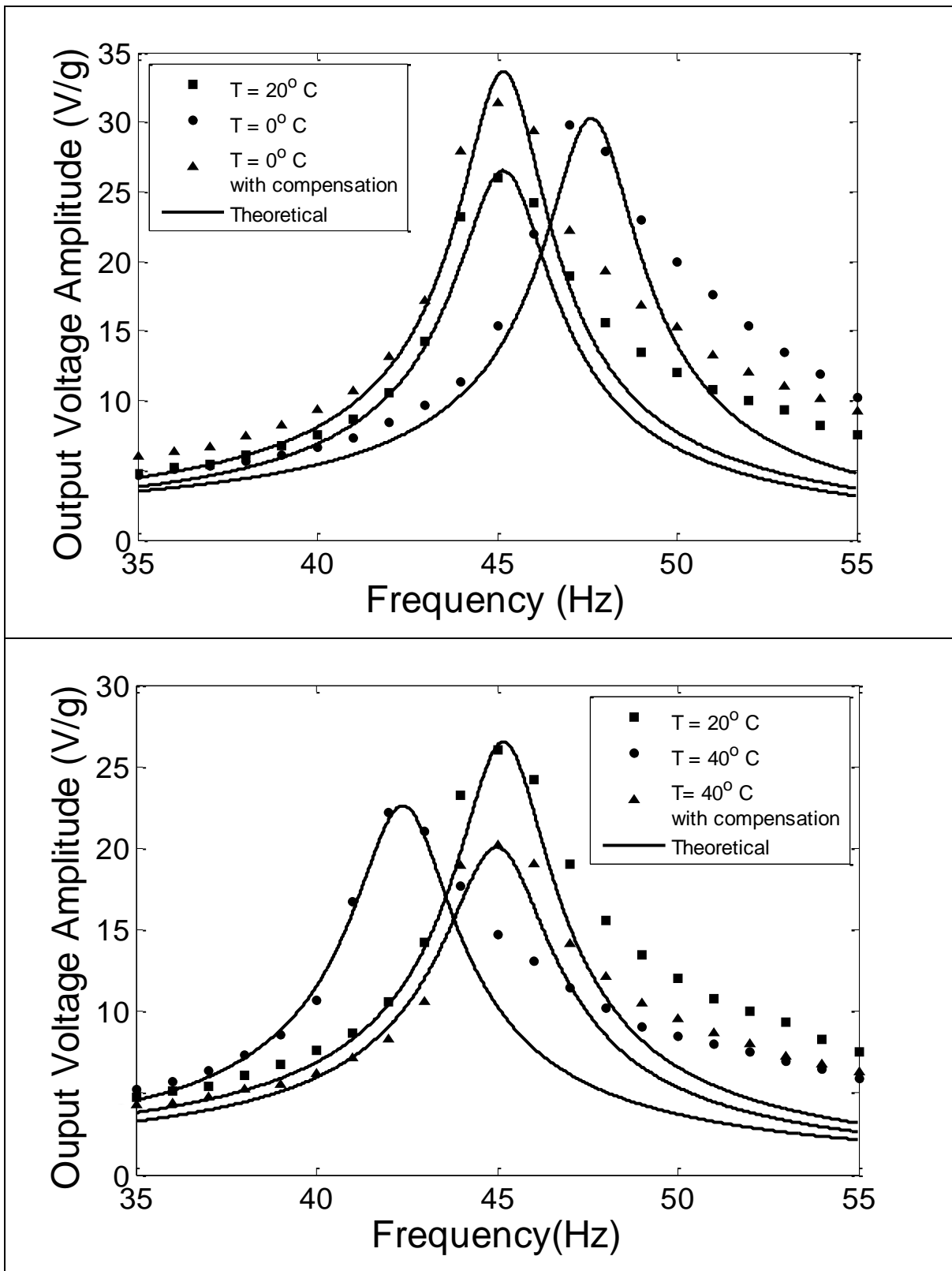


Figure 18. Temperature compensation for a variation from the 20° C reference to (a) 0° C, (b) 40° C. ($M_{tip}=3.75g$, load resistance= $1M\Omega$)

As observed in Figures 18(a) and (b), under certain configurations the loss due to temperature cannot be completely recovered by varying the load. In fact, a temperature increase induces an amplitude decrease in addition to the frequency shift. Furthermore, when trying to correct for the shift, the needed stiffness increase will also reduce the maximum response. This effect is illustrated in Figure 18(b). In spite of this behavior, it is shown in the conducted experiment that up to 60% of the amplitude is recovered. The effects are exactly the opposite for a decrease of temperature compared to the reference point.

This explains the measured peaks in Figure 18(a), which are higher after tuning than the original reference. Following these observations, it is concluded that the selection of the initial reference, the one at which the system is designed, is critical toward efficient correction. For example, the reference temperature should be the highest in the considered range for a piezo that softens when temperature increase (PZT-5H), and the lowest for a piezo material that exhibit an opposite behavior. Further analyses are required to establish proper design guidelines.

PASSIVE SELF-TUNED HARVESTER USING SHAPE MEMORY ALLOY EFFECT

Passive Self-Tuned Harvester Design

As previously discussed, systems that require constant corrections, either through mechanical or electrical input, are impractical as energy harvesting modules. The need for an external power in order to adjust the control mechanism makes it impractical. In this section, I propose a method to design a self-correcting energy harvester. The method combines shape memory alloys (SMAs) with the active piezoelectric transducer. It relies on the temperature effect in these SMAs to counteract the variations induced in the piezoelectric device.

Inherent characteristics found in Shape memory alloys allow them to exhibit large strains deformation under temperature variation. This behavior is reversible when the applied stress in the material is kept above a critical limit defined by the material properties. The described concept here is to adjust the frequency response shifts observed in the piezoelectric vibrator under varying temperature, meaning an applied axial loading generated by deformations in a set of SMA wires that are induced by the same temperature variations. The tuned system then exhibits a fully-passive self-correcting behavior. Obtained results using the presented preliminary experimental setup show that the temperature effects are not fully recovered. This is due to the hysteresis nature of the SMA, and the fact that simple, commercially available SMA springs were used in the proof of concept setup. But, it is also shown that the properties of the alloy can be optimized to match the used piezo material characteristics, and achieve then an optimal loss recovery.

Figure 19 shows the considered configurations. The SMA wires are initially pre-stressed. When the temperature changes, the wires induce large strains satisfying the following equation:

$$(\sigma_i - \sigma)A - (\varepsilon - \varepsilon_i)LK = 0 \quad \text{Compressive mechanism (Figure 19(a))} \quad (21\text{-a})$$

$$(\sigma_i - \sigma)A + (\varepsilon - \varepsilon_i)LK = 0 \quad \text{Tensile mechanism (Figure 19(b))} \quad (21\text{-b})$$

where A is the wire cross section, L is the wire length, K is the spring stiffness, σ and ε are respectively the stress and strain within the wire, and the subscript i refer to the initial condition.

The one dimensional constitutive model (Funakubo, 1987) is used in this study. The mechanical behavior of the SMAs is described by the following system of equations:

$$\sigma - \sigma_0 = D(\xi)(\varepsilon - \varepsilon_0) + \Omega(\xi)(\xi_S - \xi_{S0}) + \Theta(T - T_0) \quad (22)$$

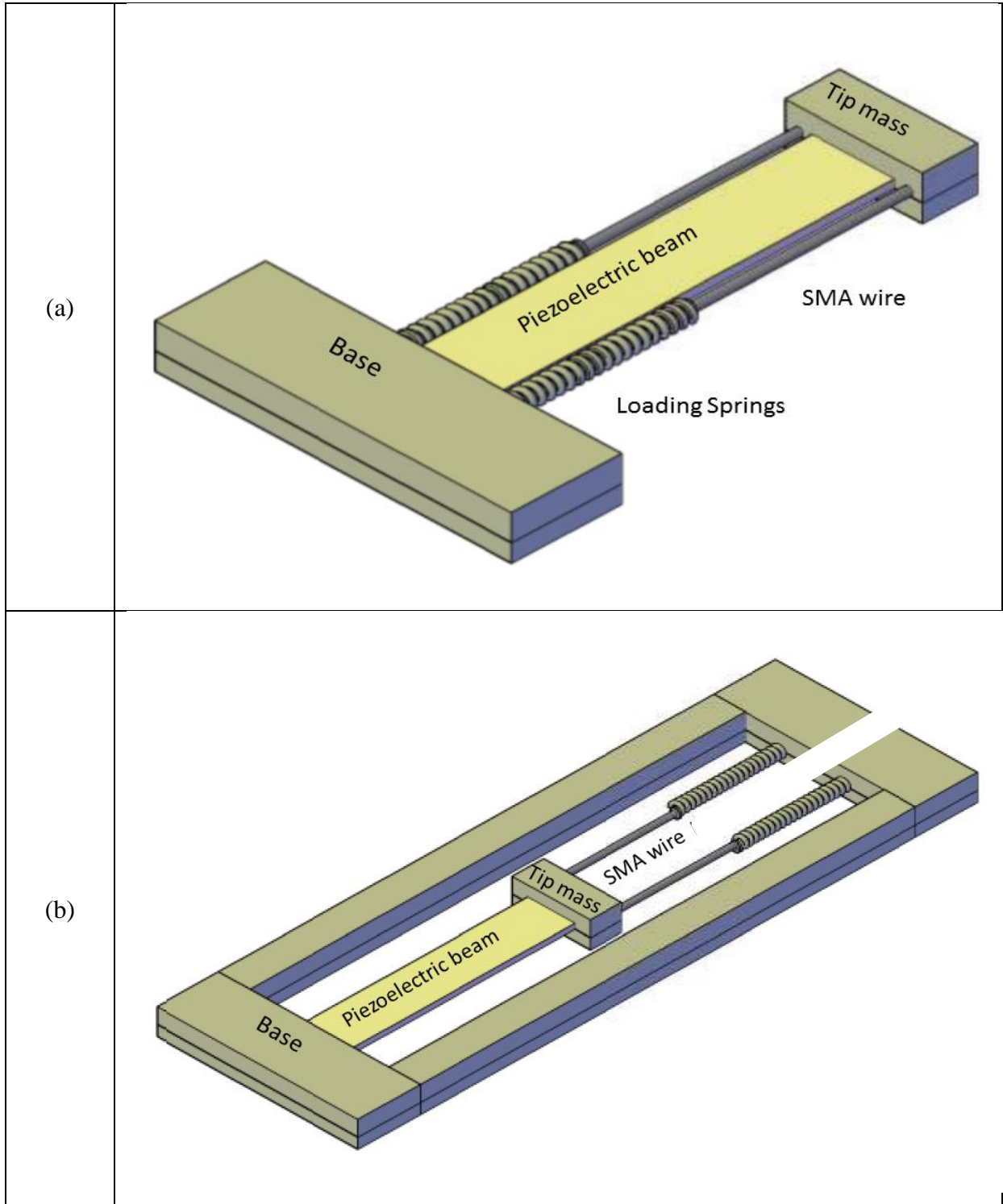


Figure 19. Schematic depiction of a piezoelectric beam with attached SMA axial loading mechanism, (a) compression mechanism, (b) tension mechanism.

Ω is the transformation tensor, Θ is related to the thermal coefficient of expansion of the SMA, ξ is the martensite fraction of the material, ξ_s denotes the stress induced single martensitic variant fraction, and D is the modulus of the SMA material which is defined as follows:

$$D(\xi) = D_a + \xi(D_m - D_a) \quad (23)$$

where D_a is the modulus of the SMA at 100% martensite and D_m is the modulus at 100% austenite. The detailed phase's transformations equations can be found in Brinson (1993).

In the experimental setup, the SMA wires are initially pre-stressed using the springs beyond the critical stress needed so that they will exhibit reversible transformations with the temperature changes according to Funakubo, 1987. This parameters are material property (Brinson, 1993). When the temperature varies, the strain ε within the wire is evaluated using equations (21), (22), (23) and the model's specific phase transformations equations. The total induced axial load is then evaluated as function of temperature as follow:

$$P(T) = \sigma A = \varepsilon LK \quad (24)$$

Self-Tuned Vibration Energy Harvester

The induced change in the piezoelectric beam stiffness due to applied axial load is calculated using Equation (12). Finally, the modified voltage transfer function is evaluated, as shown in the model described in section 2. For design purposes, once the dependence of the piezoelectric to temperature is known, the SMA parameters can be optimized and ultimately tailored in order to minimize the total stiffness change and the shift of the resonant frequency. Commercial SMA Springs were used without an optimization of their parameters. The objective

of the simplified setup is to prove that the changes in the frequency response of the piezoelectric vibrator using the SMA springs, due to temperature, can be predicted and controlled.

When the temperature increases, the SMA wires shorten, inducing compressive or tensile axial loading depending on the adopted configuration (Figure 19(a, b)). If PZT-5H is used as the transducer, it will soften during an increase in temperature thus causing a shift of the system's resonant frequency toward lower level. Based on the SMA behavior described above, if mounted in the tensile configuration (Figure 19(b)), the induced axial load will shift it back, recovering most of the observed losses. Other piezo materials can also be used, such as the hard PZT (EC-69). These materials will harden under a temperature increase in the considered range. Their elastic compliance decreases by as much as 25% for an increase in temperature from -20 °C to 40 °C (Sabat et al., 2007). This behavior will shift the resonant frequency toward higher levels. The compressive mechanism (Figure 19(a)) is then needed to use the stresses in the SMA wires and shift the resonance point back to around its initial reference level.

As discussed, simple SMA wires were considered in the work reported. Thus, only an optimization with respect to the spring stiffness, the length, and the cross section of the wires, and also the transformation temperature, were considered. The transformation constants, C_M and C_A , are assumed to be equal. All of the other material properties used in the simulations are defined in Table 3. PZT-5H piezoelectric is also considered for this study. As previously discussed, the tensile configuration is used for temperature compensation in all the simulations. To demonstrate this combined effect, a reference temperature at -20 °C is selected. The resonant frequency at the reference frequency for the used system is 49.5 Hz. For a free piezoelectric vibrator transducer (no SMA loading), the resonant frequency shifts down to 40.9 Hz at 50 °C, inducing a 90% reduction in the output voltage response evaluated across a 1 M Ω load resistance at that temperature.

Numerical Analysis

Figure 20 shows the variation of the optimum calculated axial load (tension) as a function of temperature using two SMA wires, which have the properties shown in Table 3, and a spring of stiffness 1900N/m.

Table 3. Material properties of the SMA wires used in the simulations.

| Transformation temperatures | Transformation constants |
|---|---|
| $M_f = -37\text{ }^\circ\text{C}$ | $C_m = 13.88\text{ MPa}/^\circ\text{C}$ |
| $M_s = -22\text{ }^\circ\text{C}$ | $C_a = 13.8\text{ MPa}/^\circ\text{C}$ |
| $A_s = -21\text{ }^\circ\text{C}$ | $\sigma_s^{cr} = 100\text{ MPa}$ |
| $A_f = 6\text{ }^\circ\text{C}$ | $\sigma_f^{cr} = 170\text{ MPa}$ |
| $D_a = 67\text{ MPa}$ | $\varepsilon_L = 0.067$ |
| $D_m = 26.3\text{ MPa}$ | Length $L = 0.03\text{ m}$ |
| $\Omega = 0.55\text{ MPa}/^\circ\text{C}$ | Cross section $A = 10\text{ }\mu\text{m}$ |

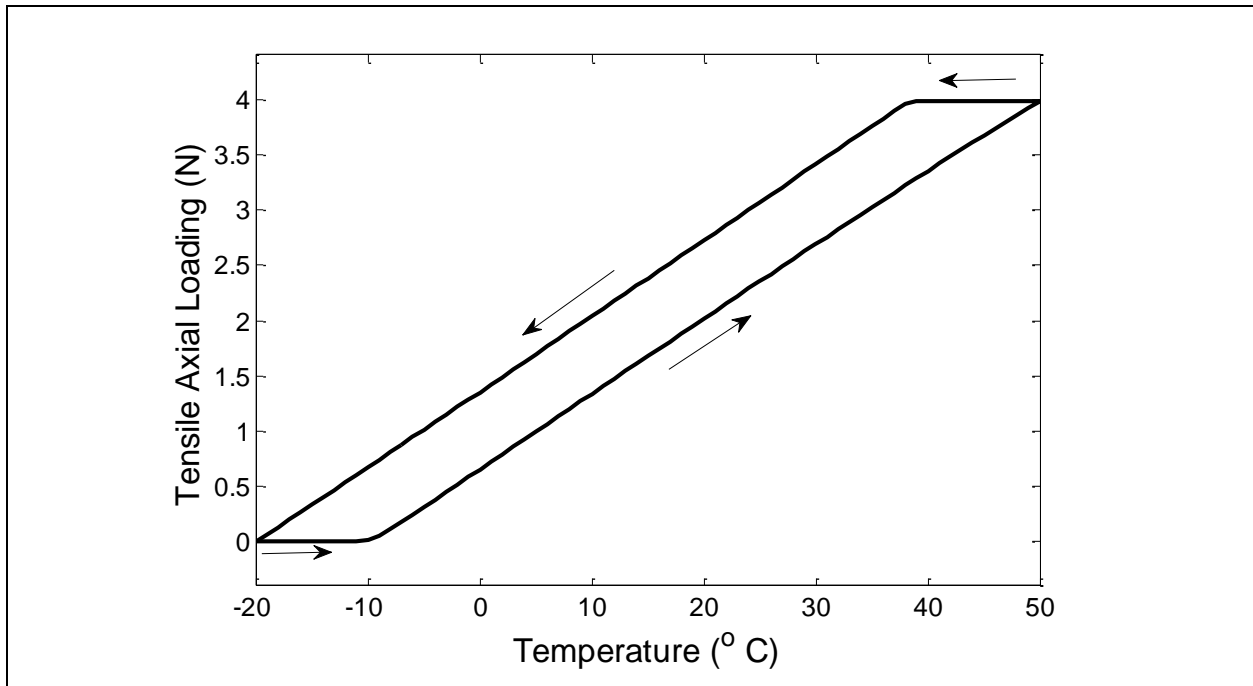


Figure 20. SMA induced load versus temperature

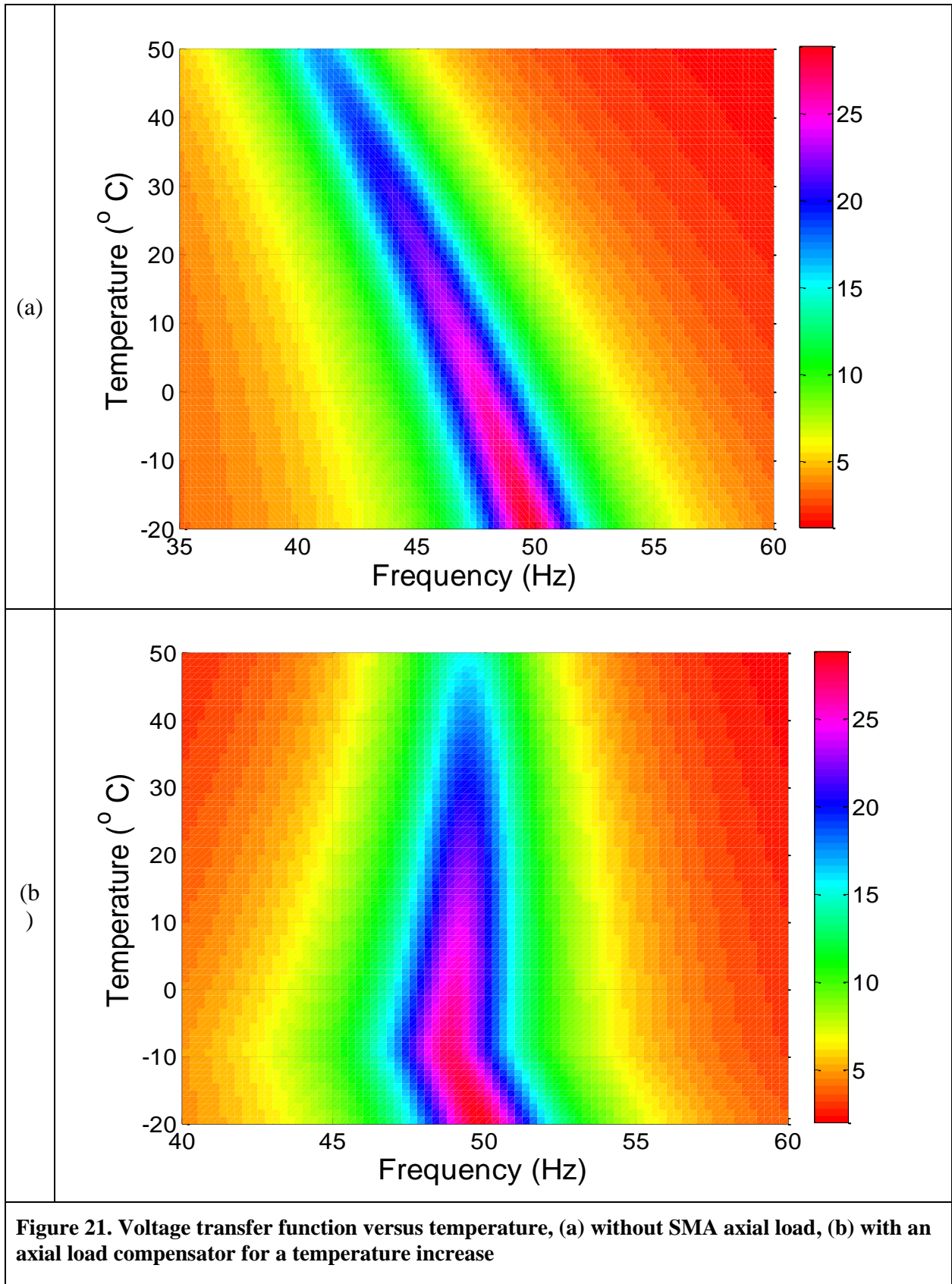


Figure 21 (cont'd)

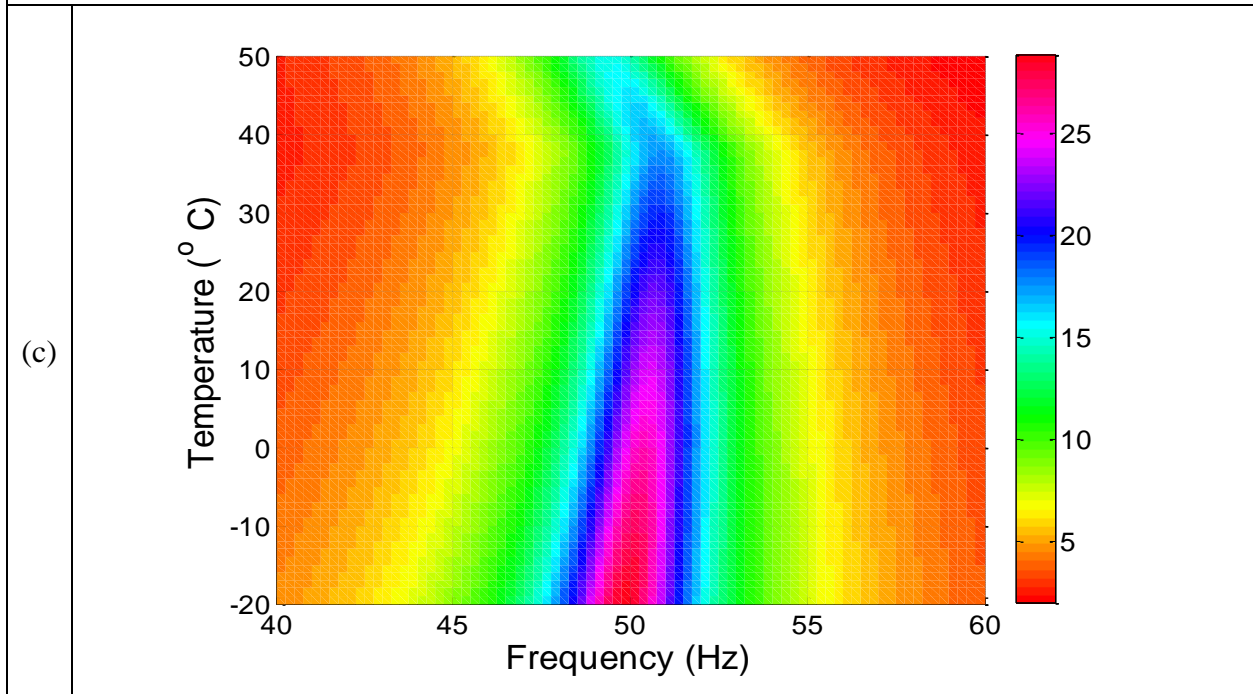


Figure 21(a) shows the voltage transfer function versus temperature for a system without SMA loading.

Figure 21(b) clearly shows the effect of an added SMA compensation mechanism, for a decreasing temperature in Figure 21(b) and for a temperature variation from low to high in Figure 21(c). It is noted that the compensation is not perfect due to the hysteresis behavior that the SMA exhibit. However, it is anticipated that by a better tailoring of the SMA material and the use of wires that have different properties, this effect can be reduced.

Figure 22 shows the variation of the resonant frequency of the harvester with and without the SMA induced axial loading effect. The arrows indicate the direction of the temperature variations. It is clearly observed that the temperature variation in the considered range pushes the resonant point up and down within a frequency range of about 10Hz for an uncorrected system.

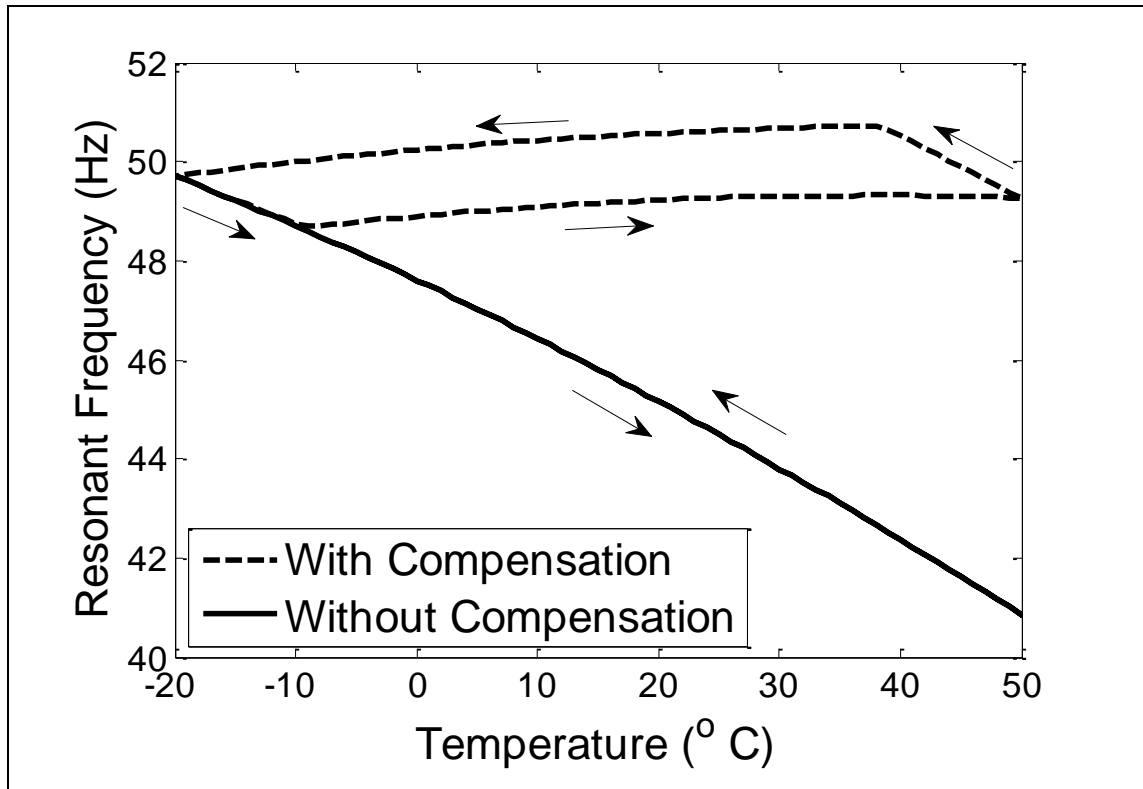


Figure 22. Variation of the resonant frequency with and without SMA induced load (arrows indicate the direction of temperature variations)

Such a huge variation naturally induces a high loss in the output of an energy harvesting module designed to operate in a predefined spectrum. The added correction mechanism restricts these oscillations within a narrow band of about 2 Hz. As mentioned, this band can be further reduced using optimized tailored SMA properties.

Simplified experiments were performed as a proof of concept for the described effects. Standard Nitinol extension springs from ‘Images SI, Inc’ were used. Only the tuning ability with temperature change is shown. An advanced materials matching was not performed. In the used configuration, the axial load is applied using two SMA springs connecting the tip of the beam to the base.

Experimental Results and Validation

The output voltage transfer function of the piezoelectric element was measured under a constant applied acceleration for different temperatures. At each temperature, the piezoelectric properties are extracted from the data shown in Figures 12 and 13, then incorporated into the response model (Equation 10) and used to evaluate the transfer function in the non-tuned configuration (at the initial preload reference point of 2 N compressive loading). The model output is compared to the measured results. The SMA springs are then attached to the setup. Using the manufacturer charts for the springs, the induced additional axial loading at a given temperature is evaluated.

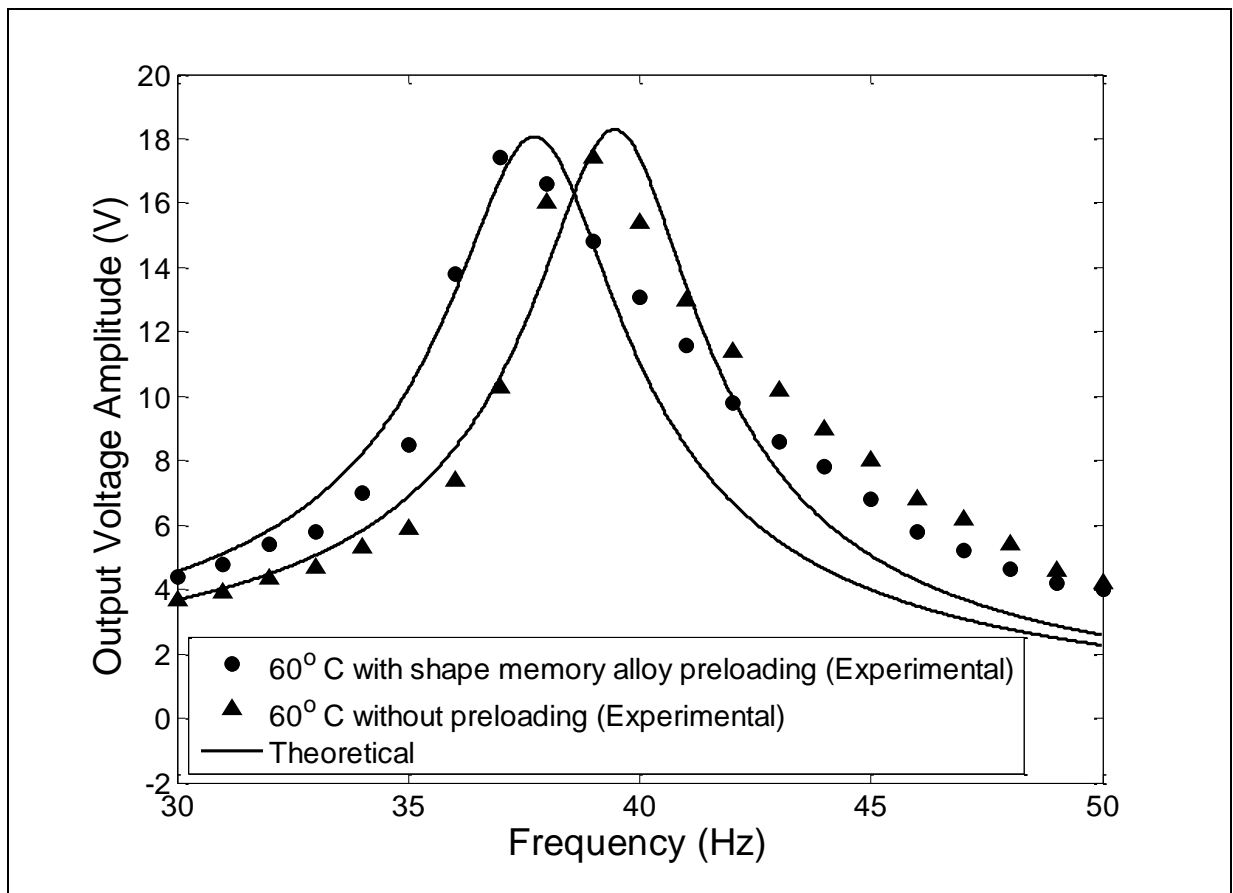


Figure 23. Output voltage transfer function of the transducer at 60 °C with and without SMA induced axial loading. $M_{tip}=3.75g$, Load resistance= $1M\Omega$.

The total loading value is injected into the model described into section 3 and the resulting voltage transfer function is compared to measurements obtained for the SMA-tuned configuration. Figure 23 shows the measured and the computed voltage transfer functions of the resonator at 60 °C with and without the shape memory alloy loading effect.

It can be clearly seen that the added SMA springs shift down the resonant frequency. Using the manufacturer chart of stiffness versus temperature for the SMA springs, it is determined that an added 0.7N loading shifted the resonant frequency from 39Hz to 37Hz. The preliminary experimental results prove that SMAs can be used to induce a variable axial loading dependent on temperature changes. This variation induces a change of the vibrator's stiffness, leading to an adjustable shift in the frequency response.

CONCLUSION

The presented study in this chapter showed that mechanical tuning of vibration energy harvesters through axial loading can be used to balance the effects induced by temperature variations. It was also shown that fully-passive temperature compensation, requiring zero input power for tuning, is feasible in piezoelectric energy harvesters. Experiments to evaluate the effect of temperature on the frequency response of a PZT-5H piezoelectric cantilever beam under base acceleration were first conducted. A generalized model for an axially loaded bimorph piezoelectric subject to temperature variations was presented. The model also describes the correction effect. Experimental results showing the combined axial load-temperature interactions were also shown.

The model was also extended to describe the overall behavior of a transducer mounted in a cantilever configuration and subject to axial preloading induced using temperature generated shape memory alloy deformations. Numerical simulations were conducted to evaluate the

variations of the SMA induced load with respect to ambient temperature. Preliminary optimizations, performed in these simulations, showed that the resonant frequency shifts in the piezoelectric system can be compensated. A test apparatus was built as a proof of concept prototype. Initial measurements compared the variations of the device's frequency response for an unloaded configuration and a SMA loaded system.

CHAPTER 4: PIEZOELECTRIC BASED SELF POWERED SENSOR FOR STRAIN MONITORING

INTRODUCTION

While the focus on piezoelectric energy harvesting from vibration was about increasing the level of harvestable power in order to achieve the usability of the CMOS floating gate sensors for vibration monitoring, piezoelectric energy harvesting from strain seems to provide enough energy to power the sensor (Lajnef et al. 2008). Piezoelectric harvester with properties in Table 1 can provide the minimum power requirement at a strain level of $25 \mu\epsilon$. The sensor is then capable of measuring and storing data using only the self-generated electrical energy harvested directly from the sensing signal using the piezoelectric patch. The work depicting a fully deployed strain sensing system with all the needed attributes is presented in this chapter. The calibration and installation of the sensor is addressed. The sensor output is defined and the evaluation of a full field data from a limited number of randomly distributed sensor is studied.

PIEZOELECTRIC FLOATING GATE SELF POWERED SENSOR

Sensor description

A CMOS floating gate is a poly-silicon gate surrounded by an insulator, which in standard semiconductor fabrication process is silicon-dioxide. The charge on the gate can be modified using hot electron injection or through tunneling. Injection in a pMOS transistor occurs primarily due to

hot-hole impact ionization caused by high electric fields at the edge of the drain-to-channel depletion region. As electrons are added to the floating gate its potential decreases, thus implementing a long term non-volatile memory. This low power operation makes it possible to have a self-powered sensor that can monitor mechanical loading through a piezoelectric harvester. In addition, a wireless communication capability was added to the sensor enabling the transmission and the reception of the data.

This module still needs further development to optimize its performance. Figure 24(a) shows the complete self-powered wireless strain sensor with attached antenna, and embedded into an epoxy packaging.

To ensure a good contact, most of the marketed packaged strain gages are “H-shaped”. Therefore, to ensure the most accurate strain measurements the sensor has been packaged in the same commercial "H-shaped" packaging, where the piezoelectric transducer is emerged at the core of the reinforced epoxy. It should be noted that there is a need for thermal protection for certain applications, such as pavement monitoring. For concrete monitoring, the thermal protection is not needed.

The envisioned monitoring system would consist of a network of low cost sensors distributed along the monitored structure. Each sensor node would be self-powered and capable of continuously monitoring and storing the dynamic strain levels. The data from all the sensors would be periodically uploaded wirelessly to a central database. The sensor will be read through standard radio-frequency (RF) transmission using a RF reader either manually operated or mounted on a moving vehicle.

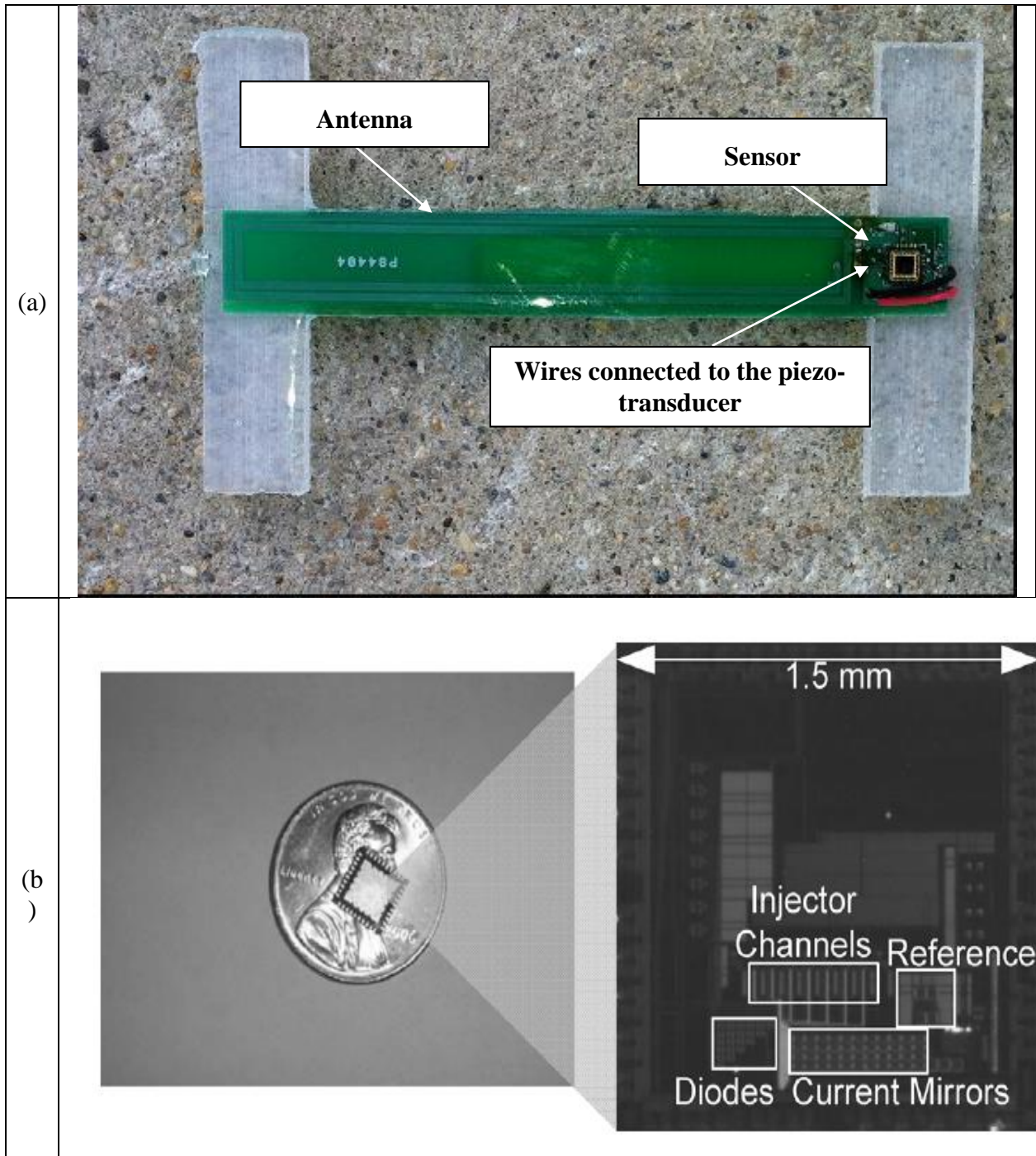


Figure 24. (a) Full sensor embedded in an epoxy package, (b) CMOS floating gate sensor.

Connected to the piezoelectric, the sensor is capable of continuously monitoring local strains within the host structure, implementing a level-crossing cumulative time counting as shown

in Figure 25. A series of memory cells (S_i) cumulatively store the duration of strain events, at a preselected level, experienced at the sensing node location.

The system measures the duration of events when the amplitude of the input signal coming from the piezo exceeds a specific threshold. For the used version of the sensor in this work, the piezoelectric transducer has to generate a voltage pulse with a minimum amplitude of 5.15 V to power the sensor. The minimum required voltage should be generated at a strain amplitude equal to the lowest fatigue (endurance) limit of the material, corresponding to the minimum strain amplitude that can lead to damage.

The upper voltage limit able to be measured by the sensor is 10 V. Since the output voltage of the piezo is linearly dependent to strain/vibration amplitude level, the measurable upper strain/vibration level is almost twice the minimum selected strain/vibration limit. Once the minimum level is selected depending on the strain range to be measured, the maximum level needed to be monitored will identify the number of sensor modules required. By stacking these modules, the covered strain spectrum can be extended depending on the specific application need. The number of modules is easily defined by the minimum natural number satisfying the equation below:

$$\frac{\varepsilon_{\max}}{\varepsilon_{\min}} \leq 2^n \quad (25)$$

where ε_{\max} and ε_{\min} are respectively the maximum and the minimum strain amplitude.

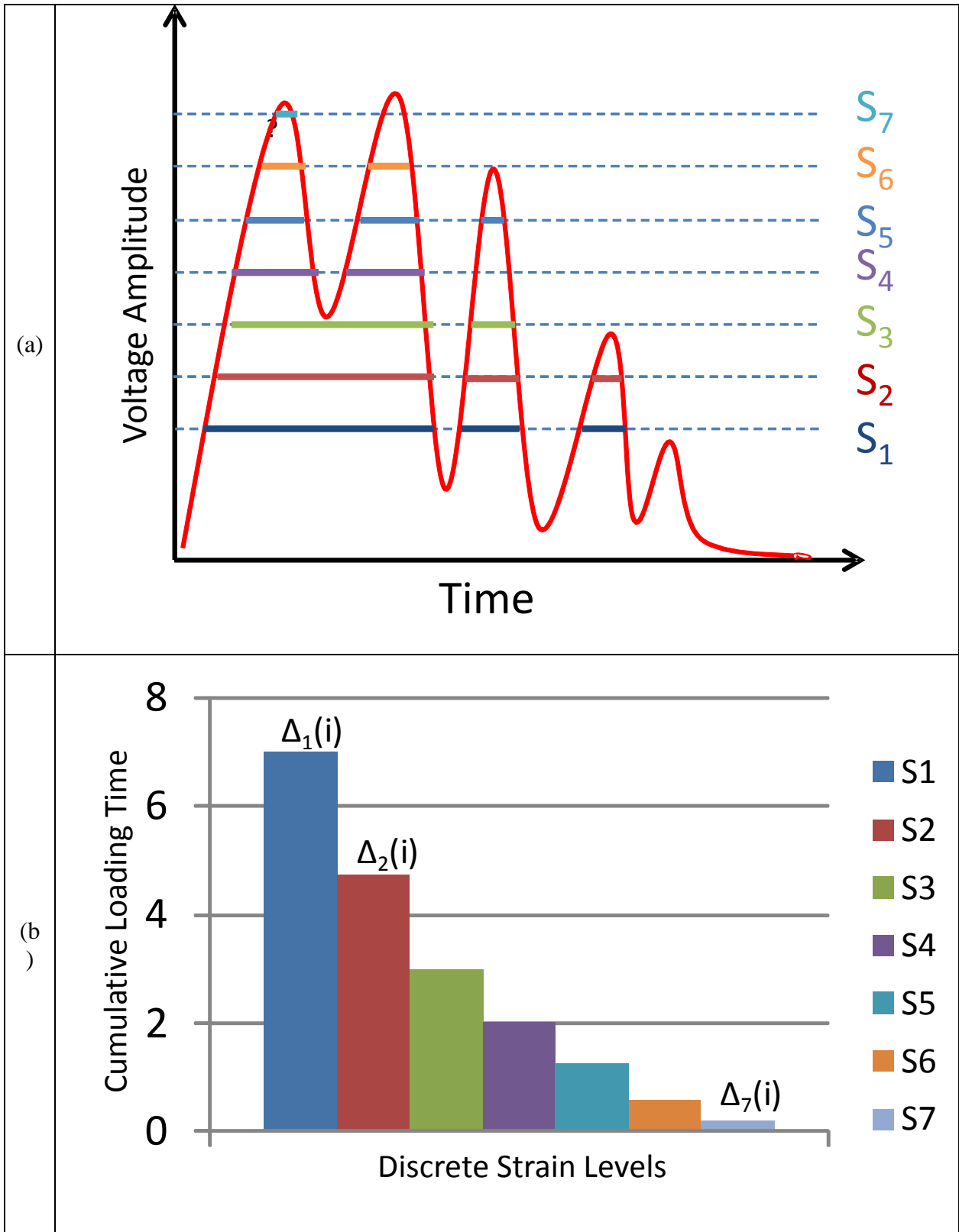


Figure 25. Illustration of the level crossing cumulative time counting implemented by the sensor

Sensor Output under Service Load

In order to select the best damage prediction model that fits the sensor output, the sensor output should be defined. The sensor measures the cumulative time of load experienced at the hosting node at preselected discrete levels.

The sensor output is then the summation of the cumulative loading time distributions: the cumulative distribution, and the cumulative loading time versus load (strain/vibration) level distribution. When monitoring vibration, the sensor-output is the cumulative vibration induced spectrum of the structure at the sensor node. When used for strain monitoring, it is the cumulative induced strain spectrum.

Service loads and the loading frequencies usually follow a Gaussian distribution. Since the summation of Gaussian distributions can be assumed by a Gaussian distribution, the sensor output can be defined by the cumulative function of a Gaussian distribution:

$$F(\varepsilon) = \frac{\alpha}{2} \left[1 - \operatorname{erf} \left(\frac{\varepsilon - \mu}{\sigma\sqrt{2}} \right) \right] \quad (26)$$

where μ is the mean of the strain distribution, σ is the standard deviation that account for the load and frequency variability, and α is the total cumulative time of the applied strain.

The sensor output data will be defined by the three parameters of Equation 26 obtained by fitting the function to the sensor output distribution collected from all of the memory cells.

SENSOR CALIBRATION AND INITIAL TESTING

Sensor Calibration

The system's configuration of the piezoelectric harvester subjected to axial strain loading is shown in Figure 26. The governing equations of strain sensor configuration are given by:

$$\begin{cases} Kr(t) - \Theta v(t) = \tilde{F}(t) \\ \Theta^T \dot{r}(t) + C_p \dot{v}(t) = \dot{q}(t) \end{cases} \quad (27)$$

where the stiffness matrix, the electromechanical coupling matrix and the capacitance matrix are defined in chapter two, equations (12) and (13).

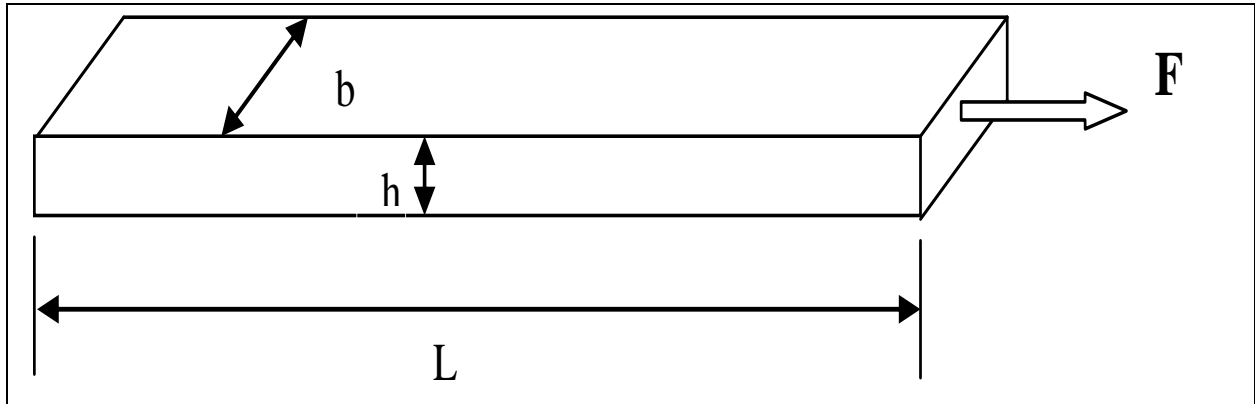


Figure 26. Schematic of a piezoelectric strain scavenger of length L , width b , and height h

\tilde{F} is the applied load induced by the axial strain expressed as following:

$$\tilde{F} = \underline{S} \underline{E} \quad (28)$$

where \underline{S} and \underline{E} are respectively the load strain and the elastic modulus of the piezoelectric $q(t)$ is the current output of the piezoelectric PZT element and can be directly related to the power output through a load resistance R .

Figure 27 shows the voltage transfer function of piezoelectric harvester having the properties given by table 1 subjected to 25 micro-strain across 50 mega-ohm resistance, equivalent to the sensor impedance. The ultimate strain limit, which is the minimum strain that causes material damage, should correspond to the minimum strain that causes the piezoelectric transducer to generate enough voltage. The minimum needed voltage for the sensor is estimated to be 5 volts. The dimensions of the piezoelectric generator is then the minimum width that generates 5 Volts across a 50 mega ohm load resistance subjected to the ultimate strain limit.

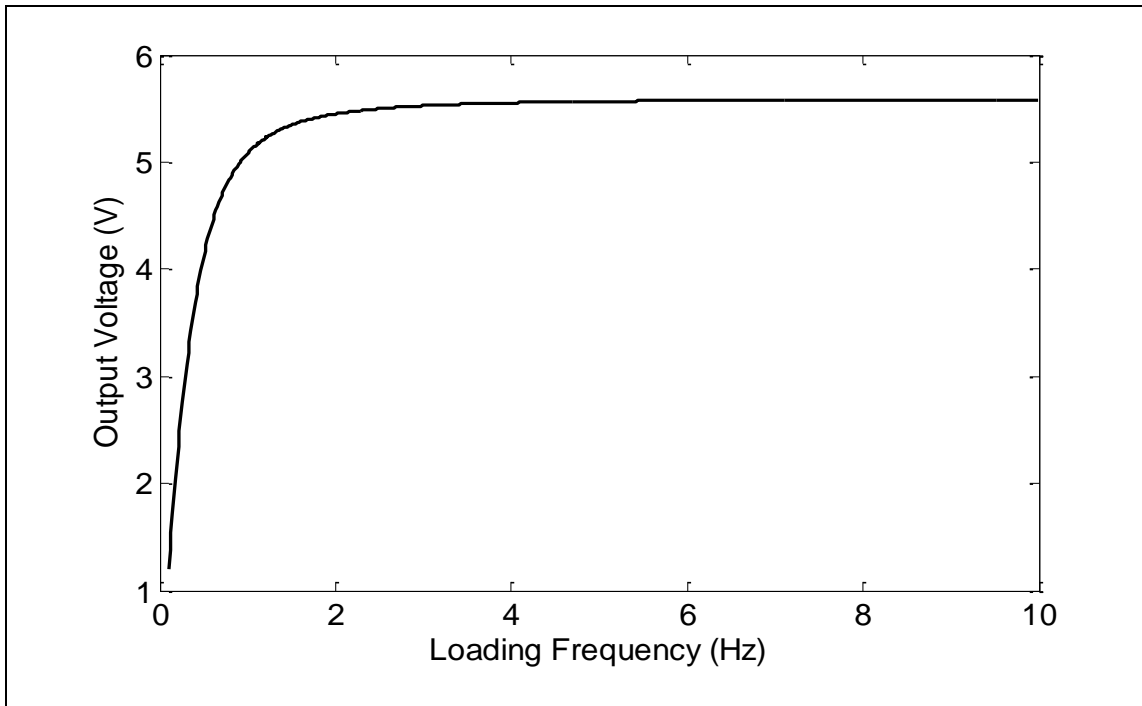


Figure 27. Voltage transfer function of a PZT piezo under 50 micro-strain loading across 50 mega-ohm load resistance

Experimental Setup and Initial Testing

A total of 2 mounted sensors were tested on concrete specimens (four point bending fixtures): two steel-reinforced specimens that had a span of 400 mm, a depth of 100 mm ($S/D=4$), and a width of 100 mm.

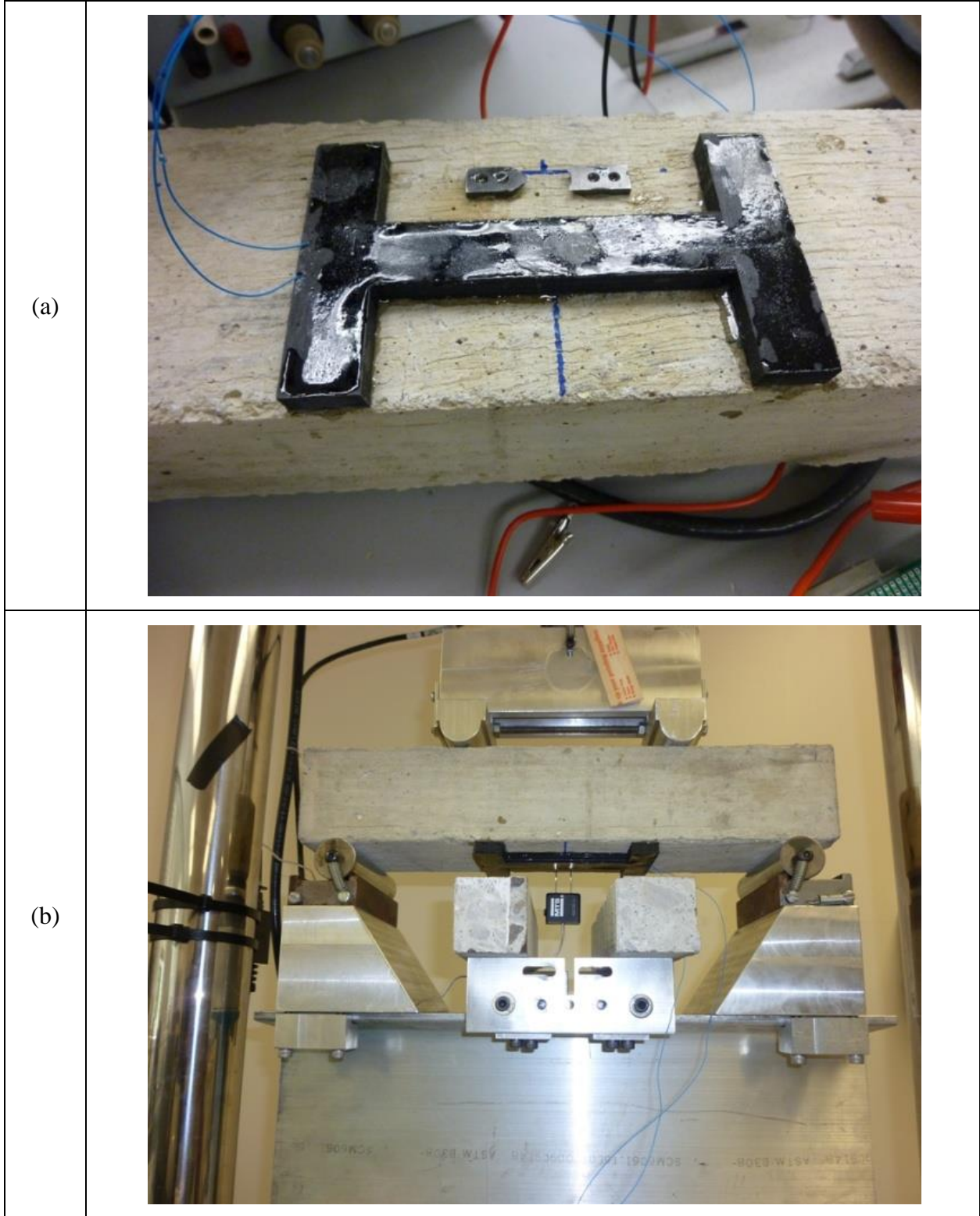


Figure 28. (a) Piezoelectric transducer embedded in epoxy then bounded to concrete, (b) Bending test setup to check the activation strain loss from a configuration to another.

A COD gage was also used to measure the strain and was attached to a pair of knife edges, which were mounted to the bottom face of the beam by a fast drying epoxy resin.

The COD gage is used to control strain and to check the validity of the measurement of the sensor. The width of the piezoelectric transducer is 5 mm, giving 5 volts under 200 micro-strain. Three sensors were calibrated and used (using Equation 23) to track a strain spectrum 200 to 1600 micro-strain.

The sensor was mounted at the bottom face of the beam (Figure 28(b)). Each specimen was subjected to a 5 Hz cyclical load; readings were taken every 10000 cycles. Figure 29 shows the measured cumulative loading distributions from the sensor at different stages of life of the steel reinforced beam.

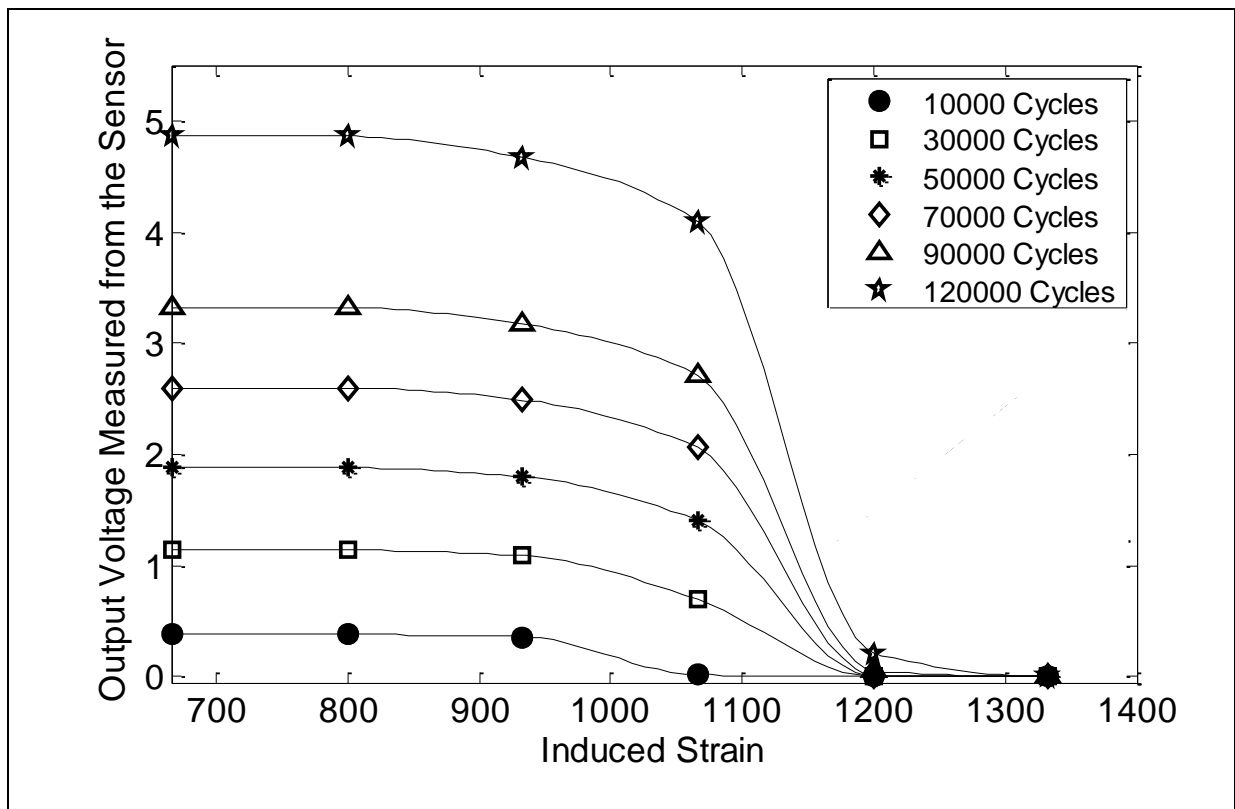


Figure 29. Cumulative distribution of strain duration expressed in term of voltage.

The results were compared to the COD gage measurements; error was very low, and results looked very promising. The prediction error will be discussed in more detail in chapter 5.

Initial Fatigue Testing

The sensor has been mounted and tested over the life span of other different concrete specimens (with the same dimension, but notched) with random (Gaussian) loading.

Figure 30 shows the strain distribution induced at the bottom of the concrete specimen. Figure 31 shows the cumulative strain distribution measured by the sensor at different life stage of the specimen. Then the measured output fitted using equation 26.

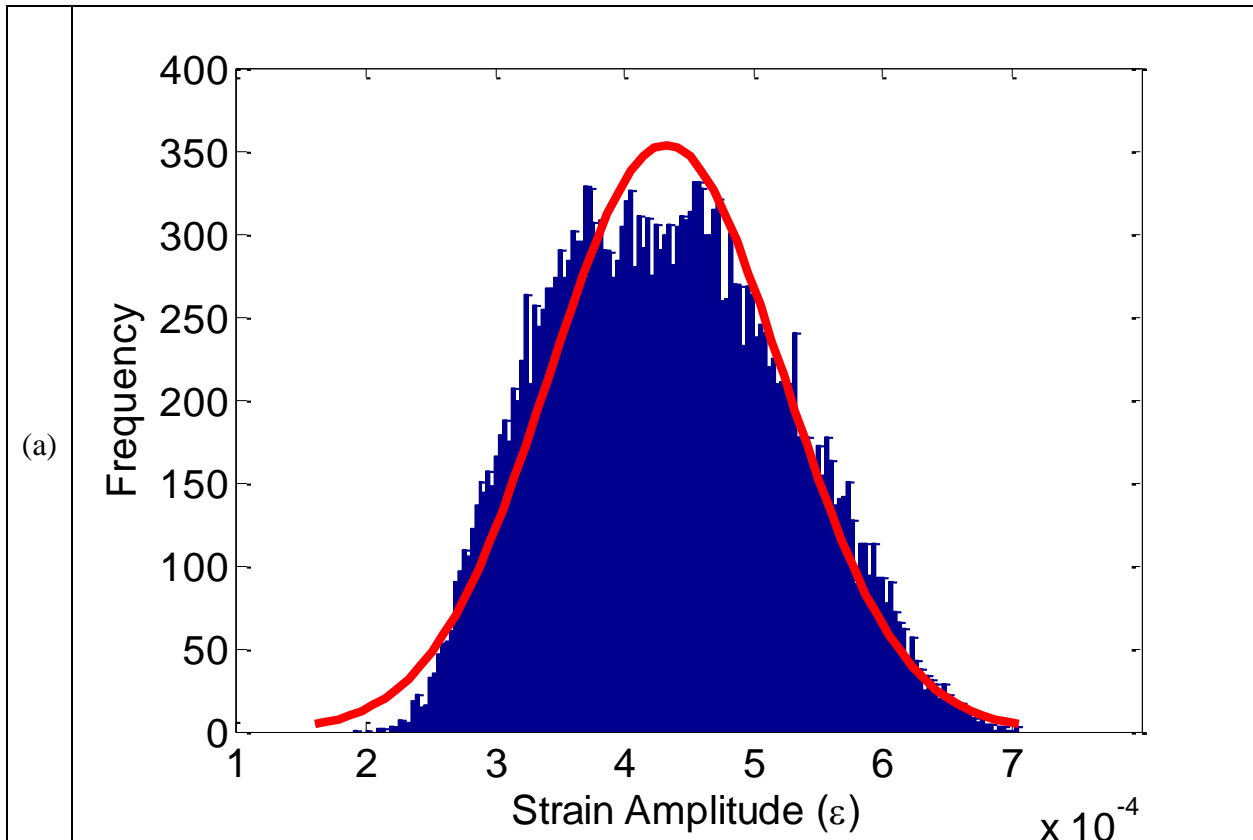


Figure 30. Strain distribution at different life stages: (a) at 25000 cycles, (b) at 40500 cycles.

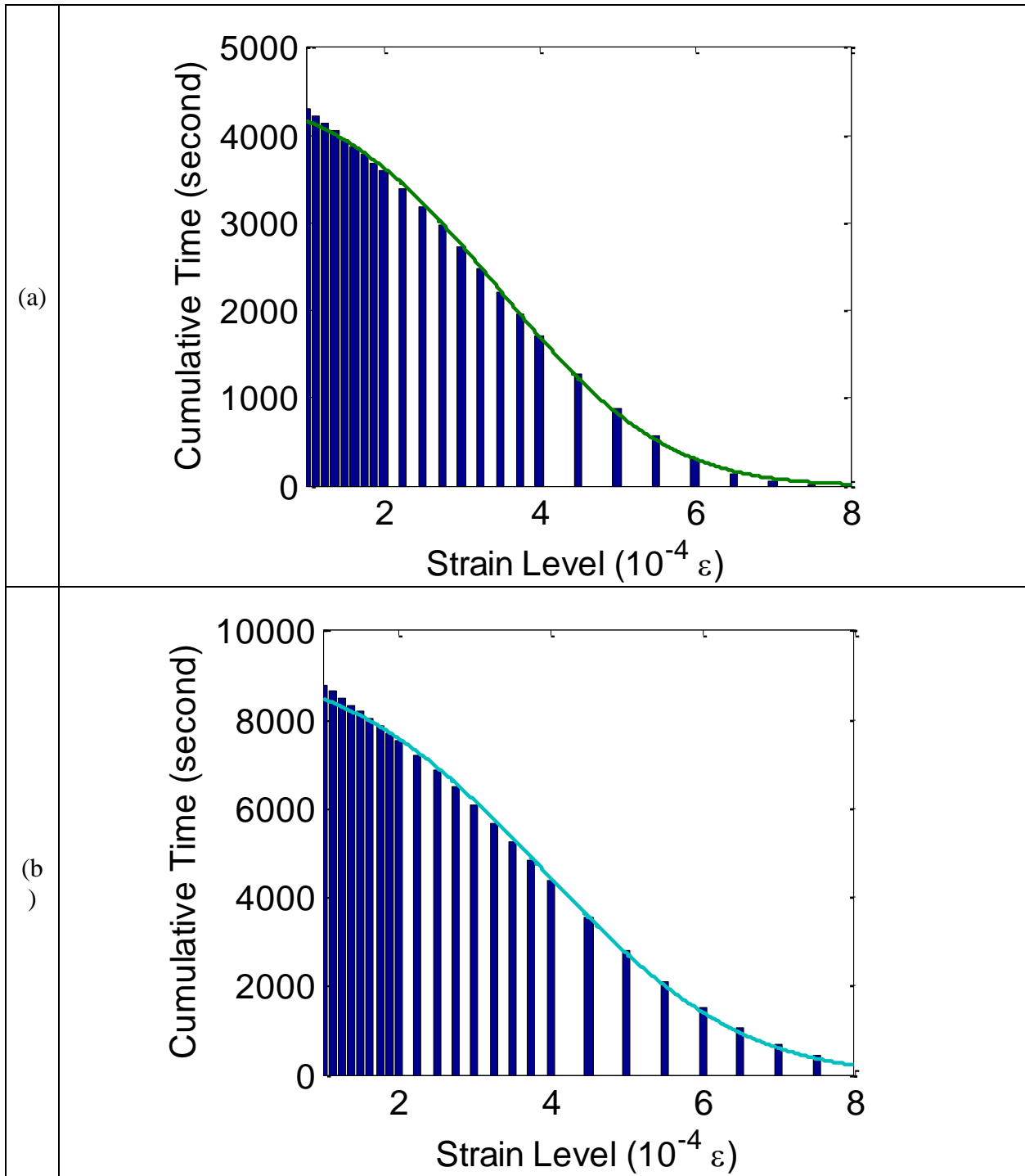


Figure 31. Fitting of the sensor's output at different life stages of the specimen: (a) at 25000 cycles, (c) at 40500 cycles.

The shift of the strain distribution over time is due to the loss of material stiffness caused by damage to the beam, which validates the output cumulative distributing measured by the sensor.

SENSOR NETWORK

Given that only a limited number of sensors can be deployed, it is critical to estimate the full-field measured strain distributions from a minimum number of sensors. The objective of this section is to study the prediction of full field sensor output data from a minimum number of equidistant sensors. Only the 1 D case has been considered. Its direct application is pavement monitoring, where the number of sensors installed to monitor strain are limited. The case of sensor network for pavement monitoring has been studied.

Probability Density Function of the Loading Distribution Parameters

The objective is to recreate the measured distribution induced by all the loading events at all locations using only a finite number of sensors implemented at determined node locations.

Figure 32 shows a pavement cross section with N sensors distributed along the section to monitor the longitudinal and transverse strain. The sensors are equidistant. The strain response of the pavement to traffic is the input to the sensors. The cumulative strain data induced by randomly generated truck traffic distributions were compressed into probability mass function histograms using the piezoelectric generator and the sensor models. Then the distribution parameters are evaluated (μ , σ and α).

The 3D response of a layered pavement system under a moving load with static and dynamic components has been modeled. The properties of the used layered system were obtained from Chabot et al. (2010). This three-layer system consists of a top viscoelastic layer modeled through the Huet–Sayegh model (Huet, 1963 and 1999; Sayegh, 1965), a road base (0.08 m in

thickness), and a sub-base layer (0.42 m in thickness) both assumed to be elastic and dependent on thermal and moisture characteristics. Detailed properties are given in Chabot et al. (2010) and Nilsson et al. (2002).

Traffic distributions were generated and applied as input loading to the pavement structure. Four different types of trucks were considered in the analysis: class 9, class 11, class 5, and class 16 (Chatti et al., 2009). One thousand passing truck events were simulated. Each event corresponds to a randomly selected truck type passing at a randomly selected position within the wheel path. The loading per axle as applied in this analysis was as follows: steering axle 68,500 N, single axle 80,070 N, tandem axle 71,170 N, and tridem and higher axles 57,830 N.

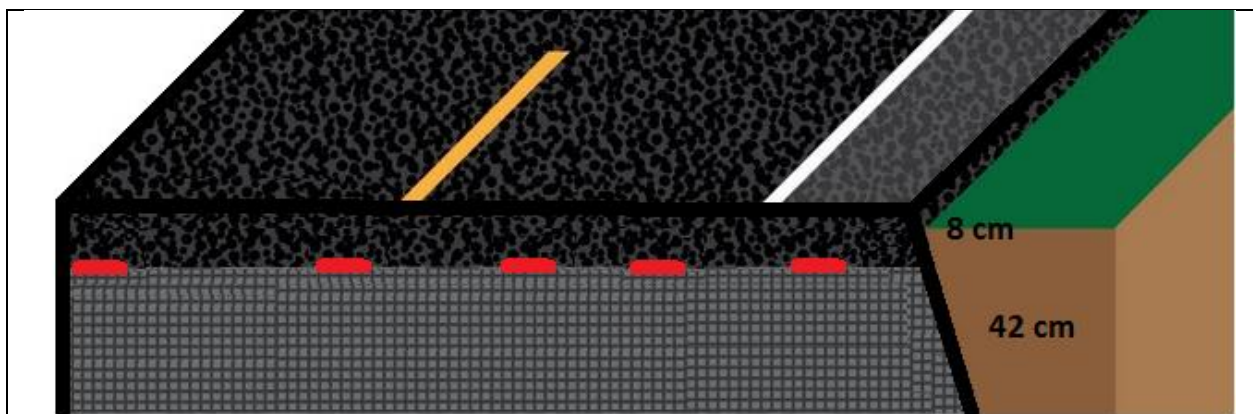


Figure 32. Pavement cross-section with sensors installed at the bottom of the HMA layer

If a model of a probability distribution " P_x " describing of the variation of the parameters of the distributions measured by the sensors along the transverse coordinate, all the missing values would be estimated.

Assuming that the transverse coordinate is a random variable and the parameters read from the sensors are the frequency of an observation of the transverse coordinate, then the variation of

each of the parameters α , μ and σ represents a probability density function of the "transverse coordinate".

The objective then would be to estimate the probability density functions described by each of the parameters. The log likelihood function of each probability density function can be written as:

$$\text{Log } L = \sum_i (\log P(y_i) + \log P(x_i | y_i)) \quad (29)$$

where y_i is all the possible transverse coordinates of the sensors, and $P(y_i)$ is its probability density. x_i is the observed data corresponding to the longitudinal coordinate of the sensor, and its probability density is defined by the normalized values of the parameters.

If the data is complete, the likelihood can easily be maximized. However, because the incompleteness of the data, there is a summation inside the log, which makes the optimization much harder. So in the case of missing values, the values are estimated based on the current probability parameters.

The probability distributions are assumed to follow a Gaussian mixture. The objective would be to evaluate the parameters of the mixture, namely the number of distribution in the mix, the means, and the standard deviations.

The most prominent method is known as Expectation Maximization. The data set is modeled with a fixed (to avoid over-fitting) number of Gaussian distributions that are initialized randomly and with parameters that are iteratively optimized.

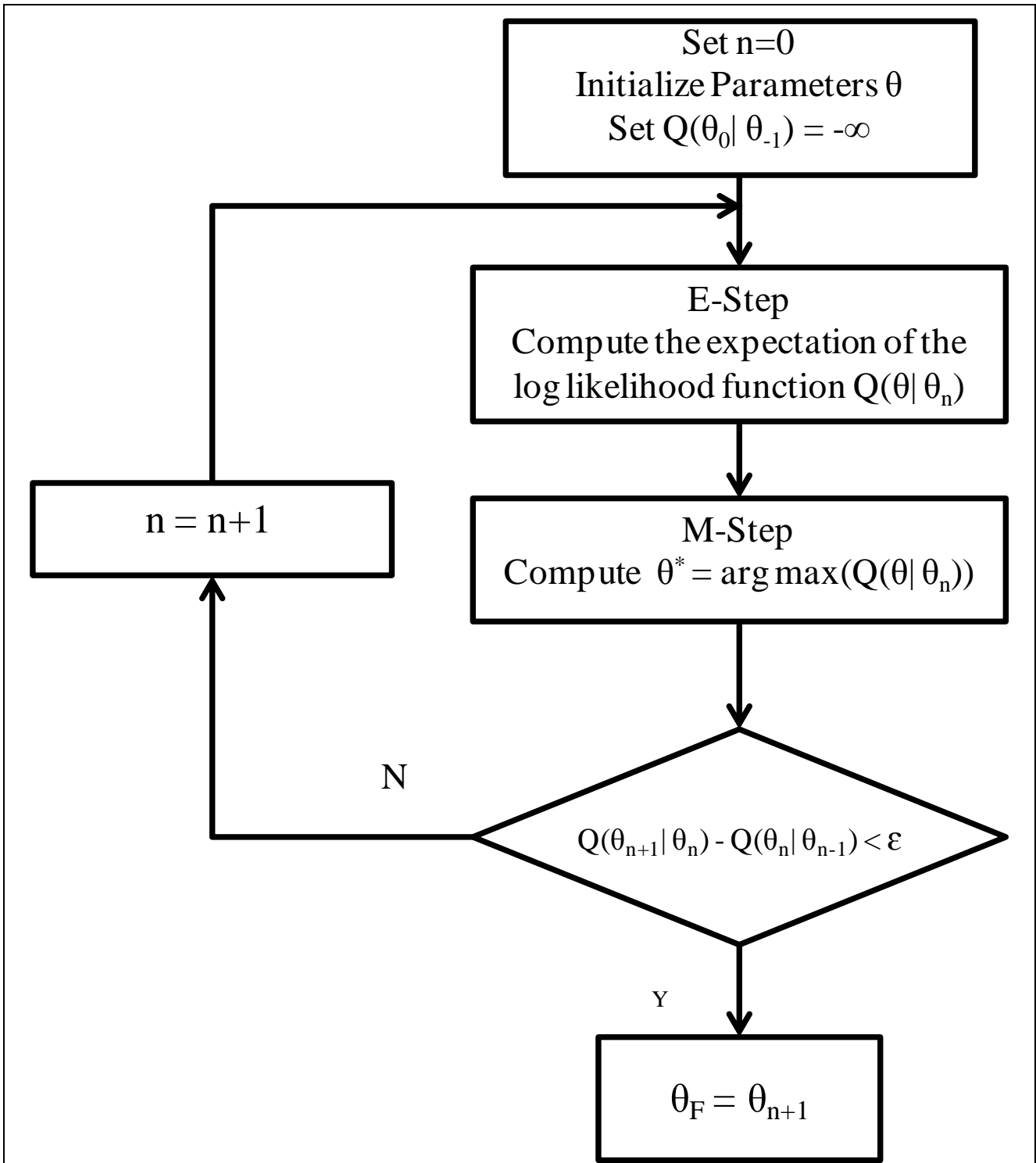


Figure 33. Schematics of the likelihood maximization algorithm

Figure 33 shows the schematic of the EM algorithm, and the missing values are filled based on the current parameters of the probability function (the parameters of the mixture) θ_n , and then

the new parameters are computed in the M step, which maximizes the likelihood of the completed data. If the relative error between two iterations is more than a given tolerance, continue running - otherwise the optimum parameters are reached.

Results and discussion

Figure 34 shows the estimated and theoretical probability density function of each of the parameters of the distributions read from the sensors. For pavement application, three components give the best description and the least error for the estimation of the density function of each of the parameters. Once the distribution is estimated, the output can be estimated at any point of the pavement cross section.

Using two Gaussian mixture components, the least square error of the full field estimation versus the number of sensors deployed in the pavement cross section has been computed and presented in Figure 35. Starting from 11 sensors, the error is almost the same, thus making 11 sensors enough to monitor the whole pavement cross section.

Results show that the parameters of a sensor's network output used for pavement monitoring can be described by a Gaussian mixture model making it possible to evaluate the full field cumulative strain measured in a hosting structure based on limited number of sensors. However, it should be noted that these observations are made for a linear elastic material behavior with no damage.

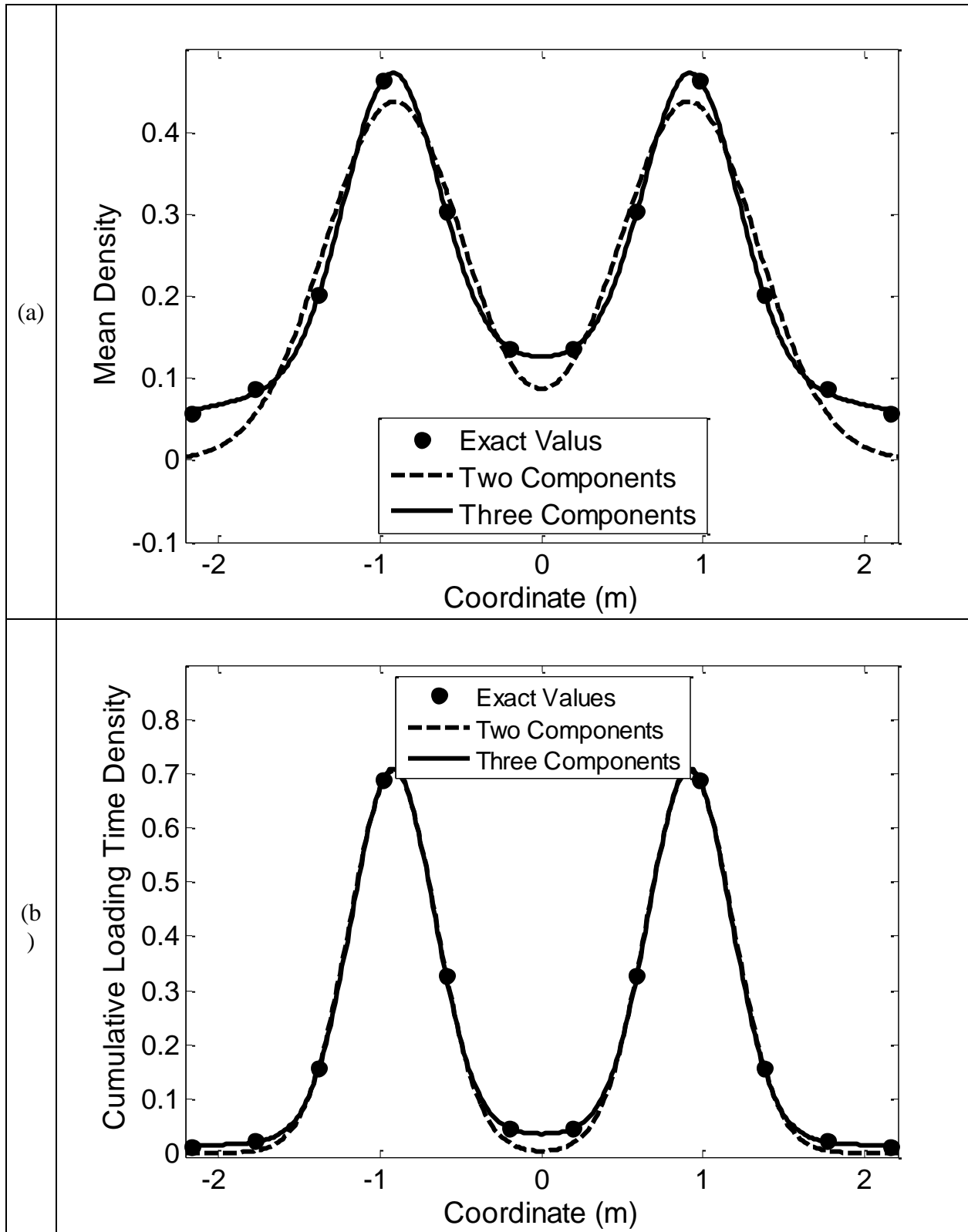


Figure 34. Theoretical and estimated density functions of the three parameters using the 10 sensors. (a) mean. (b) cumulative loading time

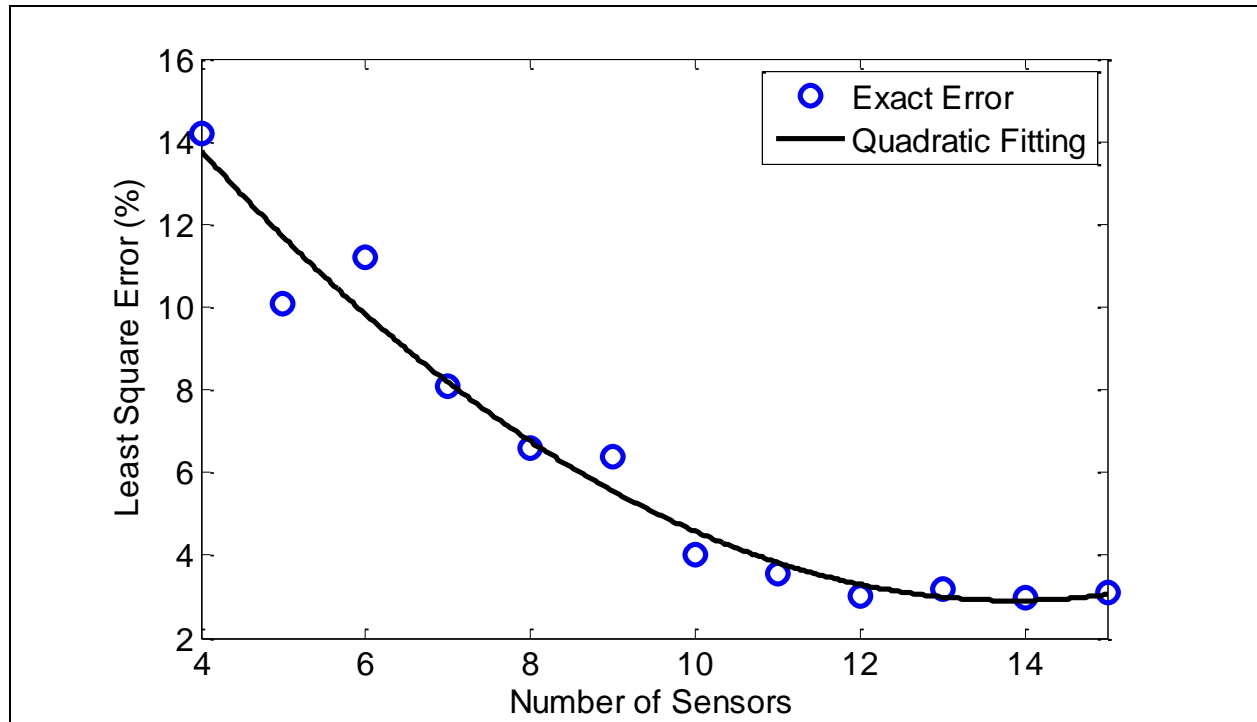


Figure 35. Least square estimation error of each of the parameters' distributions versus number of deployed sensors

CONCLUSION

In this chapter, the development and implementation of a piezoelectric self-powered sensor has been presented. Application of the sensor for concrete monitoring was developed and discussed. The feasibility of sensor network based on limited number has been addressed; however, the effects induced by the data compression format rendered by the sensor on the fatigue prediction capabilities of the system still need to be addressed.

CHAPTER 5: DAMAGE PREDICTION USING PIEZOELECTRIC SELF POWERED SENSOR

INTRODUCTION

One major obstacles facing health monitoring systems is the ability to accurately predict damage after structural state diagnosis. The objective of this chapter is to investigate the performance of the smart sensor and the usability of its output as a means to measure local damage and study remaining life prediction using a sensor node. First, the derivation of the damage index from the sensor's output data is detailed with results from a set of laboratory tests, comparing the damage index prediction between using the sensor output and the prediction using the complete time history data. Then, a projection of the remaining life of the tested specimens, using first a linear damage accumulation rule and then a survivability analysis, was computed and the accuracy was evaluated by completing the test until failure and counting the total real observed cycles.

DAMAGE INDEX DERIVATION

Damage, as defined in both damage and fracture mechanics, is the irreversible dissipation of strain energy caused by some external or internal applied force, ultimately manifesting into a loss of material stiffness (Schapery, 1990; Lemaitre, 1992). In one-dimension, damage can simply be defined by the degradation of the elastic modulus, E , as shown in equation (30).

$$D = \frac{E}{E_0} \quad (30)$$

D is the damage variable, defined from 1 to 0, and E and E₀ are the current and initial elastic modulus. Failure will occur at a value D_f which is a material property (Lemaitre, 1992). In fatigue, the loss of material stiffness (or Elastic Modulus, E) can be assessed using variations of the peak to peak strain data (Subramaniam et al., 2000). Under constant amplitude loading, the ratio between the modulus at any given time (E) and initial elastic modulus (E₀) is equal to the inverse of the ratio of the initial (Δε₀) and instantaneous (Δε) peak to peak strain levels. Thus, the damage variable D can be written in terms of Δε and Δε₀ as shown in equation (31).

$$D = \frac{\Delta \varepsilon_0}{\Delta \varepsilon} \quad (31)$$

The fitting parameters of the sensor output, the cumulative loading time, the mean and the standard deviation, can be written as a function of the parameters of the strain distributions:

$$\alpha = \sum_i^N \alpha_i \quad (32)$$

$$\mu = \sum_i^N \frac{\alpha_i}{\alpha} \mu_i \quad (33)$$

$$\sigma = \left(\sum_i^N \frac{\alpha_i}{\alpha} \sigma_i^2 \right)^{1/2} \quad (34)$$

where N correspond to the latest loading time period between the two last reading. Using equations (33) and (34), the mean and the standard deviation of the latest applied strain distribution at a time *t* can be evaluated from two consecutive readings, expressed by the following equations:

$$\mu_N = \frac{\Delta(\mu\alpha)}{\Delta\alpha} \quad (35)$$

$$\sigma_N = \left(\frac{\Delta(\sigma^2\alpha)}{\Delta\alpha} \right)^{1/2} \quad (36)$$

Once the mean and the standard deviation of the strain distributions are evaluated, using the Taylor series with exact derivation, the mean and the variance of the damage coefficient are derived, given by the two equations below:

$$E[D] = \frac{\mu_0}{\mu_N} \quad (37)$$

$$Var[D] = \frac{\sigma_0^2}{\mu_N^2} + \frac{\mu_0^2 \sigma_N^2}{\mu_N^4} \quad (38)$$

where the subscript 0 correspond to the first loading time period.

EXPERIMENTAL SETUP AND DAMAGE INDEX DISTRIBUTION

Experimental setup

To check the capabilities of the sensor for damage variable evaluation, twenty-three plain PCC three-point single edge notched beam specimens (TPB-SEN) were tested under constant and variable amplitude fatigue loading. Two beam sizes were considered: (1) The large specimens, which had a span of 400 mm, a depth of 100 mm (S/D=4), and a width of 100 mm and (2) The

small specimens, which had a span of 200 mm, a depth of 50 mm ($S/D=4$), and a width of 50 mm. The notch to depth ratio for each specimen was 0.35. A Crack Opening Displacement (COD) gage was used to measure the crack mouth opening and was attached to a pair of knife edges which were mounted to the bottom face of the beam by a fast drying epoxy resin, as recommended by RILEM (Shah, S.P., 1995). Each specimen was subjected to a 2 Hz cyclical load. Ten specimens were subjected to constant amplitude loading using a stress ratio (max load/peak load) of 0.85 (5) and 0.95 (5).

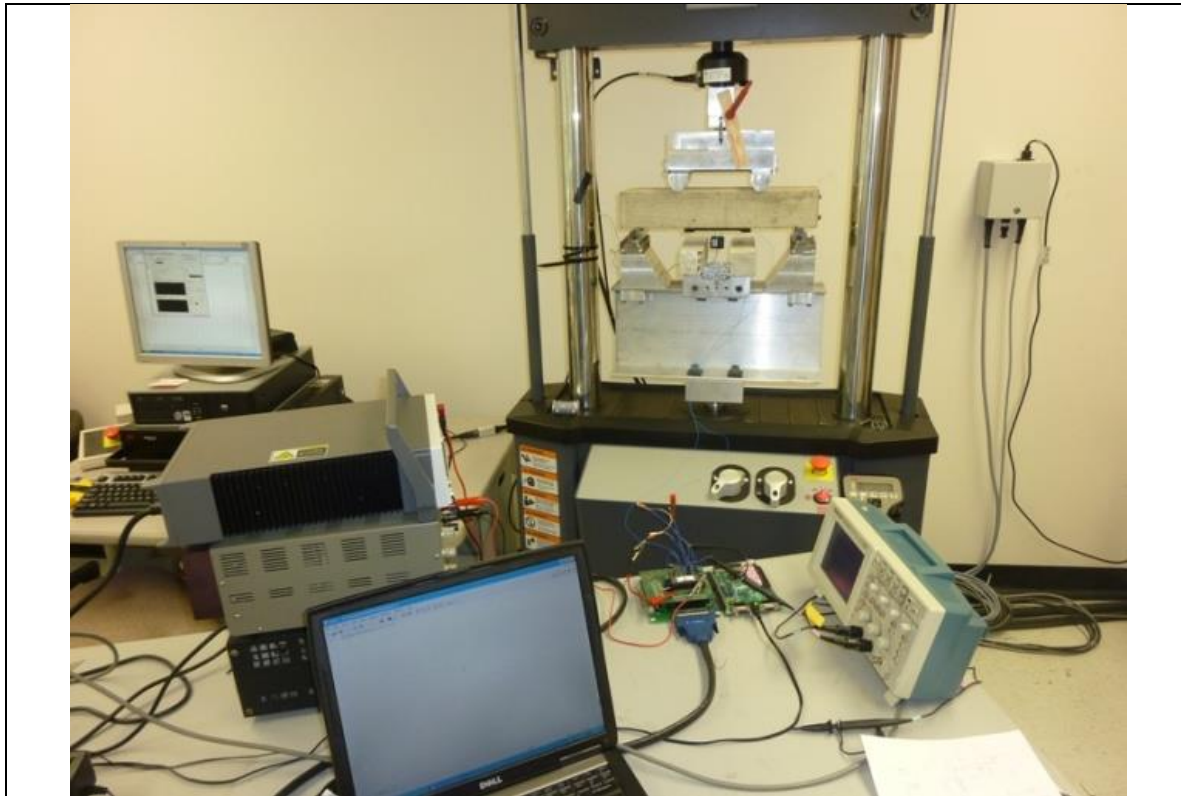


Figure 36. Test setup: the sensor is installed in the bottom of the concrete specimen to measure the induced tensile strain.

The other specimens were subjected to variable loading in which both the R ratio (min/max load) and the stress ratio were varied at several stages throughout the test. A reading was taken every 200 cycles.

The concrete mix used in this research consisted of ASTM C-150 Type I cement, natural sand, and limestone coarse aggregate (nominal maximum size of 25 mm). The water to cement ratio was 0.45 and the air content was 6.5%. The unit weight was 2274.62 kg/m³. The average 28 day Modulus of Rupture (MOR) and the split tensile strength, f_t , were 5.23 and 2.89 MPa, respectively. The 28 day compressive strength was 25 MPa. The specimens were cured for one year inside of a humidity room and then placed in ambient temperature for one more month to ensure minimal strength gain during fatigue testing.

Damage index distribution

Figure 37 shows the variation of the damage index distribution over the entire life span of a concrete specimen. It shows that the mean damage index is decreasing over time. The standard deviation of the index is, on the other hand, nearly constant over the life of the specimens.

The prediction's relative error of the damage index mean is relatively low (Figure 38); less than 20%. The prediction error is taken into account by the standard deviation.

At the initial stage of the beam, there is a fast change of the induced strain amplitude, causing a fast variation of the damage index and a higher standard deviation.

Besides the prediction error, the standard deviation takes into account all the missed information that the sensor can't sense, such as the load distribution, the induced strain sequence, and the loading frequency.

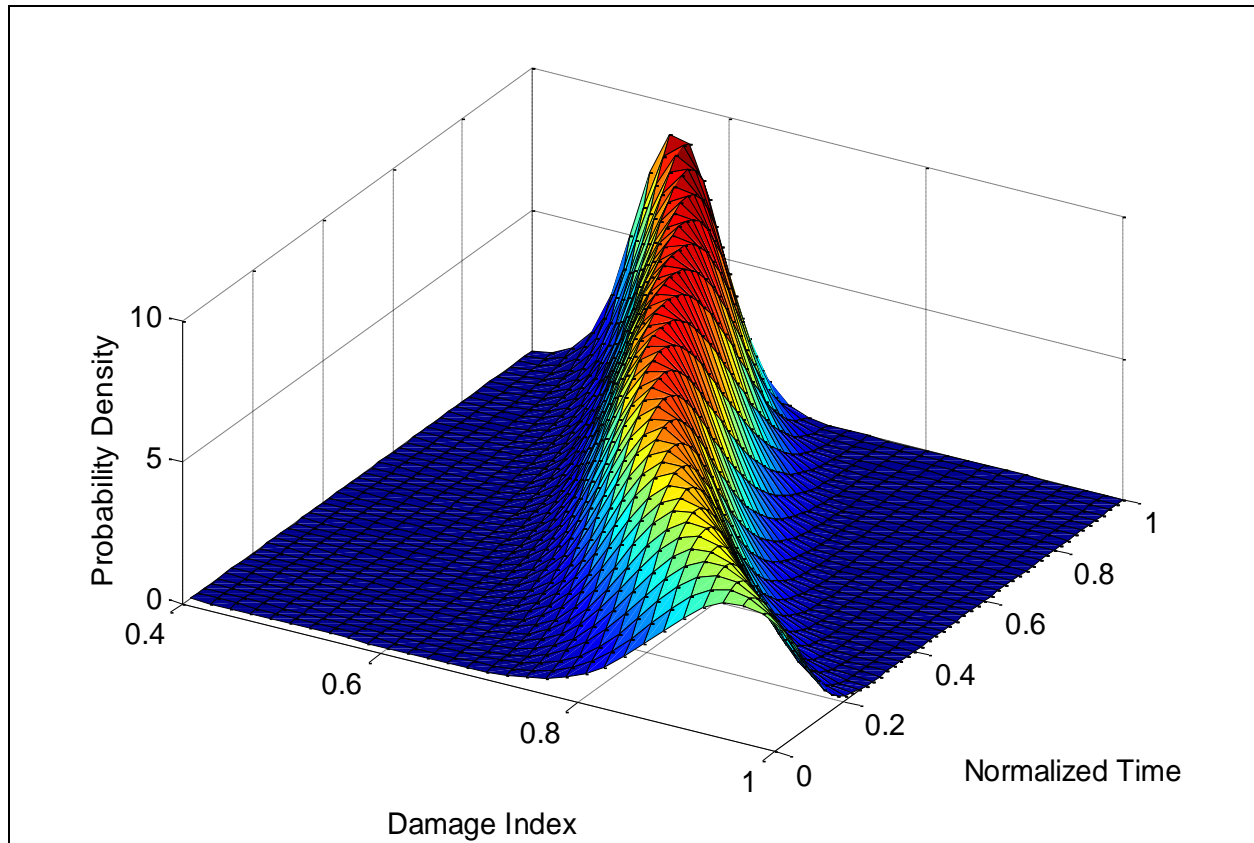


Figure 37. Probability distribution of the damage coefficient versus the number of cycles of loading

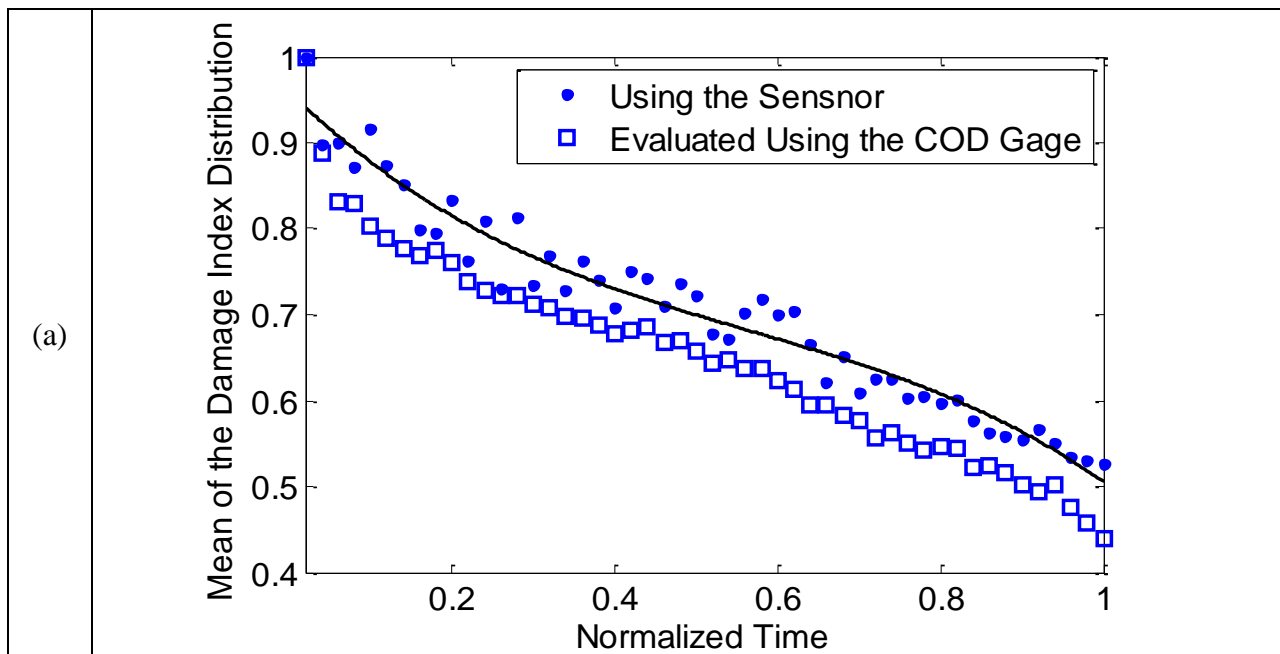


Figure 38. (a) Variation over time of the mean of the damage index versus the exact damage index evaluated with the COD gage, (b) Variation of the variance of the damage index distribution.

REMAINING LIFE PREDICTION

Linear Damage Accumulation

Equation 39 and 40 show the linear damage accumulation rule that is used in the MEPDG and adopted in this work in order to predict the remaining life of the concrete specimens. The coefficients β_i , in equation 40 were calibrated for every specimen using the sensor reading. Subramaniam et al. (2000) observed that under constant amplitude loading, the inflection point between the deceleration and the acceleration cracking region occurs at approximately 40 to 50% of the total life of the specimen. Thus, the coefficients pertaining to the first half of the specimen's life should be similar to the second half. Once the coefficients are known, a remaining life prediction can be made.

$$D = \sum \frac{1}{N_f} \quad (39)$$

$$\text{Log}(N_f) = \beta_0 \left(\frac{1}{SR} \right)^{\beta_1} + \beta_2 \quad (40)$$

For every specimen using the sensor's output, the linear damage accumulation equation function is fitted and the coefficient β_i are evaluated, then used to predict the remaining life of the specimen. The fitting parameters usually converge (stabilize) when the inflection point of the damage index is reached.

Table 4 shows the predicted remaining life using the described method based on the sensor output and the calibrated coefficient for different tested specimens. The loading of the specimens was stopped, and the remaining life was estimated and compared to a standard calibrated equations estimation. The tests were then continued until failure in order to record the actual remaining life.

As observed in the results for the considered cases, the predictions evaluated using the localized sensor data are closer to reality than the standard calibrated equation predictions.

Table 4. Predicted remaining life using calibrated coefficient and the sensor output.

| Exact remaining life | Predicted remaining life using standard equation | Relative error (%) | Predicted remaining life using the sensor | Relative error (%) |
|----------------------|--|--------------------|---|--------------------|
| 391 | 709 | 81.3299 | 325 | 16.8798 |
| 20527 | 716 | 96.51191 | 5873 | 71.3889 |
| 420 | 835 | 98.8095 | 425 | 1.19048 |
| 9350 | 902 | 90.35294 | 7125 | 23.79679 |
| 7022 | 922 | 86.86984 | 11048 | 57.3341 |
| 10980 | 990 | 90.98361 | 23011 | 109.572 |

The standard calibrated equation does not differentiate between the specimen's specific properties; the predicted values are almost constant. However, the predictions of the calibrated equation using the sensor's output are more accurate since the sensor's output is very specific to each specimen.

It should be noted that the damage index at failure is considered a random variable that depends on the material properties. However when installed, the only information that the sensor provides is the cumulative strain distribution and the damage index distribution, which gives no information about the index at failure.

Survivability analysis

Since the damage index at failure is a random variable that depends only on the material properties, the prediction of the remaining life by assuming it as a constant will not improve the prediction. The idea is to use the sensors output to construct a probability density function of the damage index at failure in order to improve the prediction over time.

Probability density function of the damage index at failure

Reliability engineering and survival analysis mostly deal with a positive random variable called “lifetime”. The lifetime is manifested by a failure or other “end event

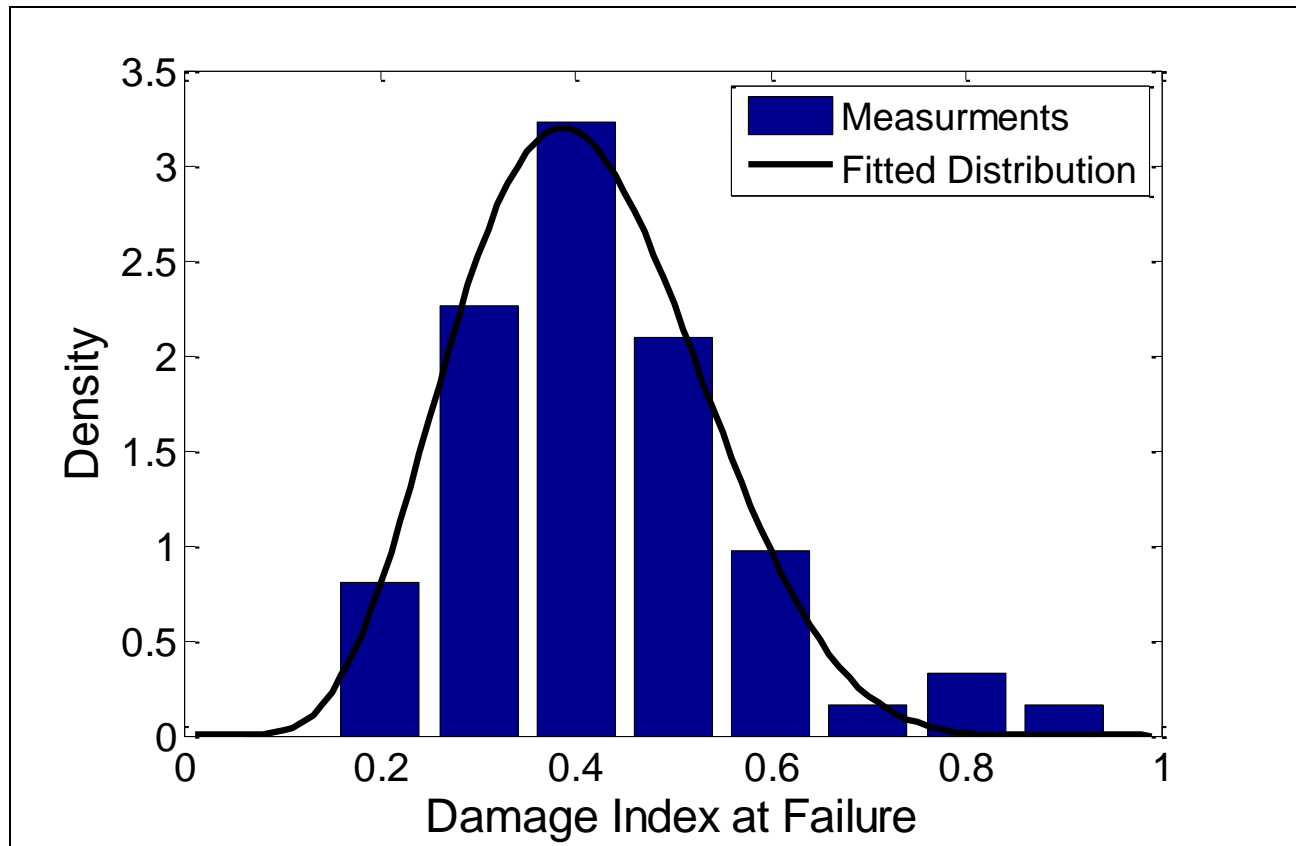


Figure 39. Probability density function of the damage index at failure

”. In this particular case, the failure is defined by the total break of the beam, and the lifetime variable is the time T , at which the failure occurs with a cumulative distribution function

$F(T)$, which here is defined by the probability of the damage index at time T being higher than the damage index at failure:

$$F(D(T)) = P_r(D_f < D(T)) \quad (41)$$

Figure 40 shows the density function of the damage coefficient at failure. A total of 23 specimens have been tested and the index has been measured using the COD gage. The fitted distribution is a logit-normal.

The objective is to evaluate the survival probability function of the specimen based on the evaluated damage index using the sensor and the probability density function of the index at failure.

Survivability function

The remaining lifetime cumulative density function is defined using the law of conditional probability, the condition that the beam didn't fail at time $t = x$:

$$F_x(t) = \frac{P_r(x < T < x + t)}{P_r(x < T)} = \frac{F(x + t) - F(x)}{1 - F(x)} \quad (42)$$

The corresponding survival probability function of the beam is given by:

$$\bar{F}_x(t) = \frac{1 - F(x + t)}{1 - F(x)} = \frac{\bar{F}(x + t)}{\bar{F}(x)} \quad (43)$$

The remaining life at a time T is estimated to be the expectation of the survival probability function:

$$Rem = E(T) = \frac{\int_T^{\infty} \bar{F}(x(t)) dt}{\bar{F}(x(T))} \quad (44)$$

However, the lifetime probability function is not defined; the remaining lifetime should be expressed as function of the damage index probability function, as it is the only information that the sensor can provide. Using a change of variable, equation 42 can be expressed as a function of the damage index:

$$Rem = E(T) = \frac{\int_{D(T)}^{\infty} \frac{\bar{F}(D)}{\frac{dD}{dt}(T)} dD}{\bar{F}(D(T))} \quad (45)$$

where $\frac{dD}{dt}$ is the variation of the damage index with respect to time, evaluated by fitting a shape function to the damage index variations values evaluated using the sensor at different life stage of the specimen.

Results

The assumed shape functions are linear and arcsine. Figure 41 shows the normalized predicted remaining life (41) using the described method. The specimen lifetime is normalized, as well as the prediction remaining life. The normalized lifetime goes from zero to one, one meaning failure; however, the predicted remaining life goes from 1 to 0, where 0 remaining life also means failure.

As the specimen approaches failure, the more fitting points are available, and the more accurate the prediction is. It should be noted that the fitting stabilizes when the inflection point of the damage index variation is reached.

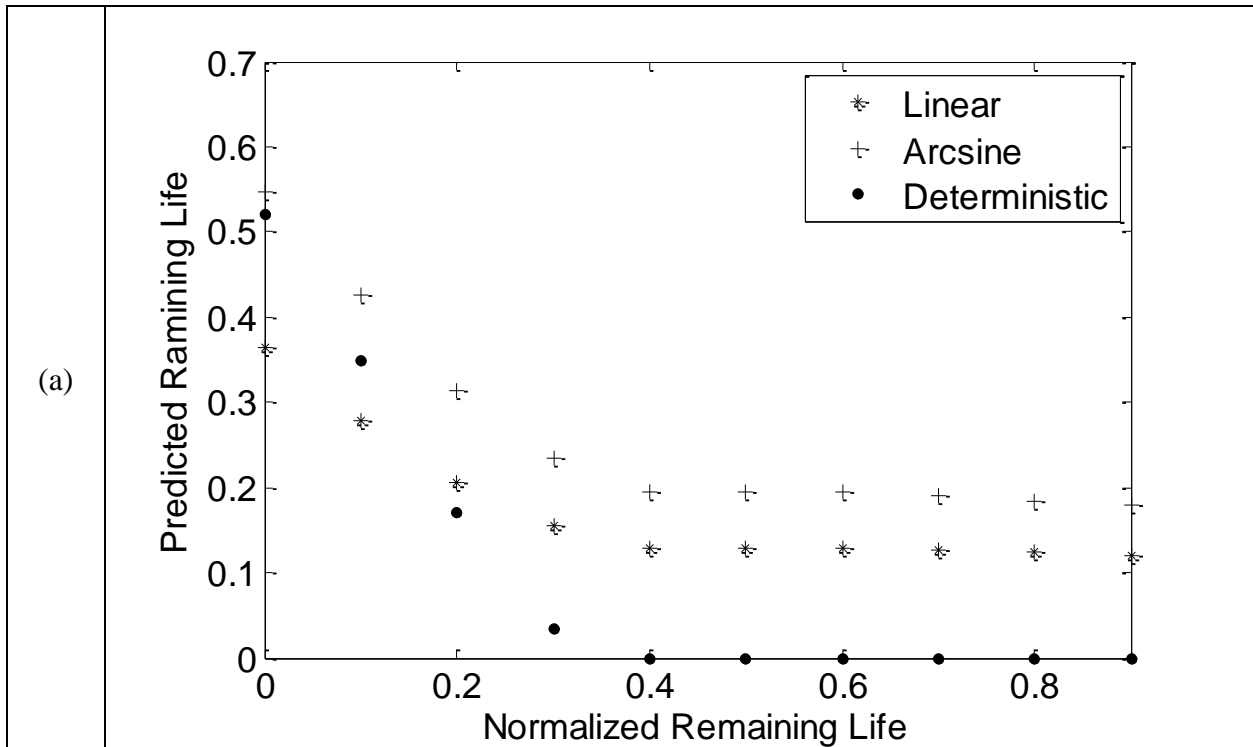


Figure 40. Normalized estimated remaining life vs. normalized specimen's lifetime using three different methods, (a) first specimen (b) second specimen.

As shown in figure (40), the prediction using the survivability function is not always better than the linear accumulation rule function. Two cases should be noticed: if the damage index at failure is a higher value (higher than the mean of the distribution or at least close) then the survivability method gives better results. Otherwise the accuracy of the results is similar. Besides having the advantage of long-term capabilities that help give better remaining life prediction using the linear accumulation damage rule, the sensor also gives the advantage of using a survivability analysis that helps the predictions accuracy by providing a data base of the damage index at failure.

The probability of the remaining lifetime is a good indicator of how reliable the prediction is. As shown in Table 5, starting from a probability of 0.6, the relative error of the predicted remaining life is less than 50%. When installed in the real field, by evaluating the lifetime

probability it is able to decide how reliable the predictions are. Tables 5 compares the predictions using a survivability analysis and the prediction using a linear damage accumulation rule.

The predictions using survivability analysis are more accurate simply because the material properties have been considered by taking into account the probabilistic nature of the damage index.

The probabilistic method is a powerful tool to deal with lack of information in order to predict the remaining life of structures. When the sensor is in the field, this method has many advantages over the linear damage accumulation method: it does not require any estimation of the material properties. For example, the resilient modulus for concrete, and it is very convenient with the sensor functionality, with two successive readings the estimated remaining life of the hosting structure can be estimated. This method is more realistic since it covers the lack of data and information about the structure such as the load distributions and the loading frequencies.

Table 5. Estimated remaining life using the different fitting shape function

| Exact Remaining Life (RL) | Linear Shape Function | | | Arcsine Shape Function | | | Linear damage accumulation | |
|---------------------------|-----------------------|--------|-----|------------------------|-----------|-----------|----------------------------|-----------|
| | RL | Prob | RL | Prob | Error (%) | Error (%) | RL | Error (%) |
| 0.5 | 0.3881 | 0.5988 | 22 | 0.6959 | 13.71 | 14 | 0.73 | 46 |
| 0.4 | 0.3481 | 0.6436 | 12 | 0.717 | 5.04 | 5 | 0.51 | 27 |
| 0.3 | 0.3115 | 0.6784 | 3 | 0.735 | 3.68 | 4 | 0.48 | 60 |
| 0.2 | 0.2836 | 0.7218 | 41 | 0.7575 | 12.87 | 13 | 0.40 | 100 |
| 0.1 | 0.2525 | 0.757 | 152 | 0.7748 | 21.71 | 22 | 0.40 | 300 |

CONCLUSION

The presented study in this chapter showed that remaining life of structures can be predicted with a better accuracy using a long-term monitoring self-powered sensor. A model for damage index derivation from cumulative load distribution was presented. The model takes into account the missing data. It was tested on concrete samples, and the damage index evaluation results looked very prominent.

It was also shown that probabilistic method is more practical and reasonable to use in the field, as it is a powerful tool to deal with a lack of information and can predict the remaining life of structures. It doesn't require any estimation of the material properties and the remaining life of the structure can be estimated at any time of its lifetime.

CHAPTER 6: CONCLUSION AND RECOMMENDATIONS

Over the last four decades, a significant interest has been placed on research related to damage prediction for the purpose of structural health monitoring. In order to improve the predictive capabilities of these methods, new emerging sensing technologies, more adapted to the SHM issues, are being developed. These systems are able to better measure and identify the parameters relevant to the health state of the structure. Global methods are the most commonly used structural health monitoring techniques. Measurement of the acceleration response of structure is the most relevant information needed in order to use these methods. However, it has been shown that methods are very sensitive to environmental changes (moisture content, temperature variation, etc). In addition, the large scatter in material data, i.e., fatigue, combined with limitations on the number of sensors that can be deployed, have hindered the development and validation of improved prediction models.

The work aiming at developing a fully deployed piezo-based self-powered SHM sensor has been presented in this thesis. The new type of data generated by the sensors, presented the challenge of developing and validating new adapted models for local and global damage prediction. The sensing system consist of a self-powered computation and non-volatile storage: it uses the physics of floating gate transistor injection principles to compute cumulative voltage output of a piezoelectric generator at preselected discrete levels. The wireless operating of the sensor allows also for longer lifetimes compared to conventional strain gauges since there is no

risk of wire damage. In addition, extensive sensor networks could be deployed for structural monitoring.

The major problem toward achieving long term self-powered monitoring was providing power. Piezoelectric harvesters were used as both the sensor and the power transducers. Mounted in cantilever configuration and subjected to ground vibration or mounted in a patch configuration and subjected to strain loading, a piezoelectric transducer is capable of generating a monitoring signal that is proportional to local vibrations/or strains within the hosting structural element.

The improvement of the energy harvesting using piezoelectric from vibration has been targeted to increase the level of harvestable power. Analysis of the variations of the frequency response, amplitude, damping ratio, and efficiency of the device with respect to the preload has showed that stiffness tuning of the PZT harvester increases the average harvested power by a one order of magnitude. It was also shown that the tuning through axial preloading can be used to correct for mismatch induced effects. Combined with Shape Memory Alloy, piezoelectric harvesters provided enough power for vibration monitoring under varying external temperature. The frequency response shifts observed in the piezoelectric vibrator under varying temperature, have been adjusted meaning an applied axial loading generated by deformations in a set of SMA wires that are induced by the same temperature variations.

The second main challenge was due to the fact that the data generated by these novel self-powered modules, is different from any data used in conventional methods. The information is compressed and integrated in time, then reported as a cumulative histogram of a combined number of events repetitions times the duration versus the input strain amplitude. Adequate data interpretation techniques were developed with the purpose of extracting the variations over time of the damage index. The issues of missing data and full field generation were also addressed.

BIBLIOGRAPHY

BIBLIOGRAPHY

- Basquin O. H., "The exponential law of endurance tests", Proc. Am. Soc. Test. Mater., Vol. 10, pp 625-630, 1910.
- Bazant Z. P., Planas J., "Fracture and Size Effect in Concrete and Other Quasibrittle Materials", Boca Raton and London: CRC Press, 1998
- Birman V., Suhir E., "Effect of temperature of vibrations of physically non linear piezoelectric rods", [International Workshop on Thermal Investigation of ICs and Systems](#), Sep 2005 Belgirate Lake Maggiore Italy, 2006
- Brinson L., 1993, "One-dimensional constitutive behavior of shape memory alloys: thermomechanical derivation with non-constant material functions and redefined martensite internal variable," Journal of Intelligent Material Systems and Structures, 4, 229–242.
- Chabot A., Chupin O., Deloffre L. and Duhamel D., "Viscoroute 2.0: a tool for the simulation of moving load effects on asphalt pavement", RMPD Special Issue on Recent Advances in Numerical Simulation of Pavements, Vol. 11(2), pp 227-50, 2010
- Challa V. R., Prasad M. G., Shi Y. and Fisher F. T., "A vibration energy harvesting device with bidirectional resonance frequency tenability", Smart Mater. Struct, Vol. 17, pp 015035, 2008
- Challa V. R., Prasad M. G. and Fisher F. T., "A coupled piezoelectric–electromagnetic energy harvesting technique for achieving increased power output through damping matching", Smart Mater. Struct., Vol. 18, pp 095029, 2009
- Challa V. R., Prasad M. G., and Fisher F. T., "Towards an autonomous self-tuning vibration energy harvesting device for wireless sensor network applications", Smart Materials and Structures, Vol. 20, pp 025004, 2011
- Chatti K., Manik A., Brake N., Salama H. and Haider S. W., "Effect of Michigan Multi-axle Trucks on Pavement Distress", Report number RC-1504, Michigan Department of Transportation, 2009
- Cho S., Yun C., Lynch J. P., Zimmerman A. T., Spencer B. F. Jr., Nagayama T., 'Smart wireless sensor technology for structural health monitoring of civil structures', International Journal of Steel Structures, Vol. 8, No. 4, pp 267–75, 2008
- Coffin L. F., Manson S. S., 'Explain fatigue crack-growth in terms of plastic strain in the tip of cracks', 1954

- Doebling S. W., Farrar C. R., Prime M. B., Shevitz D. W., "Damage identification and health monitoring of structural and mechanical systems from changes in their vibration characteristics: a literature review", Los Alamos National Laboratory Report, LA-13070-MS, 1996.
- Eichhorn C., Goldschmidtboeing F. and Woias P., "Bidirectional frequency tuning of a piezoelectric energy converter based on a cantilever beam", *J. Micromech. Microeng.*, Vol. 19, pp 094006-6, 2009
- Eichhorn C., Tchagsim R., Wilhelm N. and Woias P., "A smart and self-sufficient frequency tunable vibration energy harvester", *J. Micromech. Microeng.*, Vol. 21, pp 104003, 2011
- El-Borgi S, Choura S, Ventura C, Baccouch M and Cherif F 2005 Modal identification and model updating of a reinforced concrete bridge *Int. J. Smart Struct. Syst.* **1** 83–101
- Elvin N. G., Lajnef N., and Elvin A. A., "Feasibility of Structural Monitoring With Vibration Powered Sensors", *Smart Mater. Struct.*, Vol. 15, pp 977-986, 2006
- Elvin N., Lajnef N., Chakrabartty S. and Elvin, "A sub-microwatt self-powered fatigue sensor", 14th International Symposium on Smart Structures and Materials & Nondestructive Evaluation and Health Monitoring San Diego, 2007
- Elfrink R., Kamel T. M., Goedbloed M., Matova S, Hohlfeld D, Van Schaijk R, "Vibration energy harvesting with aluminum nitride-based piezoelectric devices", Proceedings of the powermems workshop Sendai November 10–11, 2009
- Erturk A., Farmer J. R. and Inman D. J., "Effect of strain nodes and electrode configuration on piezoelectric energy harvesting from cantilevered beams", *J. Vibr. Acoust.* Vol. 131, pp 011010-1, 2009
- Erturk A., Mann B. P., Inman D. J., "Resonant Manifestation of Intrinsic Nonlinearity within Electroelastic Micropower Generators", *Appl. Phys. Lett.*, Vol. 97, pp 254101-254103, 2010
- Erturk A., Renno J. M., and Inman D. J., "Modeling of piezoelectric energy harvesting from an L-shaped beam-mass structure with an application to UAVs", *Journal of Intelligent Material Systems and Structures*, Vol. 20, pp 529-544, 2009
- Fan W., Qiao P., "Vibration-based damage identification methods: a review and comparative study", *Structural Health Monitoring*, Vol. 10, pp 83-111, 2011
- Farrar C. R., Doebling S. W., Cornwell P. J., Straser E. G., "Variability of modal parameters measured on the Alamosa Canyon Bridge", *Proc. of the 15th Int. Modal Analysis Conference*, pp. 257-263, 1997
- Finkel P., Lofland S. E., Garrity E., "Magnetoelastic/piezoelectric laminated structures for tunable remote contactless magnetic sensing and energy harvesting", *Appl. Phys. Lett.*, Vol. 94, pp 072502, 2009

- Funakubo H., "Shape Memory Alloys", Gordon and Breach Science Publishers, 1987
- Goldschmidtboeing F. and Woias P., "Characterization of different beam shapes for piezoelectric energy harvesting J. Micromech. Microeng, Vol. 18, pp 104013, 2008
- Hooker M.W., "Properties of PZT-Based Piezoelectric Ceramics Between -150 and 250°C ", Lockheed Martin Engineering & Sciences Company, NASA Center for Aerospace Information, NASA/CR-1998-208708, 1998
- Huang C., Lajnef N., Chakrabartty S., "Self-calibration and characterization of self-powered floating-gate usage monitors with single electron per second operational limit", IEEE Transactions of Circuits and Systems I, Vol. 57, No. 3, pp 556-567, 2010
- Hu Y., Xue H., and Hu H., "A piezoelectric power harvester with adjustable frequency through axial preloads", Smart. Mater. Struct., Vol. 16, pp 1961–1966, 2007
- Huet C., "Etude par une methode d'impedance du comportement viscoelastique des materiaux hydrocarbons", Ph.D. dissertation, Universite de Paris, 1963
- Huet C., "Coupled size and boundary-condition effects in viscoelastic heterogeneous and composite bodies", Mechanics of Materials, Vol. 31(12), pp 787-829, 1999
- Issa M. A., Islam M. S., Chudnovsky A., "Size Effects in Concrete Fracture: Part I, Experimental Setup and Observations", Int. J. Fracture, Vol. 102, pp 1-24, 2000
- Kim H., Priya S., Stephanou H. and Uchino K., "Consideration of impedance matching techniques for efficient piezoelectric energy harvesting", IEEE Trans. Ultrason. Ferroelectr. Freq. Control, Vol. 54, pp 1851–9, 2007
- Lajnef N., Chakrabartty S., Elvin N., "A piezopowered floating-gate sensor array for long-term fatigue monitoring in biomechanical implants", IEEE Transactions on Biomedical Circuits and Systems, Vol. 2, No. 3, pp 164-72, 2008
- Lajnef N., Rhimi M., Chatti K., Mhamdi L., Faridazar F., "Toward an integrated smart sensing system and data interpretation techniques for pavement fatigue monitoring", Computer-Aided Civil and Infrastructure Engineering, Vol. 26, pp 513-523, 2011
- Leland E. S. and Wright P. K., "Resonance tuning of piezoelectric vibration energy scavenging generators using compressive axial preload", Smart Mater. Struct., Vol. 15, pp 1413–20, 2006
- Leland E., and Wright P.K., "Resonance Tuning of Piezoelectric Vibration energy Scavenging Generators using Compressive Axial Preload," J. Smart Materials and Structures, Vol. 15, pp 1-8, 2006

- Lemaitre J., "A Course on Damage Mechanics", Springer Verlag., 1992
- Lynch J. P., Loh K. J., "A summary review of wireless sensors and sensor networks for structural health monitoring", *Shock and Vibration Digest*, Vol. 38, No. 2, pp 91-128, 2006
- Mane P., Mossi K., Green C., and Bryant, R., "Studying the effects of temperature on energy harvesting using pre-stressed piezoelectric diaphragms", *Proceeding of the SPIE International Society for Optics Engineering*, 6526-18, 2007
- Manson S., "Interfaces between fatigue, creep and fracture", *International Journal of Fracture*, Vol. 2, pp 327-363, 1966
- Manson S. S., and Halford G. R., "Practical Implementation of the double linear damage rule and damage curve approach for treating cumulative fatigue damage", *International Journal of Fracture*, Vol. 17(2), pp 169-192, 1981
- Morris D. J., Youngsman J. M., Anderson M. J. and Bahr D. F., "A resonant frequency tunable, extensional mode piezoelectric vibration harvesting mechanism", *Smart Mat. Struct.*, Vol. 17, pp 065021, 2008
- Mateu L. and Moll F., "Optimum Piezoelectric Bending Beam Structures for Energy Harvesting using Shoe Inserts", *Journal of Intelligent Material Systems and Structures*, Vol. 16, pp 835-845, 2005
- Nilsson R. N., Hopman P. C. and Isacsson U., "Influence of different theological models on predicted pavement responses in flexible pavements", *Road Materials and Pavement Design*, Vol. 3(2), pp 117-47, 2002
- Oh H., "Cumulative damage theory of concrete under variable-amplitude fatigue loadings", *ACI Mat. J.*, Vol. 88, pp 41-48, 1991
- Omote K., Ohigashi H., "Temperature Dependence of Shear Piezoelectric Properties of Poly (vinylidene fluoride) Studied by Piezoelectric Resonance Method", *J. Appi. Phys.*, Vol. 35, pp 1818-1823, 1996
- Pacific Earthquake Engineering Research Center, "[The Earthquake Engineering Online Archive](http://nisee.berkeley.edu/data/strong_motion/sacsteel/)". <http://nisee.berkeley.edu/data/strong_motion/sacsteel/> (June 2011).
- Park Y. J., "Fatigue of concrete under random loadings", *J. Struct. Eng.*, Vol. 116, pp. 3228-3235, 1990
- Peters C, Maurath D, Schock W and Manoli Y 2008 Novel electrically tunable mechanical resonator for energy harvesting *Proc. Power MEMS 2008 (Sendai, Japan, Nov.)* 253-6.

- Rahimi M., Shah H., Sukhatme G. S., Heideman J., Estrin D., "Studying the Feasibility of Energy Harvesting in a Mobile Sensor Network", Proceedings of the 2003 IEEE International Conference on Robotics & Automation, Taipei, Taiwan, September 14- 19, pp. 19-24, 2003
- Roundy S., Wright P. K., Rabaey J., "A Study of Low Level Vibrations as a Power Source for Wireless Sensor Nodes", Computer Communications, Vol. 26, pp. 1131-1144, 2002
- Rupp C. J., Evgrafov A., Maute K., and Dunn M. L., "Design of Piezoelectric Energy Harvesting Systems: A Topology Optimization Approach Based on Multilayer Plates and Shells", Journal of Intelligent Materials and Structures, Vol. 20, pp 1923–1939, 2009
- Sabat R.G., Mukherjee B., Ren W., and Yang G., "Temperature dependence of the complete material coefficients matrix of soft and hard doped piezoelectric lead zirconate titanate ceramics", J. Appl. Phys., Vol. 101, pp 064111, 2007
- Sayegh G., "Contribution a l'étude des propriétés viscoélastiques des bitumes purs et des betons bitumineux", Ph.D. dissertation, Faculte des Sciences de Paris, 1965
- Schapery R., "A Theory of Mechanical Behavior of Elastic Media with Growing Damage", Journal of the Mechanics and Physics of Solids and Other Changes in Structure, Vol. 38, pp 215-253, 1990
- Shu Y. C., Lien I. C. and Wu W. J., "An improved analysis of the SSHI interface in piezoelectric energy harvesting", J. Smart Materials and Structures, Vol. 16, pp 2253–2264, 2007
- Singh S. P., and Kaushik S. K., "Flexural Fatigue Analysis of Steel Fiber-Reinforced Concrete", ACI Materials Journal, Vol. 98(4), pp 306-312, 2001
- Stanton S. C., Erturk A., Mann B. P., Inman D. J., "Nonlinear Piezoelectricity in Electroelastic Energy Harvesters: Modeling and Experimental Identification", J. appl. Phys., Vol. 108, pp 074903-074909, 2010
- Subramaniam K. V., Oneil E. F., Popovics J. S., and Shah S. P., "Crack Propagation in Flexural Fatigue of Concrete", Journal of Engineering Mechanics, Vol. 126(9), pp 891-898, 2000
- Swallow L. M., Luo J. K., Siores E., Patel I. and Dodds D., "A Piezoelectric Fibre Composite Based Energy Harvesting Device for Potential Wearable Applications", Smart Mater. Struct., Vol. 17, pp 1–7, 2008
- Watters D. G., Jayaweera P., Bahr A. J., Huestis D. L., Priyantha N., Meline R., Reis R., Parks D., "Smart Pebble: Wireless Sensors for Structural Health Monitoring of Bridge Decks", Proceedings of SPIE 5057 20-8, 2003
- Xiao Y. C., Li S., and Gao Z., "A continuum damage mechanics model for high cycle fatigue", International Journal of Fatigue, Vol. 20(7), pp 503-508, 1998